The Dissertation Committee for Youssef Wahib Naguib Ibrahim Certifies that this is the approved version of the following dissertation:

Application of pharmaceutical technologies to improve the activity of cancer chemotherapeutic agents

Committee:

Zhengrong Cui, Supervisor

Stephen D. Hursting

Hugh D. Smyth

Salomon Stavchansky

Robert O. Williams, III

Application of pharmaceutical technologies to improve the activity of cancer chemotherapeutic agents

by

Youssef Wahib Naguib Ibrahim, B. Pharm. Sci.; M.S.

Dissertation

Presented to the Faculty of the Graduate School of

The University of Texas at Austin

in Partial Fulfillment

of the Requirements

for the Degree of

Doctor of Philosophy

The University of Texas at Austin

May 2015

Dedication

To Diana, Anthony, Wahib, Ibtesam, Michel, and Sherri

My beloved family,

without your tremendous love nothing could have been.

Acknowledgements

I would like to express my deepest appreciation and cordial gratitude to my advisor Dr. Zhengrong Cui for his priceless effort, time, and support. His top academic standards, thoughtful knowledge, and sincere scientific determination will always give me guidance along the way. I would also like to thank my committee members Dr. Williams, Dr. Stavchansky, Dr. Smyth, and Dr. Hursting for their invaluable discussions, support, and advice.

I would also like to express my sincere gratitude to my lab mates, Mr. Abdulaziz Aldayel, Dr. Amit Kumar, Dr. Leticia Rodriguez, Dr. Yuriko Kiguchi, Dr. Dharmika Lansakara, Dr. Mengmeng Niu, Dr. Xinran Li, Mr. Michael Sandoval and Dr. Tinashe Ruwona. I will never forget the unconditional help, friendship, motivation, and useful discussion they kept on providing.

I also want to acknowledge all the current and former lab members of Dr. Cui's group, especially Dr. Saijie Zhu, Dr. Yixuan Dong, Ms. Solange Valdes, Ms. Julie Choi, Mr. Sachin Thakkar, Ms. Hannah O'Mary, Dr. Rebecca De Angel, Dr. Gang Xiao, Dr. Yuehong Xu, Dr. Piyanuch Wonganan, and Dr. Mangalika Warthaka for being such nice and friendly colleagues. They tremendously helped make the lab such a nice place to be.

I also would like to thank Dr. Laura Lashinger for her substantial assistance and contribution in some parts of research experiments that I have done towards my degree. I am as well grateful to Ms. Audrey Rasmussen and Ms. Hannah Ruisi for their help with some animal experiments.

I also thank Dr. Yue Li and Ms. Rebecca Fitch for their outstanding help in flow cytometry and histology. I am grateful as well to Dr. Steve Swinnea and Dr. Vincent

Lynch for their help with X-ray diffraction. The sincere help and professional administrative assistance provided by Mrs. Stephanie Crouch and Mrs. Yolanda Camacho in the college of Pharmacy is deeply appreciated.

I also want to acknowledge the financial support towards a full doctoral scholarship that was kindly provided by the Ministry of Higher Education of Egypt.

In addition, I also acknowledge the college of Pharmacy at the University of Texas at Austin for selecting me as the recipient of the Crowley and Vaughn graduate fellowship, The Duane A. Boyle fellowship in Pharmaceutics, and the Max & Mary Anne Burlage Fellowship in pharmacy.

I can never forget the unlimited support I kept on getting from my parents Ebtesam and Wahib, and from my wife Diana, all through my study years. Their love and care exceeded every boundary, and never waned along the years. Also, the smile of my beloved son Anthony was able to raise me up whenever things were not going the way they should. My brother and sister were always there whenever I needed them. To my beautiful family, I just want to say ‘I love you’.

Application of pharmaceutical technologies to improve the activity of cancer chemotherapeutic agents

Youssef Wahib Naguib Ibrahim, PhD

The University of Texas at Austin, 2015

Supervisor: Zhengrong Cui

Cancer is a leading cause of death worldwide. Chemotherapy remains a major therapeutic modality in cancer treatment. Conventional chemotherapeutic agents usually have limited efficacy. Furthermore, chemotherapeutic agent- and/or excipient-related toxicities comprise a serious problem that may, in many cases, deteriorate the patient's quality of life. In this dissertation, different pharmaceutical technology approaches, including nanotechnology and pharmaceutical chemistry, were utilized to improve the activity of chemotherapeutic agents.

Docetaxel is a second generation taxane used as a single agent in breast cancer, non-small cell lung cancer, and other cancers. Side effects related to the drug itself and one of the excipients (i.e. Tween 80) are extensive. I designed a solid lipid nanoparticle (DCX-SLNs) formulation to improve the delivery of docetaxel into solid tumors and to avoid excipient-related side effects associated with the current Tween 80-based docetaxel

formulation. The DCX-SLNs showed improved *in vitro* cytotoxicity in various cell lines and significantly inhibited tumor growth in an aggressive mouse model of lung cancer, while the Tween 80-based docetaxel formulation was not effective at the dose and dosing frequency tested. Higher drug accumulation in tumor tissues was achieved when the DCX-SLNs were injected intravenously, as compared to the Tween 80-based docetaxel formulation.

Gemcitabine (2´, 2´-difluorodeoxycytidine, dFdC) is the first line treatment for advanced pancreatic cancer. It is also used in other cancers (e.g. ovarian and breast cancers). In this dissertation, docosahexaenoic acid (DHA), an omega-3 polyunsaturated fatty acid, was conjugated to gemcitabine in the 4(N)-amine group to synthesize a new compound (DHA-dFdC). DHA-dFdC shows potent and broad spectrum cytotoxicity against all NCI/DTP60 human cancer cell lines. DHA-dFdC is also 100000-fold more cytotoxic than gemcitabine against human and mouse pancreatic cancer cells. In addition, DHA-dFdC shows high accumulation in mouse pancreas following intravenous injection, prompting the evaluation of its antitumor activity in mouse models of pancreatic cancer. In nude mice with subcutaneous or orthotopic human Panc-1 tumors, DHA-dFdC is more effective than the molar equivalent dose of gemcitabine in inhibiting the tumor growth.

In conclusion, the activity of cancer chemotherapeutic agents can be significantly improved by formulating them with innovative pharmaceutical technologies.

Table of Contents

Appendix A

Appendix B

List of Tables

List of Figures

List of Schemes

Chapter 1

Nanomedicine: The Promise and Challenges in Cancer Chemotherapy [1]

1.1 Introduction

1.1.1 Nanomedicine and cancer

Cancer is a leading cause of death worldwide. Conventional chemotherapy has drawbacks ranging from limited effectiveness, chemoresistance, and treatment-related side-effects and damages to healthy tissues. The idea of drug targeting started to emerge as early as 1906. As outlined by Danhier *et al.*, the challenge ahead is about how to find proper targets, to develop a drug that exploits the targets, and finally to design the proper delivery system (carrier) for the drug [1]. Cancer nanomedicine is the application of nano-sized entities (10-200 nm) to diagnose, prevent, or treat cancer. These entities can be loaded with chemotherapeutics, nucleic acids, radiosensitizers, diagnostic agents and/or probes. This chapter displays an updated review of several nano-carrier platforms, their common features, and applications, followed by a discussion of the major mechanisms by which nano-carriers are targeted to the cancer cells. Finally it discusses the barriers that hinder the application of nanomedicine in cancer chemotherapy, and how the rational design of the nanomedicine may overcome these barriers.

---

[1] This chapter is based on "*Youssef W. Naguib and Zhengrong Cui,* ***Advances in Experimental Medicine and Biology****, 2014, 811: 207-233"*

1.2. General classification of nano-carrier platforms.

1.2.1 Liposomes

Liposomes are one of the earliest nano-scale drug carriers reported in literature, first described by Bangham *et al.* [2;3]. They are spherical vesicles, composed of closed phospholipid bilayer structures that resemble the cell membrane. Their unique structure enables the encapsulation of water soluble drugs within their hydrophilic cores, while water-insoluble drugs can be entrapped within the lipid bilayer [4]. Nucleic acids (e.g., plasmids) can be non-covalently attached on the surface of cationic liposomes via electrostatic interaction [5]. Various biocompatible phospholipids, including 1,2-distearoyl-sn-glycero-3-phosphoethanolamine (DSPE) and 1,2-distearoyl-glycero-3-phosphocholine (DSPG), are in products that have been approved by the United States Food and Drug Administration (FDA) for human use [6]. Different types of liposome have different sizes. For example, multi-lamellar liposomes have a size range of about 500-5000 nm, while uni-lamellar liposomes can be as small as 50-100 nm [7]. Liposome surface can be modified with polyethylene glycol (i.e., PEGylation) to prolong their blood circulation time [8-10]. In addition, liposome surface can be modified with various targeting moieties, including small molecules (e.g., anisamide as a ligand to Sigma receptors [11-13]) or macromolecules (e.g., monoclonal antibodies in immunoliposomes [14;15]) to bind to targets that are exclusively expressed, or overexpressed, by tumor cells. Liposomal formulations of anticancer drugs currently in the market include PEGylated doxorubicin liposomes (Doxil®, about 100 nm), non-PEGylated doxorubicin

liposomes (Myocet®), and non-PEGylated daunorubicin liposomes (Daunoxome®, about 35-65 nm). The advantages and disadvantages of PEGylation will be discussed in more details later.

1.2.2 Polymeric nanoparticles.

Various polymers have been used to prepare nanoparticles, including natural polymers (e.g., chitosan and albumin) and synthetic polymers (e.g., poly-lactic acid (PLA) and poly-lactic-co-glycolic acid (PLGA)). PLA and PLGA are widely used in nano- and micro-particle preparation due to their biodegradability, biocompatibility, and well-documented safety profile [16;17]. Nanoparticles prepared by polyesters, such as PLA, PLGA, and poly-ε-caprolactone (PCL), undergo bulk erosion, where the aqueous medium penetrates inside the nano-carriers and causes hydrolysis of the core, which brings on further erosion of the bulk [18;19]. On the contrary, nanoparticles prepared with other polymeric classes, such as poly-anhydrides and poly-orthoesters, undergo surface erosion, which provides a zero-order release pattern [19-21]. Various homopolymers (e.g., PLA), co-polymers (e.g., PLGA), and block-co-polymers (e.g., PLGA-polyethylene glycol (PLGA-PEG), and PCL-PEG) have been used to prepare nano-carriers. Block-copolymers that contain PEG chains may render the nanoparticles prepared using them ‘stealthy’ and ‘long circulating’ [22].

Emulsion-based methods can be used to prepare PLA or PLGA nanoparticles, where a single oil-in-water (O/W) emulsion method is suitable for lipophilic drugs (e.g., docetaxel [23]), whereas the double emulsion (W/O/W) method helps the encapsulation

of hydrophilic drugs (e.g. siRNA [24]). The double emulsion method involves the use of two immiscible liquid phases, where a surface active agent is necessary to form the stable emulsion, and nanoparticles are solidified following solvent evaporation [25]. On the other hand, the nanoprecipitation (solvent displacement) method involves the use of two miscible liquids for the spontaneous formation of nanoparticles, without the use of surfactant, as the method does not rely on interfacial phenomenon [25;26]. Other methods that can be used to prepare polymeric nanoparticles include spray drying [27] and supercritical fluid technology [28]. In addition, micro- and nano-fabrication methods (e.g., particle replication in non-wetting templates, PRINT) are developed to produce nano-structures with a high level of control over shapes, sizes, aspect ratios, and surface chemistry, where nano-discs, filaments, rods, cubes, cylinders, and spheres can be produced and rationally employed to tackle drug delivery hurdles. For more information on these techniques, the reader is referred to [29-31].

1.2.3 Micelles

Micelles are self-assembled nano-aggregates, composed of amphiphilic block-copolymer or lipid-based molecules, with a lipophilic core and hydrophilic shell to solubilize lipophilic drugs. Various micelles that are based on poloxamers [32], PEGylated polyesters (e.g., PLA-PEG) [33], or PCL-PEG [34] have been used to deliver anticancer agents. For example, Genexol-PM, which is based on PLA-PEG micelles with an average size of about 60 nm for paclitaxel delivery, has gained approval for human use in South Korea in 2006 [6]. A mixed micelle is a self-assembled nano-structure

composed of a mixture of two or more block-copolymers, mixed together to impart the favorable features of each single component to the final micellar structure [35]. Poloxamers (Pluronic ®, tri-block copolymers of the hydrophilic polyethylene oxide (PEO) and the lipophilic polypropylene oxide (PPO), in the form of PEO-PPO-PEO) with different grades and PEO to PPO ratios are commonly used for this purpose. Chen *et al.* developed a mixed micelles formulation, composed of Pluronics P105 and F127, for the delivery of docetaxel to taxol-resistant lung cancer cells [36]. Due to the high content of PPO in P105, high docetaxel content could be loaded. However, the short PEO chains were not sufficient to stabilize the micelles. The long PEO chains of Pluronic F127, when mixed with P105, successfully improved the stability of the final formulation [36].

1.2.4 Solid lipid nanoparticles (SLNs)

SLNs are lipid-based nano-carriers that are solid at room temperature and can successfully encapsulate lipid-soluble drugs. Materials used to prepare SLNs include mono-, di-, tri-glycerides, or a mixture of them, fatty acids (e.g., stearic acid), and phospholipids (e.g., phosphatidyl choline and lecithin). While the method of high pressure homogenization (HPH) is widely used to prepare SLNs [37;38], other methods have also been described in literature, including emulsion-based methods [39], ultrasonication [40], and solvent injection method [41]. Advantages of SLNs include cost-effective production, even in large-scale [42]. For more detailed information on the application of SLNs in cancer therapy, the reader is referred to [43;44].

1.2.5 Drug-polymer conjugates

These are composed of a small molecule anticancer agent(s) covalently linked to a biocompatible polymeric chain via a bio-responsive linker. Drug-polymer conjugates may improve the pharmacokinetics profile of the drug, enhance its stability, and increase the accumulation of the drugs in tumor tissues or inside tumor cells [6;45-48]. Various drug-polymer conjugates have been investigated since the idea was hypothesized by Ringsdorf [49]. One of the very early conjugates is the doxorubicin-(N-(2-hydroxypropyl) methacrylamide) copolymer conjugate (doxorubicin-HPMA, PK1, FCE28068), which is designed to unload the doxorubicin in tumor cells following the cleavage of the peptidyl linker by lysosomal cysteine proteinases [50]. Other drug conjugates that have been developed include HPMA-doxorubicin-gemcitabine conjugate [51], paclitaxel-polylactide conjugate [52], polyethylene glycol-camptothecin (PEG-camptothecin, Pegamotecan) [46], and paclitaxel-polyglutamic acid conjugate (paclitaxel polyglumex, PPX, Opaxio) [45]. Pegamotecan is a PEG-camptothecin conjugate that is linked via an ester bond, with a drug loading of 1.7% (w/w). Unfortunately, Pegamotecan did not show a promising clinical benefit compared to irrinotecan in patients with gastric or gastroesophageal adenocarcinoma in a phase II trial and was subsequently discontinued by its sponsor [46]. Opaxio (PPX, formerly known as Xyotax) is a water soluble conjugate, composed of paclitaxel (37%, w/v) conjugated in a comb-like manner to poly L-glutamic acid via a degradable linker [46;53;54]. Despite very promising data in preclinical and early phase clinical studies, data from several phase III clinical studies showed that PPX is not significantly more effective than standard treatments [54]. For

example, the conjugate did not show any survival benefit, compared to either gemcitabine or vinorelbine single agent chemotherapeutic, in a randomized phase III trial in patients with advanced non-small cell lung cancer (NSCLC) [55]. Similarly, no survival benefit was found when PPX was used as a second line of treatment against NSCLC in a phase III trial on 849 patients, compared to docetaxel [56]. Nonetheless, this conjugate is still under extensive clinical investigation.

1.2.6 Antibody-drug conjugates

Monoclonal antibody (mAb)-drug conjugates (ADC or immunoconjugates) are bifunctional molecules that benefit from the targeting capabilities of the mAb moiety and the cytotoxic activity of the drug. Candidate mAbs should be chosen to target antigens that are exclusively expressed or overexpressed on tumor cells, but not on neighboring healthy tissues [57;58]. Advantages of ADCs include the potential to achieve a much higher concentration of the cytotoxic agent in tumor tissues (mainly due to the targeting abilities of the mAb), a lower systemic toxicity [59;60], and an overall improved pharmacokinetic profile [61]. ADCs can benefit from the long circulatory half-life of mAbs [62]. However, the stability of the linker between the mAbs and the drug molecules should also match this long-circulation time. Modifications of the linker between the mAb and the cytotoxic agent have successfully overcome some of the major problems encountered earlier with ADCs. For example, when both the drug and the linker were hydrophobic, the maximum drug-antibody ratio (DAR) obtained was 3 to 4, and further increase of the ratio resulted in aggregations and short circulation time [63]. The

use of hydrophilic linkers helps improve the drug-antibody ratio (DAR) [62-64]. Clinical problems associated with ADCs include systemic toxicity, which may be attributed to immature drug release and antigen shedding from the tumor tissues into the circulation; the shed antigens can reside anywhere in the body and mislead the 'homing missile' to a false target [57;65;66]. Other disadvantages include unexpectedly low tumor accumulation of the cytotoxic agent, with values as low as 0.0003%-0.08% of the injected dose per gram of tumor [65]. This led to a shift from using conventional cytotoxic agents (e.g., doxorubicin) to other agents with superior toxicity profiles that previously hindered their clinical use (e.g., maytansinoids, calicheamicins, and auristatins) [58;67]. However, systemic toxicities of these agents, even after mAb conjugation, may still prevail. For example, the FDA announced that Pfizer voluntarily withdrew Mylotarg® (gemtuzumab ozogamicin) in 2010 for safety and efficacy issues [68]. In addition, the low tumor accumulation necessitates the administration of large doses of the conjugates, which, in turn, may stir economic problems, especially for long-term therapy. For example, the estimated single dose cost of an auristatin-CD30 conjugate (Brentuximab vedotin) is about $13,500 every 3 weeks [69]. Nevertheless, ADCs are still regarded as very promising alternatives to conventional chemotherapy, with improved anticancer activity and safety profiles.

1.2.7 Inorganic nanoparticles

These include carbon nanotubes [70], fullerenes [71], gold nanoparticles [72], silica nanoparticles [73], iron oxide nanoparticles [74], zirconium nano-platelets [75], and

quantum dots [76]. These nano-structures will not be overviewed in this chapter, and comprehensive reviews on their application in cancer treatment and imaging can be found elsewhere [77-81].

1.3 Mechanisms underlying nano-carrier-based drug delivery to tumors

1.3.1 Passive targeting via enhanced permeation and retention (EPR) phenomenon.

1.3.1.1 Background. The EPR phenomenon was discovered by Matsumura and Maeda in 1986 [82;83]. Maeda and coworker(s), working on an anticancer protein-polymer conjugate called SMANCS (neocarzinostatin-styrene-maleic acid conjugate), noticed that many solid tumors exhibit enhanced vascular permeability that resembles the inflammatory state of normal non-cancerous tissues. In this context, the elimination of a macromolecule (i.e., Evans blue-albumin complex) from normal tissues was found to be much faster than that from tumor tissues [82;84;85].

When a tumor starts to form, the tumor cells rapidly proliferate, but the nutritional supply (mainly via diffusion) is only suitable for normally proliferating cells [86]. Thus, the tumor size is limited to what is called ‘diffusion-limited size’ (about 2 mm) [86;87]. In order to satisfy their craving for nutrients, cancer cells recruit new blood vessels, and tumor angiogenesis starts to take place [86]. This phase is characterized by excessive secretion of angiogenic factors such as vascular endothelial growth factor (VEGF), platelet-derived growth factor (PDGF), basic fibroblast growth factor (bFGF), in addition

to other factors (e.g., bradykinins, nitric oxide (NO), cytokines, matrix metalloproteinases (MMP)), which enhance angiogenesis and vascular permeability [87-89]. The mechanism of neo-angiogenesis in tumors is discussed in details elsewhere [86;90].

The newly-formed blood vessels have a leaky imperfect structure and abnormal basement membrane, while pericytes and smooth muscle layer are deficient or almost absent [87;91]. This leaves the tumor blood vessel architecture flawed with fenestrations. The size of the fenestrations is heterogeneous and can reach a maximum cut-off value of 200-800 nm [83], or 1000-2000 nm in some other reports [84;91]. Blood flow within tumors is also erratic and tortuous [87]. The imperfect, and fenestrated architecture of tumor vasculature helps the extravasation of circulating macromolecules and nano-carriers into the tumor tissues (i.e., enhanced permeation), which does not happen in healthy organs with intact vasculature [83;84;87]. The other facet of EPR is the enhanced retention and accumulation of extravasated macromolecules and nano-carriers within tumor tissues, which is facilitated by the poor lymphatic drainage and slow venous return in tumor tissues [84;89;91]. Small molecules may also benefit from the enhanced permeability of the tumor vasculature, but they will fail to accumulate within the tumor tissues, as they will be ‘washed out’ quickly by diffusion [83;87;89]. The leaky tumor vasculature also gives detached cancer cells access to the circulation, causing metastasis [87;91]. The phenomenon has been exploited in many human tumors (excluding hypovascular tumors such as pancreatic cancer) for both chemotherapeutic and imaging applications [89;92;93].

1.3.1.2 Challenges associated with EPR-mediated delivery systems.

Tumor heterogeneity. Heterogeneity is one of the landmarks of tumors in the clinical application. Many factors need to be studied before an EPR-based nanomedicine can move to the clinic. These factors include the differences in cancers in vasculature development and architecture, the effect of the cancer stage on the EPR features, the chances of delivering nanomedicine to the metastatic lesion vs. primary tumor sites, the effect of tumor stromal density (will be discussed later), in addition to patient-to-patient variability, and whether individualized nanomedicine is necessary. Tumor heterogeneity may also extend to pre-clinical level, as the animal tumor model selection may have a significant effect on decision-making regarding subsequent clinical trials. It is reported that subcutaneous xenografts are hastily-formed tumors that usually exhibit an exaggerated phenotype of EPR, which may not be of great value in clinical translation [94]. Orthotopic tumor models and, more importantly, genetically engineered mouse models (GEMM) may be of greater value when studying EPR effect on nanomedicine delivery. For more information on the effect of tumor heterogeneity on the EPR effect, the reader can refer to [94-97]. In addition, in order to achieve more correlation between animal tumor models and cancer patients, factors such as the difference in treatment regimens in mice and in humans due to different metabolic rates and the huge tumor/body weight ratio in mice compared to humans should be carefully considered in translational research [98].

Augmenting the EPR effect. Maeda and co-workers hypothesized that, since tumor vasculature lacks an intact basement membrane and smooth muscle layer, when a vasoconstrictor agent (e.g. angiotensin II) is systemically administered, the tumor blood vessels will not be affected, while other blood vessels in the body will be constricted with subsequent increased blood pressure. Thus, the tumor blood flow is expected to increase, which in turn will increase the delivery of nanomedicine to tumors via EPR effect [99]. It was noticed that the combined administration of enalapril, an angiotensin-converting enzyme inhibitor with vascular permeability enhancement effect, and angiotensin II, led to a 2-fold increase in the accumulation of a labeled mAb in human colon tumor-bearing athymic mice [91;99]. In another report, when a nitroglycerin (NO-generating substance) ointment was applied onto tumor-bearing animal skin in an area distant from the tumor site, blood flow in tumors was significantly enhanced, but not in muscles [100]. The tumor accumulation, as well as the antitumor effect, of a ^{65}Zn-labeled macromolecular drug (PEG-Zn-protoporphyrin IX, PZP) was significantly enhanced following topical application of nitroglycerin [91;100].

Tumor vascular "normalization" and nanomedicine. While the aberrantly-formed tumor vasculature is considered to be a feature that should be taken advantage of in nanomedicine delivery, other researchers regarded it as an obstacle that should be 'normalized' in order to pave the way for the delivery of chemotherapeutic agents to tumors. Jain and co-workers were the first to introduce the idea of 'tumor vascular normalization' in response to anti-VEGF treatment [101;102]. They proposed that the

defective tumor vascular architecture may have a detrimental effect on the delivery of nanomedicines, and chemotherapy in general, to tumors [102]. According to their hypothesis, tumor vascular "normalization" is expected to alleviate tumor hypoxia, and thus enhance tumor radiation therapy outcomes, reduce metastasis and the emergence of resistance, and ultimately improve tumor chemotherapy [102-104]. In addition, the vessels themselves will have less leakiness, normal basement membrane and pericyte distribution [94;101]. In normal state, there is a balance between pro- and anti-angiogenic factors; however, in tumor state, this balance is shifted towards pro-angiogeic activity to promote tumor neo-vasculature formation [105]. The 'cautious' use of the anti-angiogenic treatment modalities (e.g., mAb for VEGF like bevacizumab, Avastin®, and VEGF receptor tyrosine kinase inhibitors) is the most common method to shift the pro- and anti-angiogenic balance back to 'normalized' levels, not to a complete anti-angiogenicity [103;105]. Although the latter strategy of abolishing tumor vasculature may be expected to starve the tumor, it may also harm normal tissue vasculature and adversely affect further chemotherapy delivery [101]. Unfortunately, the vascular "normalization" effect was found to be transient (about 7-10 days), and during this period (called the "normalization" window), concomitant chemotherapy or radiotherapy should start [105;106]. However, there is an argument that this technique minimizes the benefit of EPR phenomenon in solid tumors, as the leaky tumor vasculature will be almost lost [94]. Recently, Jain and coworkers found that tumor vascular "normalization" improved the tumor uptake of 10-12 nm nanoparticles (i.e., albumin-bound paclitaxel in Abraxane®), but not 100 nm nanoparticles (i.e., Doxil®) [107]. The study highlighted the

importance of judicially adjusting the dose of the tumor vascular “normalization” treatment, as the use of a higher dose hindered the uptake of even the small nanoparticles [107].

1.3.2 Active targeting.

The term active targeting involves the exploitation of certain proteins or any other targets, exclusively expressed, or overexpressed, by tumor cells or tumor vasculature via the attachment of a specific ligand onto the surface of the nano-carriers (surface decoration); such ligand should bind at a high affinity to the tumor target. The receptor-bound nano-carriers are then internalized inside tumor cells via receptor-mediated endocytosis [108]. While tumor accumulation takes place via EPR, the role of active targeting may be thought of as a tool towards the cellular internalization of nano-carriers. Various targets have been identified in tumors, including angiogenesis targets such as vascular endothelial growth factor receptors (VEGFR), and $\alpha_v\beta_3$ integrin, epidermal receptors such as epidermal growth factor receptor (EGFR) and human epidermal growth factor receptor 2 (HER-2), human vasoactive intestinal peptide (VIP) receptors, sigma receptors, transferrin receptors, and folic acid receptors [109;110].

Two main EGFR tyrosine kinases are well-studied and characterized, namely, EGFR and HER-2. This family of receptor tyrosine kinases mediate cell signaling towards proliferation following the binding of growth factor ligands [109]. Cetuximab (Erbitux®, Bristol Myers Squibb, NJ) and Trastuzumab (Herceptin®, Genetech, CA) are FDA-approved mAbs against EGFR and HER-2, respectively, and have been used either

as a whole mAb or a fraction of an antibody (Fab') as targeting moieties to decorate the surface of nano-carriers to improve tumor targeting [109;111;112]. Several methods have been adopted to conjugate mAbs onto nanoparticles, including avidin-biotin interaction and covalent conjugation between nano-carriers with thiolated surface and maleimide-modified mAbs [112;113]. For example, Sandoval *et al.* designed an EGFR-targeted SLNs that contain a lipophilic gemcitabine prodrug (4(*N*)-stearoyl gemcitabine, GemC18) to target human breast cancer cells that overexpress EGFR [114]. Recombinant mouse epidermal growth factor (EGF) was first thiolated and purified, and then conjugated to maleimide-terminated PEG chains on the surface of GemC18-SLNs. Compared to non-targeted GemC18-SLNs, the EGFR-targeted SLNs showed enhanced antitumor activity and accumulation in tumors in mice with pre-established human breast cancer tumors (MDA-MB-468) [114]. Other tumor cell targets include transferrin receptors, sigma receptors, and folic acid receptors (FAR), which can be targeted with nano-carriers surface-decorated with transferrin [115], folic acid [116-118], and anisamide [11;13], respectively. Currently, a prostate-specific membrane antigen (PSMA)-targeted PLGA-PEG nanoparticle formulation that contains the second generation taxane docetaxel (BIND-014, BIND Biosciences Inc., MA) is under evaluation in clinical trials [119].

1.4 Barriers to delivering nanomedicines to the tumors.

In this section, the major barriers that hinder the delivery of nanomedicines to tumors will be discussed. Once a nanomedicine is administered, it has to pass some

physiological barriers to reach the circulation, unless it is administered by intravenous (i.v.) injection. Once injected, the nanomedicine has to travel a long way to reach its target: the cancer cell. The body starts to react the very first moment the nanomedicine is in the circulation, in a way that tends to clear the blood from the newly introduced foreign material. Even the fraction of the nanomedicines that makes its way past these clearance mechanisms and reach the tumors will encounter a totally different environment that should also be tackled in order to get to the tumor cells. Two major approaches are generally applied to tackle the tumor microenvironment; one is to breach or modify the physical barriers of the tumor microenvironment, paving the way for subsequent doses, and the other is to take advantage of some of the unique features that characterize the tumor microenvironment to deliver more drugs to cancer cells. Unfortunately, getting to the cells will not be the end of the journey, as the cancer cells have their own set of defenses that only a nanomedicine with a 'smart' design will be able to evade. This section will discuss the barriers that nanomedicines encounters on their voyage to targets, and how nanomedicines can be designed to reach these targets.

1.4.1 Nanomedicine circulation time.

Once in the circulation, nano-carriers are subject to quick surface adsorption of plasma proteins, including albumin, immunoglobulins, and complement proteins (opsonins), in a process called opsonization [120]. The 'opsonin-tagged' nano-carriers are then recognized and phagocytosed by the mononuclear phagocytic system (MPS) cells (e.g., monocytes and macrophages), which carry them to the MPS organs (e.g., liver,

spleen, and lymph nodes), significantly shortening the circulation half-life of the nano-carriers [121;122]. The accumulation of non-degradable nano-carriers in MPS organs may lead to toxicity [123]. In addition, glomerular filtration of nano-carriers smaller than 5.5 nm (renal filtration cutoff size) can take place, while much larger particles (~1 μm) are quickly opsonized [120;124]. Although the 5.5 nm cutoff size seems too small, some nano-carriers may fall within this range and are filtered in the kidney (e.g. quantum dots, and carbon nanotubes [122]). Several factors determine the rate of opsonization of nano-carriers by plasma proteins, including surface characteristics (hydrophobic vs. hydrophilic), zeta potential, particle size, and shape [120;123]. In general, opsonization occurs more efficiently and much faster to particles with hydrophobic surfaces than to those with hydrophilic surfaces [123]. This was the basis for the surface modification of nano-carriers with a hydrophilic molecule, which is the most widely-used strategy to prolong the circulation time of nano-carriers. PEG is the most successfully used molecule to achieve this goal, and the process is called PEGylation. The technique was first exploited by Klibanov *et al.* in 1990, where a PEG moiety is covalently conjugated to a phospholipid (e.g., dioleoyl phosphoethanolamine, DOPE) that was incorporated into large uni-lamellar liposomes [10]. About 85% and 49% of PEGylated liposomes were found circulating in mouse plasma 1 h and 5 h after injection, respectively, compared to about 20% and 0% for their non-PEGylated counterparts [10]. It is thought that the protruding PEG chains sterically hinder the adsorption of plasma proteins to the nano-carrier surface [10], and the hydrophilic nature that they impart to the nano-carrier surface minimizes non-specific interaction with MPS cells [10;125]. The term STEALTH

has been employed to describe such PEGylated, long-circulating nano-carriers, as PEGylation has become a very solid dogma in the rational design of nano-carriers for the delivery of tumor chemotherapeutics. Various researchers studied factors that govern efficient PEGylation. Desimone and colleagues studied the effect of PEGylation density on protein binding, macrophage uptake, and circulation time of PEGylated hydrogel nanoparticles (80 × 80 × 320 nm) produced by PRINT technology, where the nanoparticles were PEG-functionalized in two different conformations, brush and mushroom [126]. The researchers found that protein binding to the surface of nanoparticles is inversely proportional to PEG density, and interestingly, efficient protein binding inhibition and prolonged circulation were achieved at a less PEG density than what was previously reported [126]. Drug release from the nano-carrier is yet another factor that should be carefully considered in nano-carrier design. Since very fast drug release can result in complete dumping of the drug in the circulation before the nano-carriers reaches their target, a prolonged circulation time should be matched with slow drug release to prevent pre-mature drug leakage [44].

PEGylation strategy is not problem-free; it was found that repeated doses of PEGylated nano-carriers (e.g., Stealth liposomes, micelles, or nanoparticles) may elicit an immune response [127]. This phenomenon, commonly known as accelerated blood clearance (ABC), may result in rapid clearance and loss of clinical benefit of subsequent doses [128]. The details of the phenomenon, in addition to methods to overcome its detrimental effects, are reviewed elsewhere [127].

Bio-mimetic particles, which are ‘camouflaged’ micro- or nanoparticles that resemble biological entities, such as viruses, bacteria, red blood cells (RBC’s), and leukocytes, have been extensively studied for drug delivery purposes. Since these previously mentioned biological entities have tremendous capabilities to evade most biological and cellular barriers in the mammalian bodies, the ‘camouflaged’ nanoparticles, if properly designed, can be expected to do the same [129]. This strategy, along with the judicious control of shape and size of the nano-carriers, has been adopted to increase the circulation time of drug-loaded nano-carriers and improve overall drug delivery to tumors [124]. To mimic filamentous viruses, Discher and co-workers developed a PEGylated flexible filamentous micelle formulation (filomicelles), of at least one dimension in the nano-range and the other may extend to microns, that was able to evade MPS cell uptake and circulate longer in the plasma, and consequently, deliver more drugs to tumors via EPR [130]. The PEG-PCL filomicelles showed persistent circulation in the plasma for up to a week, while their spherical counterparts were only there for one tenth of this time [131]. The paclitaxel-loaded filomicelles showed superior proapoptotic and tumor-shrinking activities in tumor-bearing nude mice, as compared to free paclitaxel, which was completely ineffective [131]. Recently, Taciotti and co-workers synthesized leukocyte-camouflaged non-porous silicone nanoparticles (leukolike vectors, LLV) coated with a leukocyte cellular membrane to impart cell-like functions to the nano-carrier [132]. These particles exhibited significantly less opsonization and cellular uptake by murine macrophages and human phagocytic cells. These particles may be promising in delivering drugs to tumors, not only because they undergo delayed liver

clearance and enhanced tumor accumulation in mice, but also because their tumoritropic accumulation is driven by the EPR effect and is also dependent on their ability to recognize and bind to tumor endothelium in an active form [132].

Other biological barriers. Other biological barriers in the delivery of nanomedicines to tumors include the blood brain barrier (BBB) or blood brain-tumor barrier (BBTB) following i.v. administration. Due to the presence of BBTB, characterized by the presence of endothelial cells tight junctions and low permeability into the tumor parenchyma, with vascular pore size of about 12 nm, the EPR effect may not be useful in increasing the delivery of nanomedicines in brain tumor tissues [120]. The use of targeting ligands to enable the translocation of the nano-carriers across the endothelial cells of the tumor vasculature is becoming a very promising technique [133-135]. Among the most exploited endothelial targets in tumors are $\alpha_v\beta_3$ and $\alpha_v\beta_5$ integrins, and D-glucose transporter protein (GLUT), where RGD (argentine-glycine-aspartic acid) peptide motifs [134] and deoxy-D-glucose are used to modify the surface of nano-carriers to facilitate such active-targeted uptake [133].

1.4.2 Nanomedicine and tumor microenvironment

1.4.2.1 Background. A better understanding of the tumor micro-structure is a cornerstone in the design of a successful nanomedicine. A tumor cannot be described as myriads of cancer cells, all packed together, and localized in a specific region. Tumors

can be considered as organs, with both well- and ill-formed structures, and various kinds of cells, including tumor cells, tumor fibroblasts, inflammatory cells (e.g. macrophages), blood and lymphatic network of vessels, held together within a complicated cross-linked extracellular matrix (ECM) [103;136;137]. In this section, various features of the tumor microenvironment will be overviewed in order to make a better use of the diverse toolbox that nanomedicine may provide to potentially conquer cancer.

ECM. The ECM components include various proteins (e.g., collagens), glycosaminoglycan-containing glycoproteins (e.g., hyaluronic acid (HA) and proteoglycans), the glycoprotein SPARC (secreted protein, acidic and rich in cysteine), and polysaccharides [138-140]. ECM components are usually differentiated into basement membrane and interstitial matrix [141]. Collagen type I, in addition to fibronectin, imparts mechanical integrity of the interstitial matrix of tumors [140]. A major determinant in the heterogeneity of tumor matrix rigidity is the expression level of matrix metalloproteinases (MMPs), which are overexpressed in many tumors and are responsible for collagen fibrils proteolysis within the tumor matrix [138;141;142]. Overexpression of MMPs is usually associated with decreased matrix rigidity, increased potential for cancer cells migration and metastasis, and the prevention of apoptosis [143]. ECM stiffness is also attributed in part to the overexpression of lysyl oxidase (LOX), which is responsible for hyaluronic acid and collagen fibers cross-linking [141;144]. Overexpressions of MMPs and LOX are correlated with poor cancer patient prognosis [141;142]. The interplay between ECM components verifies the overall state of tumor

heterogeneity and plays a major role in determining the outcomes of chemotherapy. Tumor cells are shielded within this matrix and connected to the blood circulation through the previously discussed aberrantly-formed vasculature.

Tumor hypoxia, acidity, and increased interstitial fluid pressure. Three major features characterize the nature of the tumor matrix, namely hypoxia, extracellular acidity, and increased interstitial fluid pressure (IFP). Hypoxia is a feature of many solid tumor cores, where the ill-formed vasculature become unable to deliver oxygen and nutrients to deep tumor tissues, which lie more than 100 μm from the nearest blood vessel [145;146]. These cells can no longer depend on oxidative metabolism to produce ATP, and rather revert to glycolysis, which, along with nullified lymphatic drainage, results in the accumulation of lactate within the deep tumor tissues, lowering the extracellular matrix pH [145]. Although hypoxic cells are viable, they are usually accompanied with necrotic tissues. Unfortunately, these untoward conditions results in the selection of 'elite' cancer cells with outstanding resistance capabilities, as hypoxia induces tumor evolution, oncogene expression, apoptosis resistance (via selection of cells with lost p53 sensitivity) [147], and metastasis [144;148;149].

Both hypoxia and the acidic extracellular environment contribute to cancer chemoresistance via several mechanisms. Hypoxia stabilizes hypoxia-inducible factor 1α (HIF1 α), which leads to the upregulation of drug resistance genes, including multi-drug resistance 1 (MDR1) gene and P-gp-encoding gene [145;150]. Drugs that rely on free-radical formation will experience reduced activity (e.g., bleomycin), whereas those that

are weak bases (e.g. doxorubicin) will be ionized in the extracellular matrix, and thus their internalization will be hindered [138;151]. In addition, hypoxic conditions tend to abolish the efficacy of radiation therapy [101].

Another common feature of most solid tumors is the increased interstitial fluid pressure (IFP), which can massively hinder the efficient delivery of chemotherapeutics [152;153]. The defective lymphatic drainage, the accumulation of metabolic products in the hypoxic environment, and the imperfect structure of the hastily-formed vasculature significantly contribute to this phenomenon [138;153;154]. The rapidly dividing tumor cells and the dense cross-linked ECM structure not only compress the blood and lymph vessels, but also do not expand enough to allow edema formation, which can alleviate the increased IFP [98;154]. The fenestration that characterize the leaky tumor vasculature may not be enough to deliver nano-carriers to the tumors in such cases, as the expected extravasation into tumor tissues may also be accompanied by an intravasation into the blood vessels, which demolishes any benefit that the nano-carriers may have to reach tumors [98]. Variability of IFP contributes to the heterogeneity of tumors and complicates the predictability of clinical outcomes from chemotherapy [146].

Tumor associated macrophages. Tumor-associated macrophages (TAMs) are part of the inflammatory cells in the tumor microenvironment. The link between inflammation and cancer development is well-established [155;156]. TAMs usually originate from peripheral circulating monocytes that are recruited by the tumors [157]. However, some of them may locally proliferate within the tumor environment [158]. Although

macrophages may be expected to fight against the rapidly- and aberrantly-proliferating tumor cells, interestingly enough, there is strong evidence that tumor cells are not only able to block the antitumor activity of the immune cells, but also 'enslave' the TAMs to serve their cause by helping the tumor cells proliferate, nourish, and progress [157-159]. TAMs improve tumor angiogenesis, invasiveness, metastasis, and immune system suppression, and have been linked with poor prognosis [155;160;161]. Several chemoattractants expressed by tumor and endothelial cells are involved in TAM recruitment, which include monocyte chemoattractant protein-1 (MCP-1, CCL2), macrophage inflammatory protein-1α (MIP-1α, CCL3), vascular endothelial growth factor (VEGF), and colony stimulating factor 1 (CSF-1) [157;160]. The evident role of TAMs in tumor progression qualifies them as a potential target for nanomedicine-based chemotherapy.

Cancer-Associated fibroblasts. Cancer-associated fibroblasts (CAFs) are the most abundant cells within the stroma in many tumors, including breast and pancreatic cancers, and are the main source of ECM components [162-164]. Fibroblasts are mesenchymal non-inflammatory cellular components of the connective tissues, although they regulate inflammation and wound healing, and they secrete fibrillar components of the ECM (like type I, III, and IV collagens) [163]. They become activated in wound healing and fibrosis (called myofibroblasts) and start *de novo* expression of a type of filamentous actin, α-smooth muscle actin (α-SMA) [162;164-166]. Since cancer may be regarded as 'inflammation that never heals' [167], CAFs share a lot of similarities with activated

fibroblasts associated with wound healing, including α-SMA expression (commonly used to identify CAFs) [163;165;168] to act as a scaffold for other ECM components. However, they do not deactivate or undergo apoptosis, like activated fibroblasts, after inflammation subsides [164], mainly because tumors are persistent. Fibroblasts in tumor stroma may exist as activated or non-activated form, but the vast majority of CAFs are the activated form (e.g., 80% of fibroblasts in mammary tumors are in the activated form) [163;168]. CAFs are involved in tumor progression and metastasis via secretion of a panel of cytokines that stimulate the excretion of MMPs, which predispose metastasis and provide support for tumor cell proliferation [168;169].

After this brief overview of the tumor microenvironment, it should be clear that exploiting the anticancer activity of a nanomedicine in cell culture is not sufficient. In the literature, the *in vitro* cytotoxic evaluation is usually accepted as a means to ensure that the chemotherapeutic agent still retains its activity within the formulation. In the following section, the role of nanomedicine in overcoming the tumor microenvironment barriers, including ongoing clinical trials, will be overviewed.

1.4.2.2. Application of nanomedicines to breach or to take advantage of tumor microenvironment barriers to improve drug delivery.

A successful anticancer agent should be able to simultaneously deal with as much of these barriers as possible. Combination drug or drug/adjuvant therapy can provide a multi-target modality. However, toxicity associated with such cocktails can be expected. The versatility of nanomedicine-based approaches may help tackle multi-functional tasks

with minimum toxicity. In this section, nanomedicine approaches to breach tumor stroma, or to take advantage of some of the conditions specific to tumor microenvironment will be overviewed.

1.4.2.2.1 Depletion or modification of tumor stroma.

Hyaluronic acid. Hyaluronic acid (HA) is abundantly accumulated in almost all epithelial tumors (e.g., pancreatic ductal adenocarcinoma, PDAC), providing a viscoelastic matrix within the collagen fibers in the tumor, and is correlated with tumor proliferation, invasiveness, and poor prognosis [170;171]. HA also contributes to tumor progression, and its water retention capability helps increase the IFP [171]. The use of bovine hyaluronidase (HYAL) to breach the tumor ECM was assessed in various clinical trials during the late 1990's. Although promising results ranging from low or absent recurrence to prolonged patient survival were obtained when HYAL was combined with other anticancer drugs [172;173], the development of allergic reactions to bovine HYAL, which can be serious in many cases, hindered the widespread acceptance of this approach [170]. Researchers at Halozyme® Therapeutics developed a human recombinant HYAL (rHuPH20, Hylenex®) that was well tolerated in 100 human volunteers following intradermal injection [174] and was approved by the FDA later on. However, due to the very short half-life of this product, its use for cancer treatment was not feasible [171]. To further improve this product, the researchers, via conjugation of a 30K N-hydroxysuccinimidyl ester of methoxy-polyethylene glycol-butanoic acid to rHuPH20,

designed a PEGylated form of the enzyme (PEGPH20), which exhibited a 270-fold increase of *in vivo* half-life in mice, enabling its intravenous administration [171]. The PEGylated recombinant human hyaluronidase dramatically lowered the IFP via cleavage of the HA chains, releasing the entrapped water and decompressing the previously collapsed tumor vasculature, in transgenic mice with metastatic and invasive PDAC [175;176]. The combination of PEGPH20 with gemcitabine dramatically suppressed metastasis and significantly prolonged the survival of transgenic mice with PDAC, compared to gemcitabine alone (91.5 days vs. 55.5 days, respectively, $p = 0.004$) [175]. The administration of PEGPH20 3 h before liposomal doxorubicin showed a 4-fold increase in doxorubicin accumulation in high HA-tumor xenografts, compared to liposomal doxorubicin alone [171]. In a different context, Yang *et al.* designed a lipid-based nano-carrier for the taxane drug paclitaxel. They decorated the surface of the nano-carriers with oligo-fragments of HA (oHA) that result from the breakdown of the latter by HYAL [177]. They proposed that the use of oHA, which can replace the endogenous HA on its binding sites in CD44 receptors overexpressed on cancer cells, will not only provide an efficient targeting modality for HA-rich breast tumors, but also help breach the HA coat on tumors by CD44 receptor competition [177]. This strategy successfully sensitized the tumors to paclitaxel nano-carriers, which showed a significantly stronger anticancer activity compared to the non-decorated nano-carriers [177].

Hedgehog pathway. Stromal depletion becomes critical in dealing with deadly tumors like PDAC, where the stromal structure is tremendously dense. PDAC is one of the

deadliest cancers, with a median survival of few months, which can be extended for few more weeks when the standard first line treatment gemcitabine is used [178]. The fibroblasts-rich, rock-solid, almost avascular, desmoplastic tumor stroma acts as a mechanical barrier against the intratumoral delivery of gemcitabine, which already suffers from a short circulating half-life and extensive deamination [139;179;180]. Olive *et al.* (2009) described the efficient, yet transient, restoration of the diminished vasculature in a transgenic mouse model, via the co-administration of a hedgehog (Hh) pathway inhibitor IPI-926 with gemcitabine [180;181]. Inhibition of the stromal-associated pathway depleted the stromal matrix in the mouse model, which closely resembled human PDAC, and resulted in delivering more gemcitabine to the tumors, inhibiting the tumors growth, and prolonging the median survival of mice [181]. Unfortunately the tumors reverted back to the avascular state at the end. However, the positive results may provide new hopes to defeat the malign tumors. In a commentary on that study, Olson and Hanahan highlighted two mean aspects, dealing with the hedgehog pathway paradigm; the first one being that the tumor fights back to restore the hypoxic state, instead of the opposite in order to fulfill its craving to nutrients [180;181]. The other aspect is that this approach tends to 'vascularize' the tumor by inhibiting an anti-angiogenic pathway, which is contrary to the commonly known dogma of tumor vascular 'normalization', proposed by Jain, via treatment with angiogenic inhibitors to balance the 'super-active' pro-angiogenic activity of tumors [103;104;152;180;181]. Although positive results have been reported in early clinical studies with GDC-0449 (vismodegib, Genentech®) plus gemcitabine, or saridegib plus gemcitabine, phase II clinical trials with

the latter combination in previously untreated patients with metastatic PDAC failed to show any advantage and were stopped short [139]. This is not the end for Hh inhibitors though. Vismodegib was granted the FDA's priority review program approval in 2012 to treat advanced basal-cell carcinoma, and other Smoothened (Smo, the transmembrane protein whose reversal of repression is a major step in the Hh pathway) inhibitors (e.g., LDE 225, Novartis®) are still under clinical trials [182]. In the same regard, a nanomedicine formulation of a hedgehog inhibitor showed some promises in pre-clinical studies [183;184]. The PEGylated polymeric nanoparticle formulation (PLGA-PEG) of a hedgehog pathway inhibitor HPI-1 could overcome the mutational resistance of orthotopic pancreatic tumors against commonly used Hh inhibitors in mice [184], and inhibited metastasis in a hepatocellular carcinoma model [183].

SPARC. Secreted protein, acidic and rich in cysteine (SPARC), also known as osteonectin, is a glycosylated 43 kDa protein that is overexpressed in the PDAC stroma and at the invasion front of the tumor. It is usually associated with poor prognosis clinically in patients with high expression in the peritumoral fibroblasts, rather than in cancer cells [185-187]. Two groups of ECM-associated proteins are known: 1) structural proteins (e.g., collagens), and 2) non-structural or matricellular proteins (e.g., SPARC) [188]. Albumin-bound paclitaxel (*nab*-paclitaxel, Abraxane®), in an active combination regimen with gemcitabine, achieved 12.2 months overall survival (OS) and 48% 1-year survival (compared to 5.7 months and 20%, respectively, with the standard therapy with gemcitabine) in a phase I/II clinical trial [189]. Furthermore, a phase III clinical trial in

patients with metastatic PDAC revealed that the combination achieved an OS of 8.5 months (431 patients) vs. 6.7 months with gemcitabine monotherapy (430 patients), and a 1-year survival of 35% with the combination therapy vs. 22% with gemcitabine alone [190]. The fact that albumin-bound nano-carriers are transcytosed into the cells following binding to albumin specific receptors (e.g. gp60) [186] may not be enough to explain the improved clinical benefit achieved in the clinical trials, as the question remains: how could the 10-nm circulating albumin-paclitaxel complexes penetrate into the dense desmoplastic stroma that not only comprises a physical barrier against deep tumor penetration, but also keeps the tumor cells away from the already-poor vasculature? In a preclinical study concurrently carried out with the same phase I/II clinical study mentioned above using nab-paclitaxel with gemcitabine, Von Hoff *et al.* found that the use of nab-paclitaxel depleted the stroma of a pancreatic cancer xenograft tumors in nude mice, which facilitated the gemcitabine delivery to the tumors (2.8 times higher than what was achieved with gemcitabine alone). The stromal depletion effect was associated with dilated blood vessels and increased endothelial cell content in the stroma. The stromal depletion and improved vascularization are believed to improve gemcitabine penetration into the tumors and brought the tumor cells closer to vasculature [189]. The cornerstone finding in this study was that SPARC was the Achilles' heel within the dense stroma of the PDAC, as the strong affinity between the overexpressed SPARC and albumin in nab-paclitaxel brought the nano-aggregates (i.e., nab-paclitaxel) deeper into the tumors, breaching the stroma, and bringing more gemcitabine deep inside [186;189;191]. Similar findings were also reported with head and neck cancer tissues

[187]. Another factor that contributes to the improved efficacy of gemcitabine when nab-paclitaxel was concurrently administered is that the nab-paclitaxel was found to lower the cytidine deaminase levels in a murine pancreatic cancer model [192]. Cytidine deaminase is responsible for the extensive deamination of gemcitabine (more than 90%), yielding the inactive compound 2'-deoxy-2',2'-difluorouridine (dFdU) [179;193].

α-SMA. Li and colleagues developed a PEG-docetaxel-acetylated carboxymethylcellulose conjugate that can self-assemble and form nanoparticles of about 120 nm. This formulation (Cellax) was shown to be more efficacious than commercial solvent-based docetaxel and nab-paclitaxel in both *in vitro* and *in vivo* studies [194-197]. Docetaxel conjugation percentage was high (> 30 wt%), and it was completely and slowly released following a near zero-order pattern within 3 weeks [197]. In a recent study that thoroughly investigates the tumor stroma involvement in the anticancer activity of Cellax, the authors reported that Cellax significantly depleted the stroma of orthotopically implanted mammary tumors (4T1 and MDA-MB-231), with an about 70-fold increase in tumor perfusion and about 3-fold suppression of IFP, while minimum or no effect was noticed following either solvent-based docetaxel or nab-paclitaxel, in the same tumor models [169]. In addition, and more importantly, lung metastasis was also reduced by 7- to 24-fold following Cellax treatment, whereas the solvent-based docetaxel increased the number of metastatic lesions in the lungs [169]. One day after intravenous injection of Cellax, the authors found that the vast majority of Cellax nanoparticles (85%) co-localized with α-SMA-positive stromal cells, and the α-SMA

content in tumors declined from about 30% down to 0% within 1 week, which indicates the stromal-depleting effect of the nanoparticles [169]. Interestingly, tumor epithelial cells population started to decline only 7 days after the initiation of the treatment (i.e., after α-SMA depletion took place). Early investigation of the mechanism of Cellax-stroma interaction revealed that the albumin adsorbed on the circulating Cellax may favor the albumin-SPARC stromal penetration pathway [169], similar to that reported for the nab-paclitaxel [189]. The fact that SPARC expression is also associated with α-SMA-positive CAFs supports this proposed mechanism [169]. However, the failure of nab-paclitaxel to outweigh the Cellax performance in this tumor model sheds some questions on the influence of the tumor model on the stromal-depletion effect of the former.

1.4.2.2.2 Stimuli-responsive nano-carriers.

This approach takes advantage of specific characteristics that are exclusively exhibited in the tumor microenvironment to improve the antitumor activity of the chemotherapeutics. Various tumor environmental stimuli are involved in this approach, including lower extracellular pH, hypoxia, and MMP overexpression. Stimuli-sensitive nano-carriers have been extensively reviewed in literature (see [198-201]). This section provides a brief overview of the most common approaches employed to increase nano-carrier penetration into tumors.

Andresen *et al.* developed a liposomal formulation, composed of a serum-stable prodrugs of a group of cytotoxic lipid agents (anticancer etherlipids, AELs, also called cytotoxic lysolipids) for selective tumor site-activation and release of the active drug [202;203]. The AELs were made into phosphorylated prodrugs (proAEL) by

modification with a stable ether bond that is not hydrolysable in plasma, but is sensitive to a class of phospholipase A2 (PLA2), called secretory PLA2 (sPLA2), which is overexpressed in the tumor microenvironment. The prodrugs self-assemble into liposomes that can accumulate via EPR into tumor tissues, where the sPLA2 hydrolyzes the prodrugs, releasing the potent AELs in the tumor microenvironment [202]. Furthermore, the fatty acid by-products of the hydrolysis may also act as tumor cell permeation enhancers to improve the cellular uptake of AELs. This formulation successfully overcame the red blood cell toxicity issues encountered with the use of AELs, as the ether-based prodrugs are stable in plasma, and the liposomal nature of the prodrugs enables the encapsulation of water soluble drugs into the core of the liposomes [202;203].

Several pH-sensitive block-copolymers have been utilized to deliver drugs in the acidic extracellular matrix, while pre-mature drug leakage is minimized. Bae and co-workers developed a novel doxorubicin-loaded mixed micelle formulation that is destabilized in acidic pH to release doxorubicin [204]. The mixed micelle system was composed of poly (L-histidine)/PEG and poly (L-lactic acid)/PEG (polyHis/PEG and PLLA/PEG). As the polyHis moiety is protonated in the acidic condition, the critical micelle concentration (CMC) of the amphiphilic molecule increases, which disassembles the whole micelle structure [200;204;205]. The pH at which the formulation destabilizes can be controlled by varying the ratio between the two block-copolymers [204].

The idea of pH-dependent shedding of PEG chains has been described in literature for several purposes [200;206-209]. Poon *et al.* designed a layer-by-layer (LBL)

nanoparticle platform, where the cationic poly (L-lysine), functionalized with iminobiotin (inner layer) is further decorated with biotin-functionalized PEG chains (outer layer), through a neutravidin linker (middle layer) [206]. The quantum dots-loaded nanoparticles are designed to shed PEG chains via decomposition of the acid-sensitive iminobiotin-neutravidin at the acidic pH of the hypoxic tumor microenvironment. This will bring the cationic poly (L-lysine) layer to surface, which improves the nanoparticles internalization [206], as the PEG layer, although useful for prolonged circulation, is expected to hinder efficient cellular uptake [39;210]. A conventional biotin-avidin-based PEGylation strategy was used to prepare non-pH-sensitive nanoparticles for comparison. Although the tumor accumulations of nanoparticles in the first 8 h were not different between the pH-sensitive and non-sensitive formulations, the pH-sensitivity improved the nanoparticles accumulation after 24 and 48 h. Furthermore, histological evaluation showed that the pH-sensitive nanoparticles were associated with hypoxic regions. Early accumulation (within 8 h after injection) was assumed to be independent of the pH-sensitivity, and was rather dependent on the EPR effect, which is not expected to favor the delivery of either formulation [206].

In the same regard, Sawant *et al.* designed a multifunctional 'smart' nano-carrier that has a long-chain PEG-phosphoethanol amine (PEG-PE) moiety attached to an mAb for active targeting, while shorter PEG-chains are attached to a cell penetrating peptide (e.g., Tat peptide) [207]. The design involved inserting a pH-sensitive hydrazone bond in between the long-chain PEG and PE to render this moiety pH-sheddable. After the nano-carriers reach tumors by the help of the mAb-conjugated PEG, the long PEG chains are

shed due to the hydrolysis of the acid-sensitive hydrazone bond, exposing the Tat-conjugated PEG, which can then improve the internalization of the nano-carriers into tumor cells [205;207]. In a recent study, Zhu *et al.* applied the idea of hydrazone-based PEG-shedding to actively target TAMs [211]. The nanoparticles are composed of PLGA core (with 5% PLGA-FITC), stearoyl-mannose (C18-mannose), and PEG-hydrazone-stearoyl (PEG-hydrazone-C18, PHC). The stearoyl moiety in both PHC and C18-mannose are expected to be inserted into the lipophilic PLGA core, leaving the short mannose and the long PEG moieties projecting outwardly. Once the long-circulating nanoparticles accumulate in the tumor via EPR, the PEG chains are shed in the acidic tumor environment (pH 6.8), bringing the mannose moiety to the front, which enables the nanoparticles to interact with TAMs via mannose-mannose receptor interaction [211]. In contrast, nanoparticle uptake by normal macrophages at physiological pH is hindered by the shielding effect of the PEG chains [211]. This formulation provided a successful tool for the active targeting of TAMs.

Using PEG-shedding to expose another hidden surface targeting ligand can take place via other mechanisms as well. For example, Torchilin's group designed an MMP2-sensitive micellar formulation that sheds PEG chains and exposes a cell penetrating Tat-peptide once the micelles reach the MMP2-rich tumor microenvironment [212]. The shed PEG chains, which are connected to the MMP sensitive peptide, are long (2 kDa) to provide extended plasma circulation of the micelle formulation, while the Tat-peptide-conjugated PEG chains are shorter (1kDa) to keep the Tat shielded until the micelles reach tumor microenvironment. Paclitaxel, conjugated to the MMP-sensitive PEGylated

moiety, remained at the core of the Tat-peptide decorated micelle structure due to its lipophilic nature [212].

1.4.3 Cellular Barriers.

1.4.3.1 Nano-carrier internalization by cancer cell and endosomal escape.

Once the nano-carrier gets past all the previously mentioned barriers, it comes in contact with the tumor cells and starts to interact with tumor cell membrane to get internalized (endocytosis). The process of endocytosis starts with invagination of the nano-carriers into the cell, forming a specific vesicle (endosome or phagosome), in which the nano-carriers are entrapped. Five major endocytic pathways for the internalization of nano-carriers have been identified, namely phagocytosis, macropinocytosis, clathrin-mediated endocytosis, caveolin-mediated endocytosis, and clathrin/caveolin-independent endocytosis [120;213;214]. The type of endocytosis depends on several factors, including nano-carrier size, surface chemistry and ligands, and the tumor cells [120]. Caveolin and clathrin are proteins assisting the endosome formation and the endocytosis process. The pH inside several internalized vesicles is usually acidic, with various values. Both clathrin-mediated and caveolin-mediated endocytosis form early endosomes (pH 6.5-6.8), which become late endosomes (pH 5.2-6.2), while phagocytosis and macropinocytosis form phagosomes and macropinosomes, respectively. All three vesicles deliver their cargos to lysosomes (pH 4.5-5.2) [213]. Both the acidic conditions and the presence of hydrolytic enzymes facilitate the digestion of the internalized cargos and destroy them.

Thus, it is important that the nano-carriers find a way out of the endosomes before reaching the terminal lysosomes [215]. Among the methods adopted to enable the endosomal escape of nano-carriers from the endosomes is the proton-sponge effect method, where nano-carriers with secondary or tertiary amine groups (e.g., poly-L-histidine, polyethylene imine (PEI), or chitosan) are protonated by the acidic pH inside, which results in the extensive flow of ions and water inside the endosomes, resulting in osmotic swelling and subsequent rupture of the lysosomes. The nano-carriers then escape into the cytosol [215;216]. Other endosomal escape mechanisms include the use of fusogenic peptides (e.g., influenza HA2 peptide and GALA peptide) that destabilize the endosomal membrane after some acid-sensitive conformational changes of their structures take place[217;218].

In one example, nevertheless, it seems like what comprises a ‘curse’ to some nano-carriers turns out to be a ‘blessing’ to others. Wonganan *et al.* found that the GemC18-SLNs are taken up by tumor cells by clathrin-mediated endocytosis, and the gemcitabine is liberated in lysosomes due to acid-sensitive hydrolysis and lysosomal enzymes such as cathepsins [219]. Free gemcitabine is then likely exported out of the lysosomes by human equilibrative nucleoside transporter-3 (hENT-3) in the lysosomal membrane. It seems that, following this pathway, the liberated gemcitabine is shuttled into a natural ‘salvage’ pathway that cells adopt to recycle endogenous (e.g., apoptotic bodies) or exogenous DNA (e.g., DNA from bacteria or viruses), and is phosphorylated more efficiently into the active difluoro-deoxycytidine triphosphate (dFdCTP) to inhibit cell growth [219]. In this case, functional lysosomes are critical to efficiently generate

dFdCTP, as alkalinization of lysosomes with ammonium chloride significantly inhibits the cytotoxic action of GemC18-SLNs [219]. In contrast, the GemC18 diffuses inside tumor cells very rapidly and is hydrolyzed quickly into free gemcitabine. However, it appears that the gemcitabine that reaches cell cytosol following this pathway cannot be efficiently phosphorylated into its active dFdCTP. Gemcitabine alone can be effectively taken up by cells via nucleoside transporters such as hENT-1 located in the cell membrane. However, it is extensively deactivated into its inactive dFdU derivative before being phosphorylated [219]. For a more detailed description of this example, the reader is referred to ([219])

1.4.3.2 ATP-binding cassette transporters (ABC transporter, efflux transporter-mediated resistance)

ABC transporters are a family of proteins that include multidrug resistance protein-1 (MDR-1) and P-glycoprotein (P-gp) [138]. Human P-gp, a 170 kDa trans-membrane glycoprotein, is composed of 12 hydrophobic domains and 2 nucleotide domains [220], and is a major component of the blood brain barrier [221]. It can transport several small molecules, either from the cytosol or from the cell membrane, out of the cell, which significantly reduces cellular accumulation of cytotoxic molecules [138;222]. The mere use of a nano-carrier to deliver the chemotherapeutic agents intracellularly had been shown to overcome the P-gp-mediated efflux [223], as the nano-carrier is not a substrate to the protein. Additionally, several nano-carrier based approaches, including the concomitant use of efflux inhibitors (e.g., cepharanthine [224] and tariquidar [225]),

silencing the gene encoding P-gp [226;227], and the use of certain excipients and surfactants (e.g., poloxamers and tocopheryl-polyethylene glycol succinate (TPGS) [228;229]), are among the strategies that have been explored to reverse ABC transporter-mediated multi-drug resistance to nanomedicine.

For example, Panyam and co-workers developed a biotin-functionalized PLGA nanoparticles that encapsulate a dual drug payload of paclitaxel and the third generation P-gp inhibitor tariquidar to target the biotin receptors overexpressed by tumor cells [225]. Within a concentration range at which neither paclitaxel in solution or in nanoparticles was effective, tariquidar enhanced the cytotoxic effect of paclitaxel, both in solution and in nanoparticles, in chemoresistant cell lines that overexpress P-gp. Furthermore, the 2 h-cellular uptake of paclitaxel was the greatest when tariquidar was co-encapsulated with paclitaxel in PLGA nanoparticles. The authors attributed the lack of activity of paclitaxel nanoparticles in these cell lines to the overexpressed P-gp, as the slowly released paclitaxel is readily removed by P-gp. However, the simultaneous slow release of tariquidar inhibited P-gp and accordingly enhanced the accumulation of the slowly released paclitaxel. The dual agent encapsulation in the biotin-functionalized nanoparticles significantly enhanced the antitumor activity and survival in mice bearing resistant tumors [225]. The same group also showed that simultaneous encapsulation, and subsequent intracellular co-localization, of paclitaxel and a P-gp-silencing siRNA can successfully enhance the anticancer activity of paclitaxel in resistant cells [230]. Using a different modality, Navarro *et al.* showed that the pretreatment of resistant breast cancer cells with siRNA, loaded on a cationic PEI-functionalized phospholipid-based nano-

carrier, can significantly enhance the cytotoxic activity of a subsequent treatment with doxorubicin solution [226]. Other cellular-mediated ABC transporter-independent resistance mechanisms to chemotherapy include apoptosis inhibition and DNA repair modification [205]. For example, survivin is an antiapoptotic protein that is overexpressed in cancer cells. and the silencing of survivin gene expression has been identified as a successful tool to overcome drug resistance in cancer cells [231;232]. Yang *et al.* functionalized the polysaccharide chitosan with a cell penetrating peptide and utilized it to deliver survivin siRNA [233]. The siRNA-chitosan complexes effectively induced apoptosis in cancer cells and inhibited the tumor growth in mice with orthotopic mammary tumors, while the naked siRNA was not effective [233]. For deeper insights on the use of nanomedicine to overcome cellular-mediated drug resistance mechanisms in tumors, the reader can refer to [138;205;221;234;235].

1.5 Conclusion

Nanomedicine opens a totally different horizon in cancer chemotherapy, with so many opportunities waiting. However, as more opportunities come in the way, more challenges are also revealed. More efforts are needed to fully take advantage of its potentials.

Chapter 2

Solid lipid nanoparticle formulations of docetaxel prepared with high-melting point triglycerides: i*n vitro* and i*n vivo* evaluation [2]

2.1 Introduction

Docetaxel (DCX) is a second generation taxane, derived from the inactive 10-deacetyl baccatin III, extracted from the European Yew tree (*Taxus baccata*) [236;237]. DCX has better water solubility, pharmacokinetic profile, and anticancer activity than paclitaxel [236;238]. Current FDA approved DCX products, including Taxotere®, are essentially Tween 80/ethanol-based solutions [239], which unfortunately are associated with various significant side effects. They induce marked hypersensitivity, neutropenia, fluid retention, and alopecia [239-241]. Hypersensitivity reactions, which are attributed to the Tween 80 in the formulations, vary from simple skin rash to systemic anaphylaxis [239;242], and necessitate premedication with corticosteroids [243]. Other problems associated with the Tween 80/ethanol-based DCX formulations include the non-specific accumulation of DCX in healthy organs, which may lead to systemic toxicity and subsequent discontinuation of therapy [86].

Nanoparticle-based, Tween 80-free DCX formulations are expected to not only avoid Tween 80-related side effects, but also increase the concentration of DCX in tumors due to the enhanced permeation and retention (EPR) effect [86;88;239].

---

[2] This chapter is based on "*Youssef W. Naguib, B. Leticia Rodriguez, Xinran Li, Stephen D. Hursting, Robert O. Williams, and Zhengrong Cui,* ***Molecular Pharmaceutics****, 2014, 11(4): 1239-1249"*

Data from many previous studies show that nanoparticles of 100-200 nm are the most successful in tumor vasculature extravasation [31;120], although there are disagreements in the literature [88;91;109;244-246]. The heterogeneous nature of tumor type, size, location, and metastasis may contribute to the disagreements [94]. In order to improve the EPR-related nanoparticles extravasation, nanoparticles should be designed to circulate longer in the blood, while the drug of interest is retained within the nanoparticles [44]. PEGylation is a strategy to render the surface of nanoparticles hydrophilic, which enables the nanoparticles to evade early opsonization and circulate longer in the blood [125;247]. On the other hand, for a drug to be retained within the nanoparticles, a strong affinity between the drug and the excipient(s) used to prepare the nanoparticles is required [44].

Solid lipid nanoparticles (SLNs) have been extensively investigated as drug carriers [42;248-250]. Advantages of such nano-carriers include high compatibility with lipophilic drugs, ease of fabrication, and controlled release [37;42;44;250]. Various SLN formulations of taxanes have been previously reported [38;251-253]. Heurtault *et al*. reported the development of a PEGylated lipid nano-capsule formulation (LNCs) for paclitaxel using a novel phase inversion-based method [254]. The resultant LNCs were made of an oily medium-chain triglyceride core and stabilized with soybean lecithin as a lipophilic surfactant, and PEG hydroxystearate (Solutol®) as a hydrophilic surfactant [254-256]. Lee *et al*. applied a high pressure homogenization technique to prepare a SLN formulation of paclitaxel using triglyceryl myristate (trimyristin) and phospholipids [253]. The formulation showed improved *in vitro* activity [253], but the *in vivo*

circulation time and biodistribution profile were not improved, as compared to the market product Taxol® [257]. Videira *et al*. applied a factorial design to optimize formulation parameters to prepare paclitaxel SLN formulations using Compritol 888 ATO® (a mixture of mono-, di-, and triglycerides of behenic acid) and Precirol ATO5® (i.e., glyceryl palmito-stearate), and the final optimized formulation exhibited improved *in vitro* cytotoxic activity against the murine breast cancer cell line MXT-B2 [258].

The present study aimed at the rational selection of a triglyceride from a list of medium- and long-chain triglycerides for the development of a SLN formulation to ultimately improve the antitumor activity of DCX. Previously it was reported that low melting point triglycerides are excellent solubilizers for DCX [259], prompting us to hypothesize that high melting point triglycerides will be suitable excipients for preparing DCX-incorporated SLNs. Triglycerides that are solid at body temperature were selected to ensure formulation stability and to avoid droplet coalescence [253]. An oil-in-water (O/W) emulsion-based method was applied, where DCX and all lipid components were dissolved in the oil phase, and the aqueous phase consisted of a 0.1% (w/v) Poloxamer 188 aqueous solution. Finally, the *in vitro* and *in vivo* antitumor activities of the selected formulation were evaluated.

2.2 Materials and Methods

2.2.1 Materials

DCX was from LC Laboratories (Woburn, MA, USA). The 1,2-dioleoyl-sn-glycero-3-phosphoethanoamine-N-[methoxy (polyethylene glycol)-2000] (DOPE-PEG-2000) and phosphatidylcholine from chicken egg (ePC) were from Avanti Polar Lipids, Inc. (Alabaster, AL, USA). Sepharose® 4B, MTT (3-(4,5-dimethylthiazol-2-yl)-2,5-diphenyltetrazolium bromide) kit, Tween 80 (T80), Poloxamer 188 (Pluronic F68®), trimyristin (TM), trilaurin (TL), tristearin (TS), tripalmitin (TP), mannitol, sucrose, phosphate buffer saline (PBS, pH 7.4), triglyceride assay kit, and caspase 3 assay kit were all from Sigma-Aldrich (St. Louis, MO, USA). Float-A-Lyzer dialysis tubes (MWCO 50,000) were from Spectrum Chemicals & Laboratory Products (New Brunswick, NJ, USA).

2.2.2 Cell lines and animals

TC-1 cells (murine lung cancer cell line) were from the American Type Culture Collection (ATCC, Rockville, MD, USA) and grown in RPMI 1640, supplemented with 10% fetal bovine serum (FBS) and 1% of 100 μg/ml streptomycin and 100 IU/ml penicillin (1% P/S). M-Wnt cells (murine mammary gland cell lines) were from Dr. Stephen D. Hursting's lab at The University of Texas at Austin. M-Wnt cells were grown in a similar medium as TC-1, with an additional supplement of 1% Glutamax®. Human breast adenocarcinoma cells (MDA-MB-231) were from ATCC and grown in DMEM

supplemented with 5% FBS and 1% P/S. All cell culture reagents were from Invitrogen™ (Life Technologies, Carlsbad, CA, USA). Female C57BL/6 mice (6-8 weeks old) were from Charles River Laboratories (Wilmington, MA, USA).

2.2.3 Preparation of SLNs

SLNs were prepared using a modified emulsion/solvent evaporation method. Briefly, 1 ml of dichloromethane (DCM) containing DCX, a triglyceride (TM, TP, TL, or TS), egg PC, and DOPE-PEG-2000 in a weight ratio of 1:20:10:2 was added to 10 ml of 0.1% Poloxamer 188 aqueous solution in a glass vial, and the mixture was sonicated using a probe sonicator, with a micro-probe attached, for 40 s, at a sonication intensity of 50% (Q-sonica LLC, Newtown, CT, USA). The glass vial was placed in an ice bath during sonication to prevent heat accumulation. The emulsion was stirred for 15 min at 400 rpm in a water bath (65° C) to evaporate DCM, and was then stirred for 1 hour at room temperature. The resultant nanoparticle suspension was concentrated to 1 ml by ultrafiltration using an Amicon® device (Millipore Inc., 30,000 MWCO) (490 x *g*, 25 min, 4°C) as previously reported [260]. Finally, SLNs were briefly sonicated to eliminate aggregates due to the concentration process. DCX-free SLNs were prepared similarly without the addition of DCX. For SLNs that were used in animal studies, the ultrafiltration period was extended to 60 min to further concentrate the suspension. The prolonged ultrafiltration did not result in any significant particle size change (data not shown). SLNs were lyophilized using a Freezone freeze dryer (Labconco Corp., Kansas City, MO, USA) with 9.25% (w/v) sucrose as a cryoprotectant. The Tween 80/ethanol-

based DCX formulation (DCX in T80/E) was prepared by dissolving DCX in Tween 80 (20 mg/ml). This concentrate was then diluted with water/ethanol solution to make a final DCX solution of 4 mg/ml. The final concentrations of Tween 80 and ethanol in the solution were 20% (v/v) and 13% (v/v), respectively.

2.2.4 Determination of particle size and zeta potential

Particle size and zeta potential of the SLNs were measured using a Malvern Zetasizer Nano ZS (Malvern Instruments, Worcestershire, UK). Briefly, 20 μl of the concentrated SLNs in suspension were diluted to 1 ml with water, and the particle size and zeta potential were determined at room temperature.

2.2.5 Transmission electron microscopy (TEM)

The SLNs were examined using an FEI Tecnai Transmission Electron Microscope (FEI Corporate, OR, USA) at the Institute for Cellular and Molecular Biology, Microscopy and Imaging Facility at The University of Texas at Austin as previously reported [208].

2.2.6 Determination of DCX content and loading percentage in the SLNs

The content of DCX in the SLNs was determined using HPLC after extraction as previously reported with modifications [253]. Briefly, SLNs in suspension were diluted 5-10 times with methanol in a glass vial, which was placed in a water bath (65°C) for 20 min to dissolve the lipids, and placed at -20°C for 45 min. The supernatant was collected

by centrifugation at 18,000 g for 10 min at 4°C (Beckman Coulter Inc., Brea, CA, USA), and 5 μl of the supernatant was used for HPLC assay as previously described [210]. The HPLC system consisted of an Agilent HPLC workstation (Agilent Corp., Santa Clara, CA, USA), with RP-C18 column (Zorbax Eclipse, 5 μm, 4.6 mm × 150 mm; Santa Clara, CA, USA). The mobile phase was acetonitrile and water (1:1, v/v). The flow rate was 1 ml/min, and the detection wavelength was 230 nm. The DCX loading percentage was measured using a similar procedure, with the exception of that the SLNs were lyophilized, and 5 ml of methanol were added to 5 mg of the lyophilized SLNs. The weight percentage of DCX in the SLNs (% w/w) was calculated based on the following formula [261]:

$$Drug\ loading\ \% = \frac{DCX\ weight\ (mg)}{SLNs\ weight\ (mg)} \times 100 \qquad \text{Equation 1}$$

2.2.7 Gel permeation chromatography (GPC)

To investigate whether free DCX coexisted with DCX-SLNs in the nanoparticle preparation, the SLNs (100 μl) were applied to a Sepharose® 4B column (6 mm x 30 cm) equilibrated with water, and the DCX-SLNs were eluted with water. Fractions of 0.5 ml were collected, and 0.3 ml of each fraction was lyophilized to determine the content of DCX as mentioned above. In addition, the absorbance of each fraction (100 μl) at 500 nm was measured using a BioTek Synergy™ HT Multi-Mode Microplate Reader (Winooski, VT, USA) to determine their turbidity, which was used as an indication of the presence of

nanoparticles in the fractions collected. Finally, the concentration of triglycerides in each fraction was also measured using a Sigma Triglyceride Assay Kit following the manufacturer's instruction.

2.2.8 Short-term stability study

DCX-SLNs prepared using different triglycerides were stored in parafilm-sealed vials at 4°C for eight days. Particle size, zeta potential, and DCX content were measured as mentioned above shortly after the preparation and on day 8 to monitor any change of these parameters.

2.2.9 *In vitro* release of DCX from the SLNs

The release of DCX from the SLNs made with different triglycerides was monitored using Float-A-Lyzer tubes (MWCO 50,000). Briefly, DCX-SLNs suspension was diluted to 1 ml with PBS and transferred to the dialysis tube, which was then placed in a 50 ml plastic tube containing 20 ml of release medium (PBS, 0.1 mM, pH7.4, with 1% Tween 80). The tubes were then placed at 37°C in an orbital shaker at 100 rpm (Max-Q 5000, Thermo Scientific, Waltham, MA, USA). At predetermined time points, the whole release medium was replaced with fresh medium to maintain sink condition, and DCX concentration was analyzed using HPLC as previously mentioned. The release of DCX from the DCX in T80/E formulation was evaluated similarly for comparison.

2.2.10 Modulated differential scanning calorimetry (mDSC)

For mDSC, a TA Instruments Model 2920 DSC (New Castle, DE, USA) was used, and the data were analyzed using TA Universal Analysis 2000 Software. Accurately weighed samples were placed in aluminum crimped pans. The ramp rate was 5°C/min, and the temperature range was from 10° C to 200° C. The modulation amplitude and period were 0.5°C and 40 s, respectively. Ultra high purity nitrogen was flowing through the sample chamber during the run. Samples included DCX, trimyristin, DCX-SLNs (prepared with trimyristin), blank SLNs, and the physical mixture of DCX and blank SLNs.

2.2.11 X-Ray Diffraction (XRD)

A Philips Model 1710 X-ray diffractometer (Philips Electronic Instruments Inc., Mahwah, NJ, USA) available in the Texas Materials Institute X-ray Facility at The University of Texas at Austin was used to analyze the crystallinity of DCX in the SLNs. Samples included DCX alone, DCX-SLNs (prepared with trimyristin), DCX mixed with blank SLNs, and blank SLNs.

2.2.12 Cell proliferation assay

Cells were seeded in 96-well plates at a density of 3,000 cells/well and incubated at 37°C with 5% CO_2 overnight. They were treated with various concentrations of DCX-SLNs (prepared with trimyristin), DCX in T80/E, Blank SLNs, or T80/E alone for 72 h. Cell viability was determined using an MTT assay as previously described [210]. IC_{50}

values were calculated using GraphPad prism (GraphPad software, Inc., La Jolla, CA, USA).

2.2.13 Caspase 3 activity assay

Caspase 3 activity was determined using a Sigma-Aldrich Caspase 3 Fluorimetric Assay Kit. In brief, TC-1 cells were seeded in 24 well-plates at 25,000 cells/well and incubated overnight. The cells were treated with DCX-SLNs (prepared with trimyristin), DCX in T80/E, Blank SLNs, or T80/E for 72 h. The concentration of the DCX was 0.01 μM. The cells were then washed with PBS and lysed. The cell lysate was centrifuged at 18,000 g for 10 min at 4°C. The supernatant was transferred to a clear-bottomed black plate and mixed with the assay substrate, acetyl-Asp-Glu-Val-Asp-7-amido-4-methylcourmarin (Ac-DEVD-AMC). The mixture was incubated for 6 h for the hydrolysis of the Ac-DEVD-AMC by caspase 3 to release the fluorescent AMC, which was quantified by measuring the fluorescence intensity at 360 nm (excitation)/460 nm (emission) according to the manufacturer's instruction. The unit of the caspase 3 activity was mol AMC/min/ml. A caspase 3 inhibitor (provided in the kit) was used to confirm that the fluorescence was due to caspase 3 activity. Total protein concentration in the cell lysates was determined using Bio-Rad DC® Protein Assay Kit following the manufacturer's instruction.

2.2.14 Evaluation of the antitumor activity of the DCX-SLNs in vivo

All animal protocols were approved by the Institutional Animal Care and Use Committee at the University of Texas at Austin, and the National Institutes of Health (NIH) guidelines for laboratory animal use and care were followed. Animals were left to acclimatize for at least 7 days upon arrival from the vendor. Each mouse was injected with the murine TC-1 lung cancer cells (5 x 10^5 cells per mouse) suspended in 100 μl of FBS-free RPMI 1640 medium subcutaneously in the shaved left flank. Six days after the implantation (day 6), mice were randomized into 4 groups, 7 mice per group, and injected intravenously via the tail vein with DCX-SLNs (prepared with trimyristin), DCX in T80/E, Blank SLNs, or 5% mannitol as a vehicle control. The dose of DCX was 15 mg/kg body weight. Mannitol was used to adjust the tonicity of the nanoparticle suspension. Injection was repeated on days 9 and 12 post-implantation. Tumor sizes were measured using a digital caliper, and tumor volumes were calculated using the following formula [39]:

$$Tumor\ volume\ (mm^3) = [Length\ (mm) \times Width\ (mm) \times Width\ (mm)] \times 0.5 \qquad \text{Equation 2}$$

On day 21, mice were euthanized to harvest tumor tissues, which were weighed, fixed in Zn formalin buffer for immunohistochemistry.

2.2.15 Immunohistochemistry

Tissue sample preparation for immunohistochemical evaluation was carried out in the Histology and Tissue Analysis Core at Dell Pediatric Research Institute (DPRI) at The University of Texas at Austin. The formalin-fixed tumor tissues were embedded in paraffin wax, sectioned, and stained with an antibody against CD-31 (Abcam,

Cambridge, MA, USA) as a marker for angiogenesis (n = 3) [39]. Slides were then scanned, and images were taken using the ScanScope XT (Aperio Technologies, Vista, CA, USA).

2.2.16 Biodistribution and tumor uptake

TC-1 tumors were implanted in female C57BL/6 mice as mentioned above. Three weeks after tumor implantation, mice were divided into 2 groups (n = 9-10); one group was injected with DCX in T80/E (equivalent to DCX dose of 16 mg/kg) via the tail vein, and the other group with DCX-SLNs prepared with trimyristin (equivalent to DCX dose of 16 mg/kg). Two or twelve hours later, 4-5 mice from each group were euthanized to collect tumor, liver, kidney, spleen, heart, lung, and blood samples. The organs and tumor tissues were weighed, and stored at -80^{o} C. The blood samples were mixed with an EDTA solution and allowed to stand for about 15 min and centrifuged (3300 g, 10 min, 4° C) to separate the plasma, which was stored at -80^{o} C. DCX was extracted from the samples using ethyl acetate, and DCX concentrations in the samples were determined using HPLC. Paclitaxel was used as an internal standard.

2.2.17 Statistical analyses

Statistical analyses were completed by performing ANOVA followed by Fisher's protected least significant difference procedure. A p-value of ≤ 0.05 (two-tail) was considered significant.

2.3 Results

2.3.1 Preparation of DCX-SLNs and selection of triglyceride in the SLNs

SLNs were prepared using a modified emulsion/solvent evaporation method. The nanoparticles were composed of DCX, a triglyceride, ePC, DOPE-PEG-2000, and Pluronic F68. The average particle size of SLNs produced using tristearin, tripalmitin, trimyristin, and trilaurin, as the triglyceride was 178.4 ± 2.3, 176.3 ± 3.9, 182.8 ± 2.0, and 150.7 ± 14.5 nm, respectively (Table 2.1). The polydispersity indices of all nanoparticle preparations were equal to, or below, 0.2. The zeta potential of the SLNs was approximately -30 mV. The content of DCX in the final SLNs was 2.4-2.8% (w/w) (Table 2.1).

The release profiles of DCX are shown in Figure 2.1. The release of DCX from the SLNs was slower, relative to the diffusion of DCX out of the DCX in T80/E formulation (Figure 2.1A). Only about 4.5-9% of the DCX was released from the SLNs formulation within the first 6 h, whereas about 31% of DCX diffused out of the T80/E formulation within the same time period (Figure 2.1A). The rate at which the DCX was released from the DCX-SLNs prepared with trimyristin was the slowest (Figure 2.1B).

During a short-term, 8-day stability study at 4°C, no significant change in particle size and DCX content in any of the four DCX-SLNs preparations was found (Figure 2.2A-B). However, the zeta potential of DCX-SLNs prepared with tripalmitin and trilaurin changed significantly (Figure 2.2C). Based on data shown in Figures 2.1 and 2.2, the DCX-SLNs prepared with trimyristin were chosen for further studies, because the

release of DCX from the SLNs prepared with trimyrstin as the triglyceride was the slowest, and the resultant DCX-SLNs were also relatively more stable.

2.3.2 Characterization of DCX-SLNs prepared with trimyristin as the triglyceride

Shown in Figure 2.3A are the GPC results for the DCX-SLNs prepared with trimyristin as the triglyceride. About 90% of the DCX that was eluted from the column was associated with the triglyceride and with the fraction that contained the nanoparticles (calculated based on the area under curves of the GPC profiles) (Figure 2.3A). TEM showed that the DCX-SLNs are spherical (Figure 2.3B). The SLNs were successfully lyophilized with 9.25% (w/v) sucrose as a cryoprotectant (data not shown).

DSC analysis of the DCX-SLNs, free DCX, blank SLNs, and blank SLNs mixed with DCX showed that DCX exhibited a characteristic melting peak at 167.4^{o} C (Figure 2.4A). The physical mixture exhibited an endothermic melting peak at 143.4^{o} C, which can be attributed to the presence of free DCX, as the blank SLNs did not show any distinct peak at that temperature. A characteristic DCX endothermic melting peak was also absent in the DCX-SLNs (Figure 2.4A). On the other hand, the presence of the endothermic melting peak of trimyristin at approximately 55-58^{o} C confirmed the solid state of the lipid within the SLNs (Figure 2.4A). Finally, XRD showed that a characteristic DCX peak was present in the physical mixture, but absent in the DCX-SLN composition (Figure 2.4B).

Table 2.1: Physical parameters of DCX-SLNs prepared with different triglyerides. Data shown are mean ± S.D. (n = 3).

SLNs	*Triglyceride*	*Particle size (nm)*	*Polydispersity index*	*Zeta potential (mV)*	*DCX loading (%, w/w)*
TS	Tristearin	178.4 ± 2.3	0.181	-29.6 ± 2.3	2.6 ± 0.2
TP	Tripalmitin	176.3 ± 3.9	0.162	-30.7 ± 2.8	2.8 ± 0.1
TM	Trimyristin	182.8 ± 2.0	0.196	-29.8 ± 1.8	2.4 ± 0.1
TL	Trilaurin	150.7 ± 14.5	0.165	-29.3 ± 1.5	2.5 ± 0.1

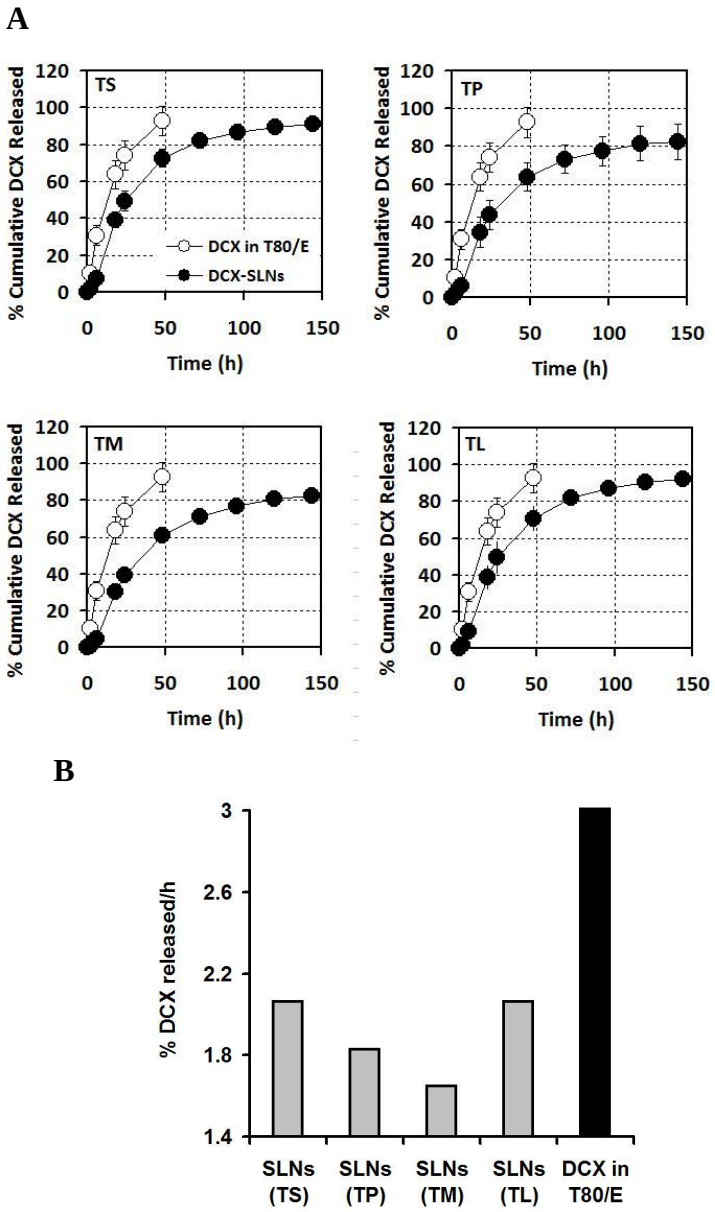
A
TS
TP
TM
TL
% Cumulative DCX Released
Time (h)
DCX in T80/E
DCX-SLNs
B
% DCX released/h
SLNs (TS)
SLNs (TP)
SLNs (TM)
SLNs (TL)
DCX in T80/E

Figure: 2.1

Figure 2.1: (**A**) **The release of DCX from DCX-SLNs (closed circles) prepared using tristearin (TS), tripalmitin (TP), trimyristin (TM), or trilaurin (TL)**. As a control, the release of DCX from DCX in T80/E (open circles) was also included. Each point represents mean ± S.D. from three independent measurements. (**B)** A comparison of the percent of DCX released per hour from DCX-SLNs prepared using different triglycerides. The release rates were calculated with data in the initial 24 h period. Each point represents mean (n = 3).

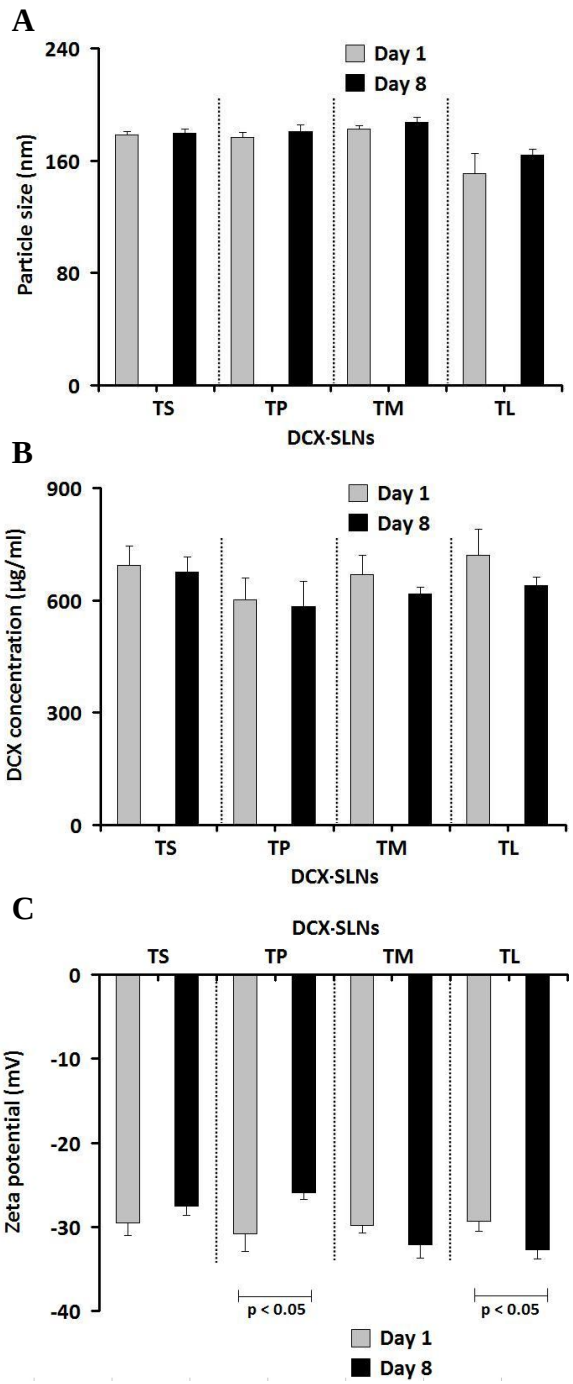
A
240
160
80
0
Particle size (nm)
Day 1
Day 8
TS
TP
TM
TL
DCX-SLNs
B
900
600
300
0
DCX concentration (µg/ml)
Day 1
Day 8
TS
TP
TM
TL
DCX-SLNs
C
DCX-SLNs
TS
TP
TM
TL
0
-10
-20
-30
-40
Zeta potential (mV)
p < 0.05
p < 0.05
Day 1
Day 8

Figure: 2.2

Figure 2.2: Stability of the DCX-SLNs formulations prepared using different triglycerides. The particle sizes (**A**), DCX contents (**B**), and zeta potentials (**C**) of DCX-SLNs prepared with different triglycerides shortly after preparation or after 8 days of storage at 4°C. Data shown are mean ± S.D. (n = 3).

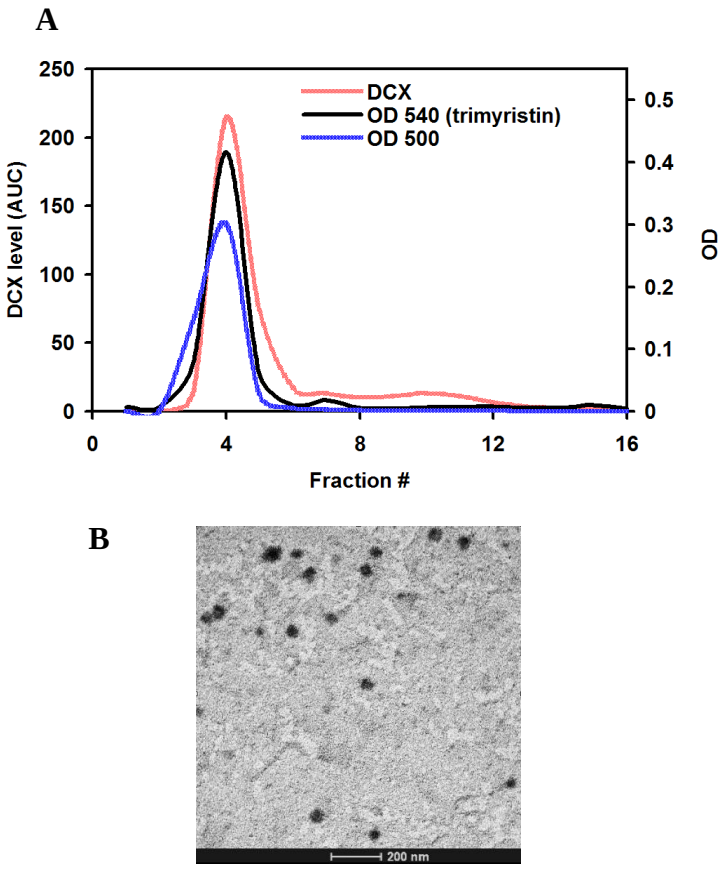
A
DCX
OD 540 (trimyristin)
OD 500
DCX level (AUC)
OD
Fraction #
250
200
150
100
50
0
0.5
0.4
0.3
0.2
0.1
0
0
4
8
12
16
B
200 nm

Figure: 2.3

Figure 2.3: **Gel permeations chromatogram of the prepared DCX-SLNs (prepared using trimyristin) and a representative TEM image of DCX-SLNs.** (**A**) A representative GPC profile of DCX-SLNs prepared with trimyristin. Collected fractions were divided into three portions; one was analyzed for DCX content (red), one was used to measure turbidity (OD 500 nm) (blue), and the other one was used to measure trimyristin concentrations, and the visible absorbance of the formed colored component was measured (OD 540) (black). This experiment was repeated three times with similar results. (**B**) A representative TEM image of DCX-SLNs prepared with trimyristin (bar = 200nm).

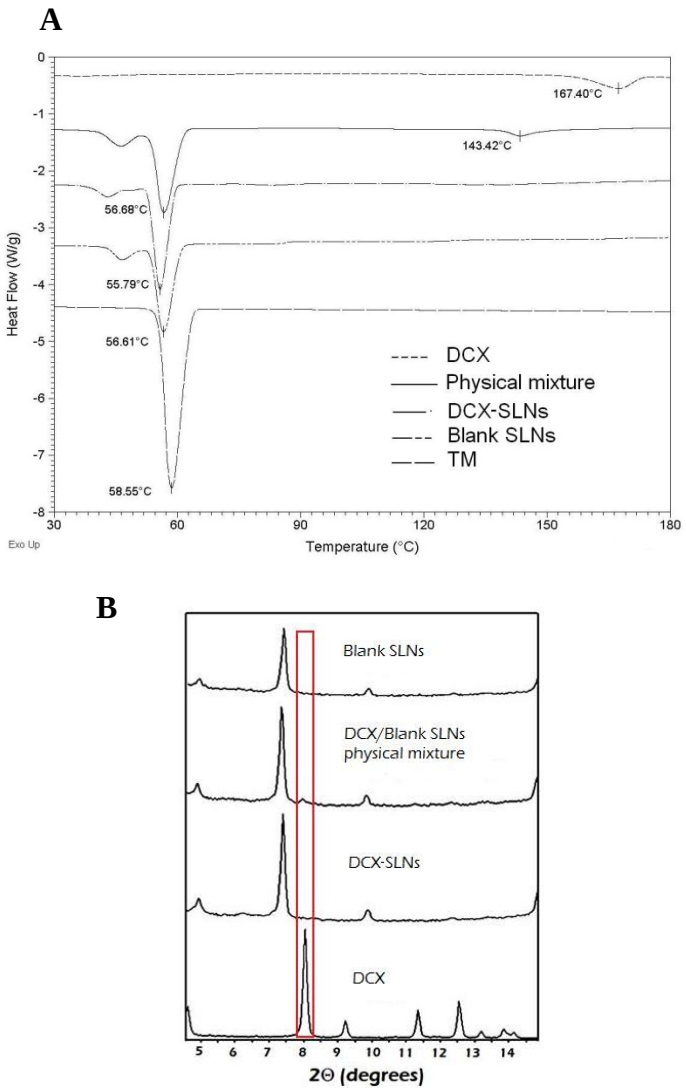
A
Heat Flow (W/g)
Exo Up
Temperature (°C)
167.40°C
143.42°C
56.68°C
55.79°C
56.61°C
58.55°C
DCX
Physical mixture
DCX-SLNs
Blank SLNs
TM
B
Blank SLNs
DCX/Blank SLNs
physical mixture
DCX-SLNs
DCX
2Θ (degrees)

Figure: 2.4

Figure 2.4: **Physicochemical characterization of DCX-SLNs.** DSC thermograms (**A**) and X-ray diffractograms (**B**) of DCX-SLNs, DCX alone, trimyristin (TM) alone, blank SLNs, or the physical mixture of blank SLNs and DCX.

2.3.3 Cytotoxicity of the DCX-SLNs prepared with trimyristin as a triglyceride against tumor cells in culture

MTT assay revealed that both DCX-SLNs and DCX in T80/E inhibited the proliferation of tumor cells, including murine mammary gland cancer cells (M-Wnt), murine lung cancer cells (TC-1), and human breast adenocarcinoma cells (MDA-MB-231). However, the IC_{50} values of the DCX-SLNs were significantly lower than that of the DCX in T80/E in each of the three cell lines (Figure 2.5A). At the highest equivalent DCX concentrations tested (i.e., 0.01, 1, and 0.05 μM in M-Wnt, TC-1, and MDA-MB-231, respectively), both the blank SLNs and the T80/E vehicle control did not show any significant toxicity in all three cell lines (data not shown).

Caspase 3 activity was also measured in TC-1 cells treated with DCX-SLNs, DCX in T80/E, Blank SLNs, and T80/E at a DCX concentration of 0.01 μM. Caspase 3 activity in cells treated with the DCX-SLNs was significantly higher than in cells treated with DCX in T80/E ($p < 0.005$, Figure 2.5B). The total protein contents in the cell lysates in all four groups were not significantly different (data not shown).

2.3.4 The antitumor activity of the DCX-SLNs prepared with trimyristin as a triglyceride in a mouse model

The antitumor activity of DCX-SLNs was evaluated in TC-1 murine lung cancer tumor model pre-established in C57BL/6 mice. As shown in Figure 2.6A, both DCX-SLNs and DCX in T80/E significantly inhibited the growth of the TC-1 tumors in mice. However, the DCX-SLNs were significantly more effective than the DCX in T80/E

formulation, starting on day 15 (Figure 2.6A). The average body weights of mice that were injected with blank SLNs or 5% mannitol (as a vehicle control) increased slightly (~10%) during the 21 days after tumor cells implantation, while the average body weight of mice that were treated with DCX-SLNs or DCX in T80/E did not show any significant change (Figure 2.6B). Finally, the average weight of tumors in mice that were treated with the DCX-SLNs was also significantly lower than that in other groups at the end of the study (Figure 2.6C). Anti-CD31 staining (i.e., angiogenesis marker) showed that the extent of $CD31^+$ staining tended to be lower in tumors in mice that were treated with the DCX-SLNs, as compared to in other groups (Figure 2.6D).

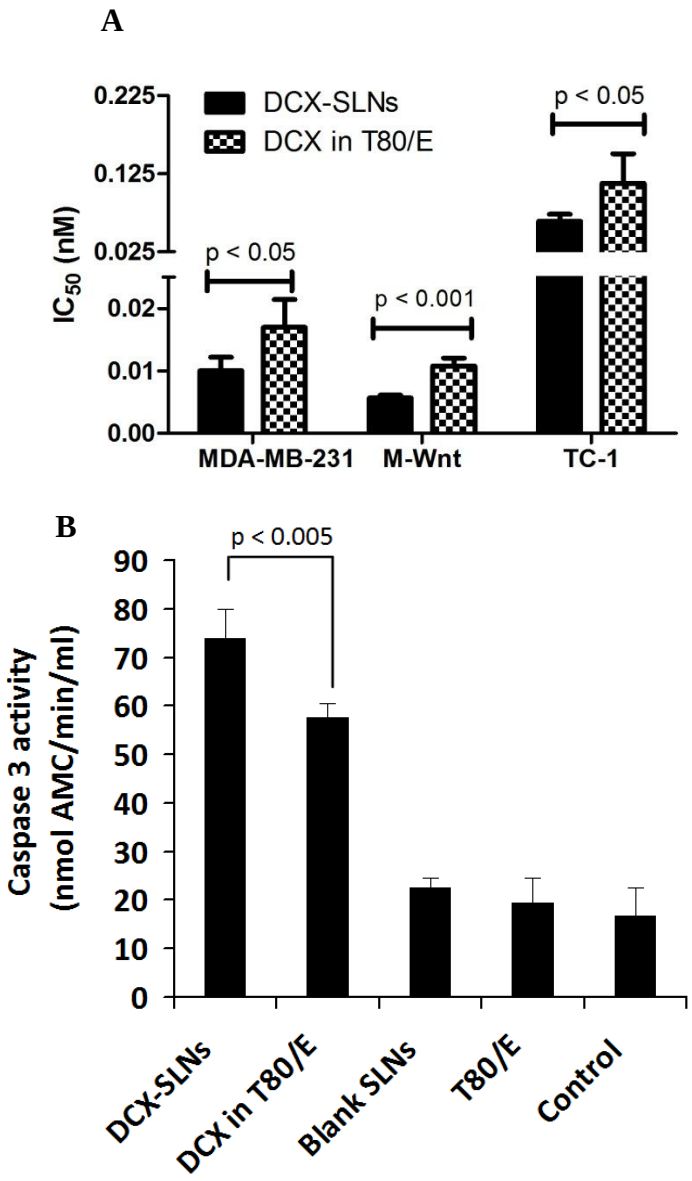
A
0.225
0.125
0.025
0.02
0.01
0.00
IC50 (nM)
DCX-SLNs
DCX in T80/E
p < 0.05
p < 0.001
p < 0.05
MDA-MB-231
M-Wnt
TC-1
B
p < 0.005
90
80
70
60
50
40
30
20
10
0
Caspase 3 activity
(nmol AMC/min/ml)
DCX-SLNs
DCX in T80/E
Blank SLNs
T80/E
Control

Figure: 2.5

Figure 2.5: Apoptotic and anti-proliferative activity of the DCX-SLNs. (A) The IC_{50} values of DCX-SLNs and DCX in T80/E in MDA-MB-231, M-Wnt, and TC-1 cells. Cells were incubated with the DCX formulations for 72 h. (**B**) Caspase 3 activity (in mmol AMC/min/ml) in TC-1 cells following 72 h of incubation with DCX-SLNs or DCX in T80/E (DCX, 0.01 μM). Controls include blank SLNs, T80/E vehicle, or medium alone. Data shown are mean ± S.D. (n = 4).

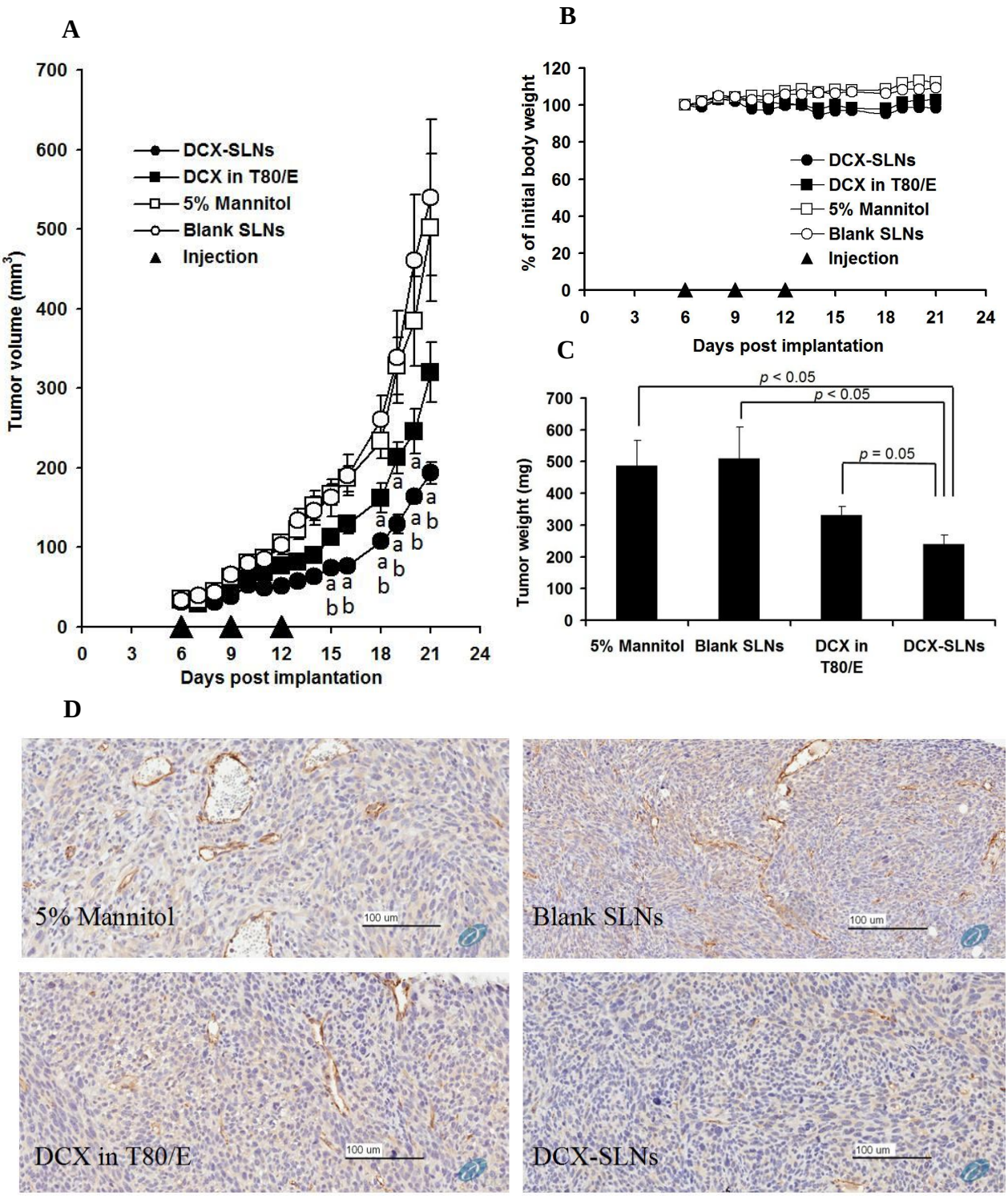
A
Tumor volume (mm3)
DCX-SLNs
DCX in T80/E
5% Mannitol
Blank SLNs
Injection
Days post implantation
B
% of initial body weight
DCX-SLNs
DCX in T80/E
5% Mannitol
Blank SLNs
Injection
Days post implantation
C
Tumor weight (mg)
p < 0.05
p < 0.05
p = 0.05
5% Mannitol
Blank SLNs
DCX in T80/E
DCX-SLNs
D
5% Mannitol
Blank SLNs
DCX in T80/E
DCX-SLNs
100 um

Figure: 2.6

Figure 2.6: Antitumor activity of DCX-SLNs in tumor-bearing mice. (**A**) The growth curves of TC-1 tumors in C57BL/6 mice ([a] $p < 0.05$, DCX-SLNs or DCX in T80/E vs. 5% mannitol, [b] $p < 0.05$, DCX-SLNs vs. DCX in T80/E). (**B**) The changes in the body weight of TC-1 tumor-bearing mice. (**C**) The weights of tumors at the end of the study. (**D**) Representative images of tumor tissues after anti-CD31 staining (Bar = 100 μm). Mice were i.v. injected with DCX-SLNs or DCX in T80/E at a DCX dose of 15 mg/kg via the tail vein on days 6, 9, and 12 after tumor implantation. Controls included mice that were injected with blank SLNs or 5% mannitol. Data shown in A-C are mean ± S.E.M. (n = 7).

2.3.5 Biodistribution study

Figure 2.7 shows the concentration of DCX in tumors and other organs in TC-1 tumor-bearing mice 2 and 12 h after the mice were injected intravenously with either DCX-SLNs (prepared with trimyristin) or DCX in T80/Ethanol. The concentration of DCX in tumors in mice that were injected with DCX-SLNs was about 50% higher than in mice that were injected with the DCX in T80/Ethanol formulation, 12 h after the injection ($p < 0.05$) (Figure 2.7A). However, the concentration of DCX in the liver, spleen, kidneys, heart, and lungs of mice injected with the DCX-SLNs were lower than in mice injected with the DCX in T80/E formulation (Figs. 7B-F). Finally, 2 h after intravenous injection, the concentration of DCX in the plasma in mice that were injected with the DCX-SLNs was about 5-times higher than in mice that were injected with the DCX in T80/E formulation (Figure 2.7G).

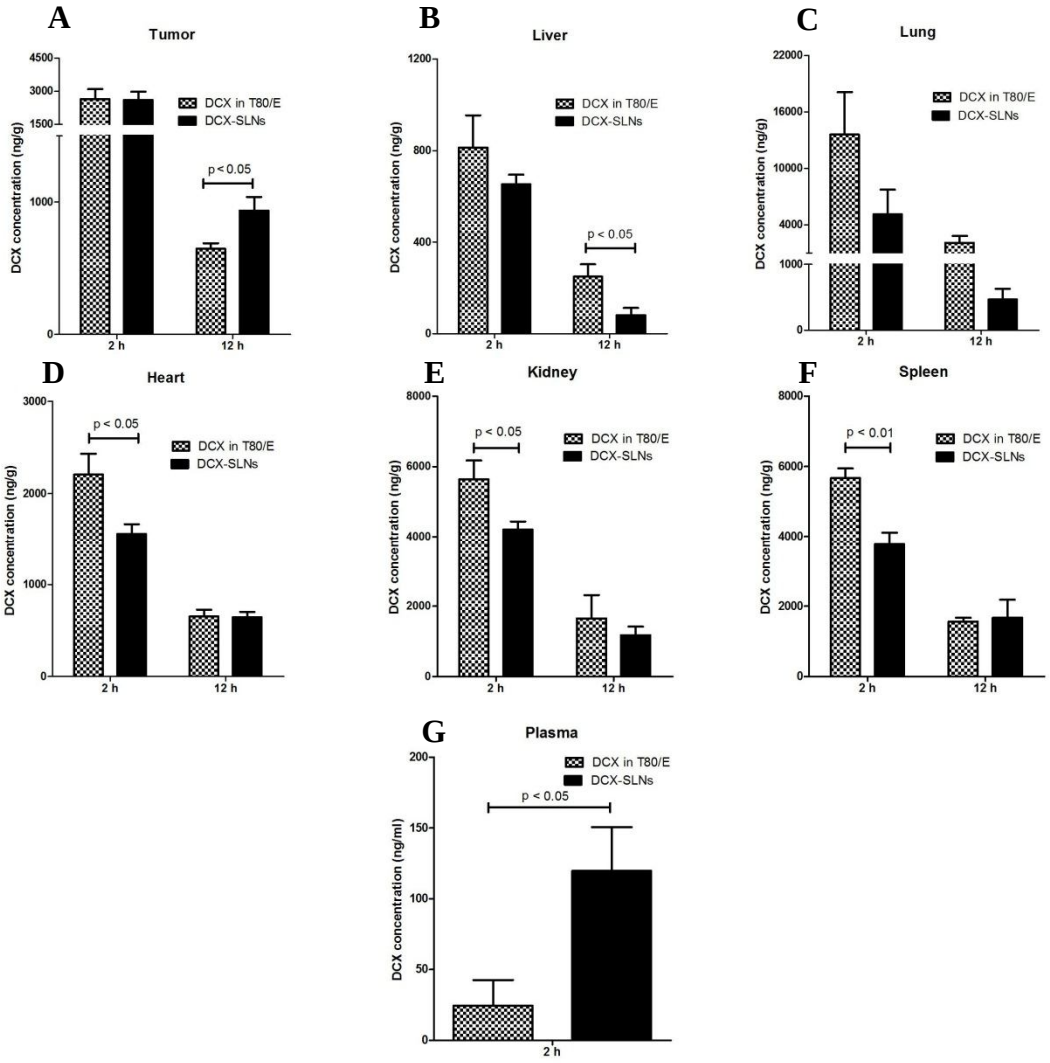
A
Tumor
DCX concentration (ng/g)
DCX in T80/E
DCX-SLNs
p < 0.05
2 h
12 h
B
Liver
C
Lung
D
Heart
E
Kidney
F
Spleen
p < 0.01
G
Plasma
DCX concentration (ng/ml)

Figure: 2.7

Figure 2.7: **Biodistribution profile of DCX-SLNs in the tumors and organs of mice**. The concentrations of DCX in tumor (**A**), liver (**B**), lungs (**C**), heart (**D**), kidneys (**E**), spleen (**F**), and plasma (**G**) of TC-1 tumor-bearing C57BL/6 mice 2 or 12 h after i.v. injection of either DCX-SLNs or DCX in T80/E. The dose of DCX was 16 mg/kg. Data shown are mean ± S.E.M. (n = 4-5).

2.4 Discussion

Since the discovery of taxanes in the mid-1980s, the fervent search for more efficacious and less toxic taxane formulations has led to the FDA approval of three market products, namely Taxol® (Bristol-Myers Squibb, Princeton, NJ, USA), Taxotere® (Sanofi-Aventis U.S. LLC, Bridgewater, NJ, USA), and Abraxane® (Celgene Corporation, Summit, NJ, USA). In addition, a polymeric PEGylated micelle formulation of paclitaxel (Genexol-PM) has been marketed in South Korea since 2007 [262-264], and others (e.g. BIND-014) are in the pipeline [264]. Taxotere® used to be the only FDA-approved DCX formulation on the U.S. market. Generic DCX products that are currently in the U.S. include formulations launched by Hospira, Sagent, Accord, which are all DCX in Tween80/ethanol solutions. Docefrez® is a lyophilized DCX powder to be reconstituted with 3.54% ethanol in Tween 80 before injection. DCX has low water solubility (~5 μg/ml) [265], and Tween 80 and ethanol are used in the current DCX formulations to solubilize DCX.

The main aim in the present study was to rationally design a Tween 80-free formulation of DCX that also improves the antitumor activity of DCX. Based on a study by Huynh *et al.*, where the authors reported that DCX solubility in low melting point triglycerides, such as tributyrin, tricaproin, and tricaprylin, is 10,000-20,000 times more than in water [259], we postulated that triglycerides-based SLN formulations may exhibit attractive drug-excipient interaction, facilitating incorporation of DCX in the nanoparticles. Four different medium- and long-chain saturated triglycerides that are solid at body temperature were employed in this study; namely, trilaurin (m.p. 46°C),

trimyristin (m.p. 57°C), tripalmitin, (m.p. 66°C), and tristearin (m.p. 69°C) with fatty acid-chain lengths of 12 (C12:0), 14 (C14:0), 16 (C16:0), and 18 (C18:0) carbon atoms, respectively. It was reported that triglycerides with melting points lower than room temperature form nano-droplets that are prone to coalescence during preparation or storage [252;253]. The use of high melting point triglycerides may significantly decrease the mobility of the drug molecules within the lipid core and thus reduce immature drug leakage [253;257].

Therefore, tricaprylin (C8:0, m.p. 9°C), tricaprin (C10:0, m.p. 31°C), and trolein (C18:1, m.p. 5°C) were excluded. The trimyristin-based SLN formulation was chosen from the four tested formulations because the rate at which the DCX was released from them was the slowest (Figure 2.1), and the SLNs were also more stable (Figure 2.2). In a mouse model with pre-established TC-1 mouse tumors, the DCX-SLNs were significantly more effective than DCX in T80/E in inhibiting the tumor growth (Figure 2.6), likely because the DCX-SLNs significantly increased the accumulation of DCX in tumor tissues (Figure 2.7A). Circulating nano-carriers usually take advantage of the leaky vasculature and/or poor lymphatic drainage in tumor tissues to accumulate in tumors [91;266]. Since DCX accumulation in tumor was only significantly higher at 12 h, but not at 2 h, following the administration of SLNs, as compared to the DCX in T80/E, it is likely that the enhanced retention of the DCX-SLNs in tumors due to poor lymphatic drainage was responsible for the improved accumulation [91;94]. Small molecules may also exhibit enhanced permeation to tumors as well due to the leaky neovasculature in the tumor tissues, however, they can easily diffuse out of tumors as well, while

macromolecules and nano-carriers are entrapped and consequently accumulate [83;87;89].

DCX not only induces apoptosis due to microtubule assembly stabilization, but also is antiangiogenic [238;267]. Inhibition of the formation of new blood vessels that provide rapidly growing tumors with increasing nutritional demand is expected to stunt the tumor growth [86;88;109]. Furthermore, the hastily-formed tumor-associated vasculature is characterized with various fenestration and imperfections, and almost lacking any intact lymphatic drainage [87;91;94;268]. Nanoparticles are known to take advantage of this leaky tumor vasculature to extravasate into the tumor microenvironment, where they can accumulate [266]. Several groups have reported lipid nanoparticle-based DCX formulations before [38;210;253;269-271]. The most widely used lipid excipients are soy lecithin, glycerides, or a mixture of the two. For example, Liu *et al*. formulated DCX into a nano-structured lipid carrier composed of soy lecithin, glyceryl monostearate, and fatty acids [271], but the DCX in nano-structured lipid carrier was only slightly more effective than a DCX in a T80/E formulation (Duopafei®) against B16 tumors in mice [271]. Xu *et al*. designed a trimyristin-based SLN formulation for DCX to treat hepatocellular carcinoma [38]. To improve their liver uptake, the SLNs were not PEGylated. Instead, their surface was galactosylated to target asialoglycoprotein receptors overexpressed on the surface of hepatoma cell lines [38].

We previously reported the formulation of DCX-loaded lecithin-based PEGylated SLNs [210]. The resultant SLNs showed an improved *in vitro* cytotoxic activity, in addition to improved tumor accumulation in a mouse model. However, the capacity of

this formulation in incorporating DCX was limited, which may be attributed to the limited affinity between DCX and the excipients [210]. In the present study, in order to rationally select the most suitable excipient, four DCX-SLN formulations were prepared using four different high melting point triglycerides.

As discussed previously, a successful formulation for taxane is the one that exhibits (a) long plasma circulation time, (b) long drug retention within the delivery carrier, which requires high drug-excipient affinity and slow release, (c) high tumor accumulation, and (d) favorable biodistribution profile, as less drug goes to healthy tissues [44]. Drug release behavior from the DCX-SLNs and short-term stability were the criteria for triglyceride selection in this study. In this regard, the absence of a burst release of DCX from the DCX-SLNs in the first 2 h and a subsequent slower release rate predict a limited drug leakage from the nanoparticles in the blood circulation before reaching tumors [272]. The release of DCX from the tristearin-based and trilaurin-based DCX-SLNs was relatively faster (Figure 2.1), and the tripalmitin- and trilaurin-based DCX-SLNs showed instability, as the zeta potential changed significantly following a short-term storage (Figure 2.2). Change in zeta potential has been used as an indicator of nanoparticle instability [273;274]. Several reports indicated that trilaurin does not exist in the solid state within the SLNs, but rather as a ‘supercooled-liquid state’ that resembles O/W emulsions, even at 4°C, which was not the case with triglycerides having higher melting points [273;275;276]. The relatively faster release of DCX from the trilaurin-based SLNs may also arise as a result of the same phenomenon. As to the SLNs prepared with tripalmitin, the ‘super-cooled liquid state’ phenomenon was not reported, therefore,

the reasons to which this sign of instability may be attributed need to be investigated. On the other hand, the absence of a burst release of DCX from the DCX-SLNs prepared with trimyristin may infer a strong DCX-trimyristin interaction. It was reported that the solubility of DCX in tributyrin (4 C-chain) is about 108 mg/ml, and it gets lower with higher chain length, reaching about 56 mg/ml with tricaprylin (8 C-chain) [259]. Based on this, and since DSC and XRD data (Figure 2.4) implied that there is a strong interaction between DCX and the excipients, it is speculated that DCX exists in the SLNs either in a non-crystalline state and/or a dissolved state, within the lipid matrix. Existence of DCX in the amorphous state within lipid-based matrices was also reported previously [40]. The disappearance of the characteristic DCX-related peaks in DSC and XRD was previously shown to be related to the loss of DCX crystallinity [40;277]. In fact, we also found that the characteristic melting peak of DCX at 167°C completely disappeared upon analyzing the thermal behavior of DCX-trimyristin mixtures at DCX to trimyristin ratios of 1:5, 1:2, and 1:1 using DSC (data not shown), suggesting the prevalence of a strong interaction between the DCX and trimyristin. The relatively slower release of DCX from trimyristin-based DCX-SLNs may also be attributed to the strong DCX-lipid interaction as well.

Finally, potential toxicity issues were also considered during excipient selection. Long chain triglycerides in soybean oil and egg yolk phospholipids are commonly used in intravenous fat emulsions as components of parenteral nutrition for patients who are not able to receive nutrition via oral diets (e.g., Intralipid®, B Braun Medical Inc., Bethlehem, PA). Triglycerides are metabolized in the blood by lipases into corresponding

fatty acids, which are cleared from the blood within about 30 min [278]. Phosphatidylcholine and PEGylated phosphoethanolamine are used in products that are approved for intravenous infusion in humans (e.g., Doxil®). Therefore, we expect that our new DCX-SLN formulations will likely have a favorable safety profile. In fact, the body weights of the tumor-bearing mice that were treated with the DCX-SLNs did not significantly change by the end of the efficacy study (Figure 2.6B). In addition, the concentrations of DCX in vital organs such as liver, spleen, kidneys, lungs, and heart of mice that were injected with the DCX-SLNs were significantly lower than in mice that were injected with the DCX in T80/E formulation (Figure. 7), indicating that our DCX-SLNs may be less damaging to those vital organs than Taxotere®.

2.5 Conclusion

In the present study, by taking advantage of the high solubility of DCX in triglycerides, we successfully prepared several DCX-incorporated SLNs using various medium- and long-chain triglycerides. The DCX-SLN composition prepared with trimyristin was selected for further evaluation because the resultant DCX-SLNs were stable in a short-term stability study, and the rate at which the DCX was released from them was the slowest. The DCX-SLNs showed a stronger antitumor activity than DCX solubilized in a Tween 80/ethanol mixture in cell culture and, more importantly, in a mouse model with pre-established tumors, likely because the DCX-SLNs significantly increased the accumulation of the DCX in tumor tissues. The decreased accumulation of DCX in vital organs after i.v. injection of DCX-SLNs, relative to after injection of DCX solubilized in a Tween80/ethanol mixture, suggests that the DCX-SLNs may have a favorable safety profile.

Chapter 3

Synthesis, characterizations, and *in vitro* and *in vivo* evaluations of 4-(*N*)-docosahexaenoyl 2´, 2´-difluorodeoxycytidine with potent and broad spectrum antitumor activity

3.1 Introduction

Docosahexaenoic acid (DHA, omega-3, 22:6, n-3) is a polyunsaturated fatty acids (PUFA) that has been extensively investigated for its potential antitumor activity, either as a single agent or in combination with other cancer chemotherapeutic agents [279-283]. It was shown that omega-3 PUFAs induce apoptosis in various cancer cells [284;285], inhibit cancer cell invasiveness [286], and inhibit metastasis and angiogenesis in tumor tissues [287-289]. The mechanism underlying the antitumor efficacy of omega-3 PUFAs remains unclear, but it is thought to be related to its potent anti-oxidant activity [284]. In order to better take advantage of the antitumor activity of DHA, it was previously conjugated with some commonly used anti-cancer chemotherapeutic agents, such as paclitaxel, doxorubicin, and camptothecin [290-292]. For example, Bradley et al. showed that conjugation of DHA to paclitaxel significantly modified the pharmacokinetics and biodistribution of paclitaxel, prompting the testing of the DHA-paclitaxel conjugate (i.e., Taxoprexin) in clinical trials [293;294], although the DHA–paclitaxel conjugate was not more cytotoxic than paclitaxel alone against many tumor cells in culture [292;295;296].

Gemcitabine HCl (2`, 2`-difluorodeoxycytidine HCl, dFdC) is a fluorinated deoxycytidine analogue. It is the standard treatment of locally advanced and metastatic

pancreatic cancer [297;298] and is also used in combination therapy to treat various other solid tumors including breast, bladder, lung, and ovarian cancers [297;299;300]. In pancreatic cancer, the drug is administered at a 1000 mg/m^2 intravenous infusion over 30 min once/week for 7 weeks followed by a one week's rest, then once weekly for up to 3 weeks in a 28 days' cycle, and while this dosage regimen is changed in case of non small cell lung cancer, ovarian cancer, and breast cancer, the recommended short infusion time (< 70 min) keeps the infusion time-dependant plasma half life relatively short [301-303]. Extensive deamination at the 4-amino site, which takes place both intracellularly and extracellularly by the action cytidine deaminase, is responsible for the loss of about 90% of the drug, and the deaminated metabolite difluorodeoxyuridine (dFdU) is almost inactive [39;179;193;297;304]. More than 99% of administered dFdC is excreted in the urine, with unchanged dFdC comprising only 5%, and the rest is the long-circulating dFdU, which has a terminal phase half life of about 22 h [297;305]. Over the years, there have been reports showing that chemical modifications of this fluorinated deoxycytidine analogue may potentially improve its efficacy and/or safety profile. For example, it was shown that conjugation of a fatty acid, such as stearic acid or lauric acid, to dFdC at the 4-NH_2 group decreases the sensitivity of the latter to deaminase, modifies its pharmacokinetics, and in some cases, improves its *in vivo* antitumor activity [39;114;208;219;301;302;306-315]

In the present study, we report the synthesis, characterization, and *in vitro* and *in vivo* evaluations of 4-(*N*)-docosahexaenoyl 2´, 2´-difluorodeoxycytidine (DHA-dFdC) conjugate. DHA-dFdC showed broad spectrum and potent antitumor activity in various

human cancer cell lines. Because DHA-dFdC showed an unexpectedly longer residence time in mouse pancreas, compared to dFdC, and since pancreatic cancer is one of the most aggressive, and in most cases fatal, types of cancer, with a mortality rate almost equal to incidence rate [316;317], the antitumor activity of the DHA-dFdC was primarily evaluated in mouse models of pancreatic cancer.

3.2 Materials and Methods

3.2.1 Materials

Gemcitabine HCl (dFdC) was from Biotang, Inc. (Lexington, MA). Cis-4,7,10,13,16,19-docosahexaenoic acid (DHA) and trifluoroacetic acid (TFA) were from Acros Organics (Morris Plains, NJ). Di-tert-butyl-dicarbonate, 1-(3-dimethylaminopropyl)-3-ethylcarbodiimide hydrochloride (EDCl), 3-(4,5-dimethylthiazol-2-yl)-2,5-diphenyltetrazolium bromide (MTT), HPLC grade methanol, and Tween 80 were from Sigma-Aldrich (St Louis, MO). Hydroxy-7-azabenzotriazole (HOAt) was from CreoSalus, Inc. (Louisville, KY). Isopropyl myristate (IPM) was from TCI America (Montgomeryville, PA). Anhydrous sodium sulfate, ammonium chloride, mono- and di-basic sodium phosphates, ethyl acetate, HPLC-grade acetonitrile, dichloromethane (DCM), acetone, hexane, and octanol were from Thermo Fisher (Waltham, MA). BD Matrigel^{TM} Basement Membrane Matrix was from BD Biosciences (San Jose, CA). D-Luciferin K^+ salt bioluminescent substrate was from Perkin Elmer (Waltham, MA). Guava Nexin reagent for flow cytometry was from EMD Millipore (Billerica, MA). Lactate dehydrogenase (LDH) cytotoxicity detection kit was from Takara (Clonetech Laboratories, Mountain View, CA). Dulbecco's modified Eagle medium (DMEM), Roswell Park Memorial Institute (RPMI 1640) medium, fetal bovine serum (FBS), penicillin, streptomycin, horse serum, and Dulbecco's phosphate buffer saline (DPBS) were all from Invitrogen-Life Technologies (Carlsbad, CA). All other

chemicals, reagents, and solvents were of analytical grade and used as received without further purification.

3.2.2 Cell lines

Panc-02 (mouse pancreatic cell line), BxPC-3 (human pancreatic cancer cell line), MIA PaCa-2 (human pancreatic cancer cell line), and TC-1 (mouse lung cancer cell line) were from the American Type Culture Collection (ATCC, Manassas, VA). Panc-1-Luc human pancreatic cell line was generously provided by Dr. Dawn E. Quelle at the University of Iowa [318]. TC-1 and Panc-02 cells were grown in RPMI 1640 medium. BxPC-3, MIA PaCa-2, and Panc-1-Luc cells were grown in DMEM. All media were supplemented with 10% FBS, 100 U/ml of penicillin, and 100 g/ml of streptomycin, and the DMEM for MIA PaCa-2 cells was supplemented additionally with 2.5% horse serum.

3.2.3 Synthesis of 4-N-docosahexaenoyl 2´, 2´-difluorodeoxycytidine (DHA-dFdC) (3)

DHA-dFdC was synthesized following a previously reported conjugation scheme with slight modifications [39;193;208] (**Scheme 3.1**). dFdC **(1)** (200 mg, 0.67 mmol) in 13.3 ml of 1 N potassium hydroxide was cooled to 4° C. To this solution, di-tert-butyl dicarbonate (Boc_2O, 1.483 g, 6.8 mmol) in about 13.3 ml of anhydrous dioxane was added over 10 min under argon atmosphere as previously reported [319]. The reaction mixture was stirred at room temperature (~22° C) for 1 h and extracted with ethyl acetate (EtOAc). The organic layer was washed with brine, dried over anhydrous

sodium sulfate (Na_2SO_4) and filtered. Solvent was removed under reduced pressure. The residue was added to Boc_2O (1.483 g, 6.8 mmol) in 13.3 ml of anhydrous dioxane and 13.3 ml of 1 M KOH at room temperature. The reaction was monitored by thin-layer chromatography (TLC). After 1 h, the reaction mixture was extracted to EtOAc. The organic layer was washed with brine, dried over anhydrous Na_2SO_4, and filtered. Solvent was then removed, and the crude product was purified by column chromatography (DCM to acetone, 1:1, v/v). The desired product fractions were pooled and dried to yield 219 mg (71 %) of 3`,5`-O-bis(tert-butoxycarbonyl) dFdC **(2).** ^{1}H NMR (500 MHz, acetone-d^6) δ 7.60 (1 H, d, J = 7.6 Hz, 6-CH), 6.34 (1 H, brs, 1`-CH), 5.97 (1 H, d, J = 7.6 Hz, 5-CH), 5.29 (1 H, brs, 3`-CH), 4.53-4.39 (3 H, m, 4`-CH, 5`A-CH, 5`B-CH), 2.82 (2 H, s, $NH_2$) 1.50, 1.47 (18 H, two s, $(CH_3)_3C$). A solution of 3`,5`-O-bis(tert-butoxycarbonyl) dFdC (150 mg, 324 µmol), DHA (123 mg, 373.9 µmol) and HOAt (75 mg, 551.1 µmol) in anhydrous DCM was pre-cooled to 4^{o}C, and EDCI (93.75 mg, 604.1 µmol) was added. The mixture was de-gassed by vacuum sonication and then stirred at room temperature under argon for about 40 h. Water (5 ml) was added to the reaction mixture and extracted three times with a mixture of EtOAc and hexane (2:1, v/v). The combined organic phase was washed with saturated ammonium chloride (NH_4Cl) and brine and then dried over anhydrous Na_2SO_4. The solvent was evaporated, and the residue was purified by column chromatography (EtOAc to Hexane, 3:7, v/v). The conjugated amide was isolated and quantified (~165 mg). ^{1}H NMR was as follows: (300 MHz, acetone-d^6) δ 9.18 (1 H, s, NHCO), 7.83 (1 H, d, J = 7.8 Hz, 6-CH), 7.49 (1 H, d, J = 7.8 Hz, 5-CH), 6.47-6.42 (1 H, m, 1′-CH), 5.42-5.30 (12 H, m, CH_2), 5.30-5.05 (1 H, m, 3′-CH), 4.50–4.34 (3 H, m, 4′-

CH and 5′-CH), 2.90-2.79 (10 H, m, CH_2), 2.60-2.40 (4 H, m, CH_2), 2.07 (2 H, p, J = 7.5 Hz, CH_2), 1.53-1.46 (18H, m, $(CH_3)_3C$), 0.97 (3 H, t, J = 7.4 Hz, terminal CH_3). To a stirred solution of the conjugated amide (37 mg, 47.8 nmol) in 3 ml of DCM, about 0.2 ml of TFA was added. This solution was stirred at room temperature for 4 h, and excess TFA was removed under reduced pressure. The concentrated sample was co-distilled with DCM for 3 times. The crude sample was chromatographed on silica gel (DCM to ethanol, 94:6, v/v) [193;301]. The desired fractions were pooled, and the solvent was evaporated to yield 4-(*N*)-DHA-dFdC (DHA-dFdC, **3**, ~80 mg, ~36% of original combined weights of dFdC and DHA). ^{1}H NMR (300 MHz, THF-d^4) was as follows: δ 10.13 (1H, s, NHCO), 8.17 (1H, d, J = 7.5 Hz, 6-CH), 7.37 (1H, d, J = 7.5 Hz, 5-CH), 6.25 (1H, t, J = 7.4 Hz, 1′-CH), 5.51–5.27 (12H, m, CH), 4.40-4.20 (1H, m, 3′-CH), 3.95–3.70 (3H, m, 4′-CH and 5′-CH), 2.95-2.82 (10H, m, CH_2), 2.50-2.41 (4H, m, CH_2), 2.08 (2H, p, J = 7.2 Hz, CH_2), 0.96 (3H, t, J = 7.7 Hz, terminal CH_3) (see Figure 3.1A for ^{1}H NMR spectrum). ESI-HRMS $[M+Na]^+$ m/z calculated for $C_{31}H_{41}F_2N_3NaO_5$ is: 596.29065, found: 596.29068.

The purity of the synthesized compound was confirmed by LC/MS following gradient elution (Figure 3.1B and C). The LC/MS system used was an Agilent Technologies 6530 Accurate Mass Quadruple TOF LC/MS using a RP C18 column (Agilent Zorbax, 50 x 2.1 mm, 5 µm) at 40ºC. The mobile phase consisted of solvent A (water with 0.1% formic acid) and solvent B (acetonitrile with 0.1 % formic acid). Mobile phase composition was changed from 95% solvent A to 100% solvent B over 5 min, ran for 2 more minutes, and finally changed back to 95% solvent A over 4 more

minutes. The flow rate was 0.7 ml/min. The target compound was detected at 4.85 min, and the compound was observed as $[M+H]^+$ m/z at 574.3, $[M+Na]^+$ m/z at 596.3, $[2M+H]^+$ m/z at 1147.6, and $[2M+Na]^+$ m/z at 1169.6 (Figure 3.1C).

4-(*N*)-arachidonyl dFdC (ARA-dFdC) was synthesized similarly, except that the DHA was replaced with arachidonic acid (ARA), an omega-6 polyunsaturated fatty acid (Scheme 3.1). The structure of the resultant ARA-dFdC was confirmed using ^{1}H NMR and Mass Spectroscopy.

3.2.4 Determination of the solubility and partition coefficient of DHA-dFdC

The aqueous solubility of DHA-dFdC was determined following an indirect method according to Beall *et al*. with minimal modifications [320]. Briefly, excess amount of DHA-dFdC was added to 100 µl of IPM in a crimp-sealed amber glass vials under nitrogen and was stirred vigorously at room temperature for 24 h, protected from light. After the stirring was stopped, the mixture was left to stand for an additional 24 h for equilibration. The content of the vial was centrifuged (14,000 rpm, 10 min) and the supernatant was transferred into a different tube. Aliquots of the saturated IPM solution were used to measure the DHA-dFdC concentration before partitioning (A_1) using HPLC (after proper dilution with methanol). The HPLC method will be discussed in details later. Then, water was added to the IPM saturated solution in a volume ratio of 10:1. The two phases were mixed by vortexing for 5 min, left to stand for 15 min, and then centrifuged (14,000 rpm, 15 min) to collect the IPM layer. DHA-dFdC concentration in

the IPM layer (A_2) was again measured using HPLC after partitioning. The following equation was used to calculate the partition coefficient ($K_{IPM/water}$) [320]:

$$K_{IPM/water} = [A_1 / (A_1 - A_2)] \times [V_{water} / V_{IPM}] \quad \text{(equation 3)}$$

Where V_{water} is the volume of the water phase and V_{IPM} is the volume of IPM, and the value of V_{water} / V_{IPM} was 10.

The aqueous solubility (S_w) of DHA-dFdC was determined using the following equation [320]:

$$S_w = S_{IPM} / K_{IPM/water} \quad \text{(equation 4)}$$

Where S_{IPM} is the solubility of DHA-dFdC in IPM, and DHA-dFdC was found to be stable in IPM under test conditions for at least 48 h.

The octanol-water partition coefficient of DHA-dFdC was determined using a previously reported method with minor modifications [321]. Briefly, octanol and PBS (7.4, 0.01 M) were mutually saturated for 24 h. DHA-dFdC was dissolved in octanol (0.4 mg/ml, PBS-saturated) and 10 µl of the solution were withdrawn and diluted with methanol to measure DHA-dFdC concentration using HPLC (C_1). PBS was added to octanol at a volume ratio (V_{PBS} / V_{oct}) of 20:1 into a sealed vial under nitrogen, and the mixture was agitated vigorously at room temperature using a horizontal orbital shaker at

250 rpm (Max Q 2000, Thermo Scientific, Waltham, MA) while protected from light. After 5 h, the mixture was centrifuged (14,000 rpm, 15 min) and the concentration of DHA-dFdC in the octanol layer was determined using HPLC (C_2). Partition coefficient ($K_{oct/water}$) was calculated using the following equation:

$$K_{oct/water} = [C_1 / (C_1 - C_2)] \times [V_{PBS} / V_{oct}] \quad \text{(equation 5)}$$

DHA-dFdC was found to be stable in octanol under the test conditions for at least 18 h.

3.2.5 Chemical stability of DHA-dFdC in an aqueous solution

DHA-dFdC is freely soluble in ethanol and in Tween 80. It was solubilized into a formulation that contains Tween 80, ethanol, and water at a volume ratio of 1:0.52:8.48 to evaluate its *in vivo* activity. The stability of DHA-dFdC in this formulation was evaluated in crimp-sealed amber glass vials under nitrogen atmosphere. Briefly, 150 µl of the DHA-dFdC aqueous solution at a concentration of about 7 mg/ml were added to the amber glass vials under nitrogen atmosphere, and the vials were crimp-sealed with aluminum seals over rubber lids. At predetermined time intervals, 10 µl of the solution were diluted with 90 µl of methanol and mixed, and the concentration was measured using HPLC. Stability tests were carried out at room temperature (~22^{o}C) or 4^{o}C in triplicates. Vitamin E was added in the formulation to a final concentration of 0.01% or 0.04 % (v/v) to evaluate the effect of vitamin E on the chemical stability of DHA-dFdC.

To study the effect of temperature on the chemical stability of DHA-dFdC, the DHA-dFdC formulation in crimp-sealed vials under nitrogen was stored in room temperature, 37ºC, or 60ºC, protected from light. Sampling and analyses were carried out at pre-determined time points as described above. The first order degradation reaction equation was used to calculate the values of the reaction rate (*k*) at different temperatures. Arrhenius plot was constructed by plotting the log *k* values vs. 1/T to calculate the activation energy (E_a, in kcal/mol).

3.2.6 Physicochemical characterizations of DHA-dFdC

The UV-Vis absorbance of DHA-dFdC, DHA, dFdC, and the physical mixture of dFdC and DHA, all dissolved in methanol, were evaluated using a BioTek Synery HT Multi-Mode Microplate Reader (Winooski, VT) using the scanning mode. Modulated differential scanning calorimetry (DSC) was used to evaluate the thermal properties of DHA-dFdC. Samples (2-4 mg) were placed in sealed pans, and the DSC analysis was carried out using DSC Q200 (TA instruments, New Castle, DE) at a ramp rate of 5ºC/min under nitrogen flow. X-ray diffraction (XRD) analyses of DHA-dFdC, dFdC, DHA, and the physical mixture of dFdC and DHA (1:1, m/m) was carried out in the X-ray facility in the Department of Chemistry at the University of Texas at Austin using a Rigaku Spider single crystal X-ray diffractometer (Rigaku, Tokyo, Japan).

3.2.7 Evaluation of the anti-proliferative, cytotoxic, and pro-apoptotic activity of DHA-dFdC in tumor cells in culture

The anti-proliferative activity and cytotoxicity DHA-dFdC were tested using the NCI-60 DTP Human Tumor Cell Line Screen service (http://dtp.nci.nih.gov/branches/btb/ivclsp.html) using one-concentration and then five-concentrations. The NCI-60 cell lines do not include any pancreatic cancer cell lines. Therefore, DHA-dFdC antitumor activity was also evaluated in mouse (Panc-02) and human (Panc-1-Luc, MIA PaCa-2, and BxPC-3) pancreatic cell lines. TC-1 is a mouse lung cancer cell line that grows aggressively in mouse model [39], and thus the cytotoxicity of DHA-dFdC was also evaluated in TC-1 cells. For TC-1, Panc-02, BxPC-3 and Panc-1-Luc cells, cells (1,500/well for Panc-02, BxPC-3, and Panc-1-Luc, and 3,000/well for TC-1) were seeded in 96-well plates and incubated at 37º C and 5% CO_2 overnight. The cells were then treated with various concentrations of DHA-dFdC, dFdC, DHA, or physical mixture of dFdC and DHA (1:1 molar ratio, DHA + dFdC) for 24 h for Panc-1-Luc and TC-1, 48 h for Panc-02, and 72 h for BxPC-3. Cell survival was determined using an MTT assay as previously described [322]. dFdC was dissolved in cell culture media, whereas DHA-dFdC, DHA, and DHA in the mixture were dissolved in dimethylsulfoxide (DMSO). In a separate experiment, Panc-02 cells were also treated for 4 h with higher concentrations of DHA-dFdC (i.e., 10-100 μM) or molar equivalent concentrations of dFdC, DHA, or dFdC + DHA 1:1 m/m mixture and cytotoxicity was measured using MTT assay. The cytotoxic activity of DHA-dFdC in Panc-02 cells was also evaluated using an LDH assay kit (Takara Clonetech, Mountain view, CA). Panc-02 cells (1500 cells/well) were seeded in 96-well plates and incubated at 37ºC and 5% CO_2 for 24 h, followed by treatment with DHA-dFdC or dFdC as mentioned above for 48 h.

LDH activity in the cell culture medium was determined following the manufacturer's instruction. Finally, the anti-proliferative activity of the ARA-dFdC was also evaluated in MIA-PaCa-2 and BxPC-3 cells using MTT assay (1000 cells/well and then treated with various concentrations of ARA-dFdC for 72 h). The values of IC_{50} were calculated using either GraphPad Prism (GraphPad software, Inc., La Jolla, CA) or Microsoft Excel.

Apoptosis analysis was carried out as previously reported [209], Briefly, 100,000 Panc-02 cells were incubated in 24-well plates for 24 h at 37ºC and 5% CO_2 and then co-incubated with various concentrations of DHA-dFdC for 48 h. The cells were then harvested and stained with 0.1 ml of Guava Nexin reagent (Millipore Corporation, Billerica, MA) for 20 min at room temperature, protected from light. The stained cells were analyzed using a Millipore Guava easyCyte 8HT Flow Cytometry System. Control cells were left untreated.

3.2.8 Cellular uptake of DHA-dFdC

The uptake of DHA-dFdC by Panc-02 cells was evaluated. Briefly, 250,000 cells were seeded in 12-well plates and incubated overnight, followed by the addition of DHA-dFdC (or dFdC as a control) to a final concentration of 10 µM. Four hours later, the medium was removed, and cells were lysed using a 500 µl of 1:1 mixture of 2% sodium dodecyl sulfate (SDS) and 1% Triton X for 15 min at room temperature. The cell lysate was centrifuged (14,000 rpm, 10 min), supernatant collected, and 25 µl of which was used for protein assay using Pierce BCA protein assay kit (Life technologies, Carlsbad, CA). For cells that were incubated with dFdC, prior to the centrifugation of the cell

lysate, tetrahydrouridine (THU, 40 μg) were added into the cell lysate to inhibit de-amination, and deoxyuridine (dU, 0.4 μg) was added as an internal standard. DHA-dFdC was extracted from the cell lysate using ethyl acetate, which was evaporated under nitrogen, and the residue was re-dissolved in 100 μl of methanol and analyzed by HPLC. To extract dFdC, the cell lysate was mixed with acetonitrile for protein precipitation, followed by centrifugation and collection of the supernatant, which was evaporated under air stream at 45ºC. The residue was re-dissolved in 200 μl of water and analyzed using HPLC. Standard curves of DHA-dFdC and dFdC in cell lysates were constructed.

3.2.9 Pharmacokinetics and biodistribution of DHA-dFdC

Animal protocols were approved by the Institutional Animal Care and Use Committee at the University of Texas at Austin. Healthy female C57BL/6 mice (6-8 weeks, Charles River Laboratories, Wilmington, MA) were injected intravenously (i.v.) with DHA-dFdC solution in Tween 80/ethanol/water (with 5% mannitol) at a dose of 75 mg/kg. At various time points (5, 15, 30, 60, 120, and 180 min), 3 mice were euthanized at each time point to collect blood by cardiac puncture. DHA-dFdC was extracted from plasma using ethyl acetate and analyzed using HPLC. Data were analyzed using the Pharsight WinNonlin software (Sunnyvale, CA).

Biodistribution study was carried out in healthy female BALB/c mice (14-16 weeks old, Charles River). DHA-dFdC was i.v. injected at a dose of 75 mg/kg, and organs were collected after 1 h and weighed. In addition, the pancreatic content of DHA-dFdC was measured in the pancreas of female BALB/c mice (14-16 weeks, Charles

River) after i.v. injection (75 mg/kg), followed by euthanization of mice and collection of pancreas at predetermined time points (5, 25, 60, 90, 330, and 720 min). DHA-dFdC was extracted by ethyl acetate and analyzed by HPLC. As a control, the content of dFdC in mouse pancreas at various time points after i.v. injection of dFdC (75 mg/kg in 5% mannitol solution) was determined. Before extraction of dFdC, THU (4 μg) was added as deoxycytidine deaminase inhibitor, and dU (40 μg) was added as an internal standard. dFdC concentration was determined using HPLC.

Biodistribution of DHA-dFdC was also confirmed in C57BL/6 mice with pre-established subcutaneous TC-1 tumors. When tumor diameters reached 7-8 mm, mice were injected via the tail vein with a DHA-dFdC solution (75 mg/kg). Ninety minutes later, mice were euthanized to collect major organs (e.g., liver, kidneys, spleen, lung, heart, and pancreas), and the contents of DHA-dFdC in each organs were determined using HPLC after extraction. Similar experiment was repeated in mammary M-wnt tumor-bearing C57BL/6 mice (7-8 mm) following injection of 37.5 mg/kg of DHA-dFdC by i.v. injection.

3.2.10 HPLC

HPLC analysis of DHA-dFdC was performed using an Agilent Infinity 1260 (Agilent Corp., Santa Clara, CA) with a RP-C18 column (Zorbax Eclipse, 5μm, 4.5 mm x 150 mm, Santa Clara, CA).The mobile phase was methanol and water (90:10, v/v). The flow rate was 1.0 ml/min, and the detection wavelength and injection volume were 248 nm and 5 μl, respectively. When cell lysate, mouse plasma or tissue samples were used,

the mobile phase was methanol and 1% (v/v) acetic acid in water (85:15, v/v) with a flow rate of 1.2 ml/min and injection volume of 20 µl. When pancreas samples were used, the wave length of detection of DHA-dFdC was set to 300 nm.

The concentration of dFdC was determined using a previously reported method with modifications [323]. Briefly, an Agilent 1260 Infinity HPLC Station equipped with a RP-C18 column (Zorbax Eclipse, 5µm, 3 mm x 150 mm, Santa Clara, CA) at a controlled temperature of 20°C, an Agilent quaternary pump and Agilent Diode array UV detector was used. The mobile phase was composed of solution A (phosphate buffer, pH adjusted to 3.0 using phosphoric acid) and solution B (acetonitrile). The column was equilibrated using solution A for at least 30 min at a flow rate of 0.6 ml/min, followed by another 30 min at 1.2 ml/min. The gradient elution consisted of 100% solution A for 6 min, followed by a gradual change to 97% solution A and 3% solution B over 1 min. This composition was maintained for 2 min, and the composition was returned back to 100% solution A over 1 min. Between runs, the column was rinsed with methanol:water (90:10), methanol:water (50:50), and then solution A for 15 min each. The flow rate was 1.2 min.

3.2.11 Evaluation of the antitumor activity of DHA-dFdC in animal models

3.2.11.1 Transgenic mice with spontaneously developed pancreatic tumors.

Kras Ink4A$^{+/-}$ spontaneous pancreatic tumor-bearing female mice were bred in the Animal Research Center at the University of Texas at Austin as previously reported [324]. In order to early investigate whether DHA-dFdC is effective in a pancreatic cancer

model that resembles human pancreatic cancer which becomes more aggressive when combined with obesity, mice were transferred to a special diet (D1249, 60% kcal fat, Research Diets, Inc, New Brunswick, NJ) at the age of 16 weeks *ad libitum*. Mouse body weight was monitored twice a week. Mice were then either treated with DHA-dFdC (50 mg/kg, i.p., up to twice weekly, total of 29 doses, n = 5) or left untreated (n = 6) and their health and survival were monitored. In another experiment, following their transfer to a similar high fat diet at 10-12 weeks of age, mice were randomized into 2 groups (n = 6) at the age of 19-20 weeks and were treated with DHA-dFdC group (65 mg/kg, i.p., twice a week) or left untreated until week 30. They were then euthanized and their pancreas were collected, fixed in formalin, and embedded in paraffin blocks for histological evaluation.

3.2.11.2 Mice with subcutaneous Panc-1-Luc tumors.

Male athymic nude mice (6-8 weeks, Charles River) were subcutaneously injected with Panc-1-Luc cells (5 x 10^6 cells in DMEM:Matrigel, 1:1 v/v). Five days later, tumors reached about 130 mm^3 (tumor volumes (V) were calculated based on the longest diameter (L_1) and the shortest diameter (L_2) of each tumor using the equation of $V = ½ \times L_1 \times L_2 \times L_2$). Mice were randomized into 5 groups (n = 5-6) and injected i.p. with DHA-dFdC (in Tween 80/ethanol/water at a ratio of 1:0.52:8.48 with isotonicity adjusted with 5% w/v mannitol, 50 mg/kg or ~ 0.087 mole/kg, n = 6), dFdC (in aqueous 5% w/v mannitol solution, 26.1 mg/kg or ~ 0.087 mole/kg, n = 6), DHA (in Tween 80/ethanol-based solution, 28.7 mg/kg or ~ 0.087 mole/kg, n = 5), or the physical mixture of dFdC (26.1 mg/kg) and DHA (28.7 mg/kg) in a Tween 80/ethanol-based solution (n = 6). As a

vehicle control, mice were also injected with the Tween 80/ethanol-based solution alone (n = 6). Treatments were repeated twice a week for up to 6 times, and tumor growth was monitored using digital calipers.

3.2.11.3 Mice with orthotopic Panc-1-Luc tumors.

Panc-1-Luc cell suspension was prepared at a concentration of about 2 x 10^7 per ml in a 1:1 (v/v) mixture of DMEM and Matrigel. Tumor cells were then injected into the pancreas of male athymic nude mice (6-8 weeks, Charles River) following a surgical procedure [325;326]. Briefly, after mice were anesthetized using isoflurane, the skin and peritoneum were cut open about 1 cm in length using sterile surgical scalpels. The pancreas was pulled out, and about 50 µl of the cell suspension were injected slowly until a small bleb was formed. After the needle was withdrawn, a small cotton plug was applied for 10 s. The pancreas was returned back, the peritoneum was sutured with Monocryl® bioresorbable sutures (Ethicon, Somerville, NJ), and the skin was then closed using surgical clips. Mice were s.c. injected with buprenorphine (0.1 mg/kg) as a pain killer and were left to heal for one week. Tumor progress was monitored using an IVIS® Spectrum imaging system (Caliper, Hopkinton, MA). For IVIS imaging, each mouse was i.p. injected with a luciferin solution (15 mg/ml) at a dose of 0.15 mg/g body weight in sterile DPBS, anesthetized with isoflurane, and imaged 10 min after luciferin injection. Four weeks after tumor implantation, mice with tumors were randomized into 3 groups (n = 5-7) and i.p. injected with DHA-dFdC (50 mg/kg, ~0.087 mole/kg), dFdC (26.1 mg/ml, ~0.087 mole/kg), or left untreated. DHA-dFdC was in a Tween 80/ethanol/water solution

with 5% (w/v) of mannitol, and dFdC was dissolved in sterile mannitol solution (5%, w/v). Treatments were repeated twice a week for a total of 7 times. Thirty days after the first treatment, mice were sacrificed and tumors were dissected from the pancreas, weighed, and fixed in formalin, dehydrated in 70% ethanol, and embedded in paraffin wax.

In both studies mentioned above, the doses were based on the average weight of mice in the same group on the day of injection, and were adjusted only if the weight of an individual mouse was above or below 10% of the average weight.

3.2.11.4 Mice with subcutaneous TC-1 tumors.

The *in vivo* antitumor activity of DHA-dFdC was also evaluated and compared to that of dFdC in female C57BL/6 mice (6-8 weeks, Charles River) with subcutaneously implanted TC-1 mouse lung cancer cells. Briefly, 5×10^5 cells in RPMI were s.c. injected in the right flank of female C57BL/6 mice (Charles River, 6-8 weeks). Eight days later, mice were randomized into 3 groups (n = 5-6) and i.p. injected with DHA-dFdC solution (50 mg/kg, ~ 0.087 mole/kg), dFdC solution (26.1 mg/kg, ~0.087 mole/kg), or left untreated as a control. Treatments were repeated every 3-4 days for a total of 4 times. Tumor growth was monitored using a digital caliper.

3.2.12 Immunohistochemistry

Tumor tissues were sectioned and stained in the Histology and Tissue Analysis Core at Dell Pediatric Research Institute at the University of Texas at Austin or in the

Department of Molecular Carcinogenesis at the University of Texas M.D. Anderson Cancer Center at Science Park (Smithville, Texas) with hematoxylin & eosin (H&E), antibodies against cleaved lamin-A (apoptosis marker), CD-31 (angiogenesis marker), or Ki-67 (proliferation marker). Slides were then scanned, and images were taken using the ScanScope XT (Aperio Technologies, Vista, CA). Pancreas tissues were examined to evaluate the progression of pancreatic cancer (i.e., pancreatic intraepithelial neoplasia-1, -2, and -3 (PanIN-1, -2, and -3), and pancreatic ductal adenocarcinoma (PDAC)).

3.2.13 Statistical analysis

Statistical analyses were completed by performing ANOVA followed by Fisher's protected least significant difference procedure. Survival curve comparisons were constructed using Kaplan−Meier survival analysis (GraphPad Prism, La Jolla, CA). The survival curves were compared using the log rank test (Mantel-Cox test). A p value of ≤ 0.05 (two-tail) was considered statistically significant.

3.3 Results

3.3.1 Synthesis and characterization of DHA-dFdC and ARA-dFdC

DHA was conjugated to Boc_2O-protected dFdC at the 4-(*N*) position via an amide linkage (Scheme 3.1). NMR, mass spectrometry, and LC/MS data confirmed the structure and purity of the compound (Figure 3.1), which is more than 99.8%. The drug appeared as pale yellow dry waxy flakes. As a control, ARA-dFdC, an omega-6 polyunsaturated fatty acid-dFdC conjugate, was synthesized similarly (Scheme 3.1).

3.3.2 Solubility and partition coefficient of DHA-dFdC

Beall *et al*. reported a method to measure the aqueous solubility of drug molecules that are unstable in water [320], which was used in the present study. In order to validate the method, the aqueous solubility of 4-(*N*)-stearoyl dFdC, another lipophilic dFdC conjugate [39], which is stable in water, was measured directly (i.e., direct method) or using the indirect method reported by Beall *et al*. [320]. The solubility of 4-(*N*)-stearoyl dFdC in water was found to be 1.38 ± 1.6 μg/ml when it was measured using the direct method, and 1.39 ± 0.1 μg/ml using the indirect method. Therefore, the indirect method was used to measure the solubility of DHA-dFdC in water, which was found to be 25.15 ± 11.2 μg/ml. The partition coefficient (octanol/PBS 7.4) of DHA-dFdC was also measured using an indirect method by determining its concentration in octanol, before and after partitioning. The log*P* value of DHA-dFdC was found to be 2.24 ± 0.25.

Scheme 3.1. Synthesis of DHA-dFdC and ARA-dFdC.

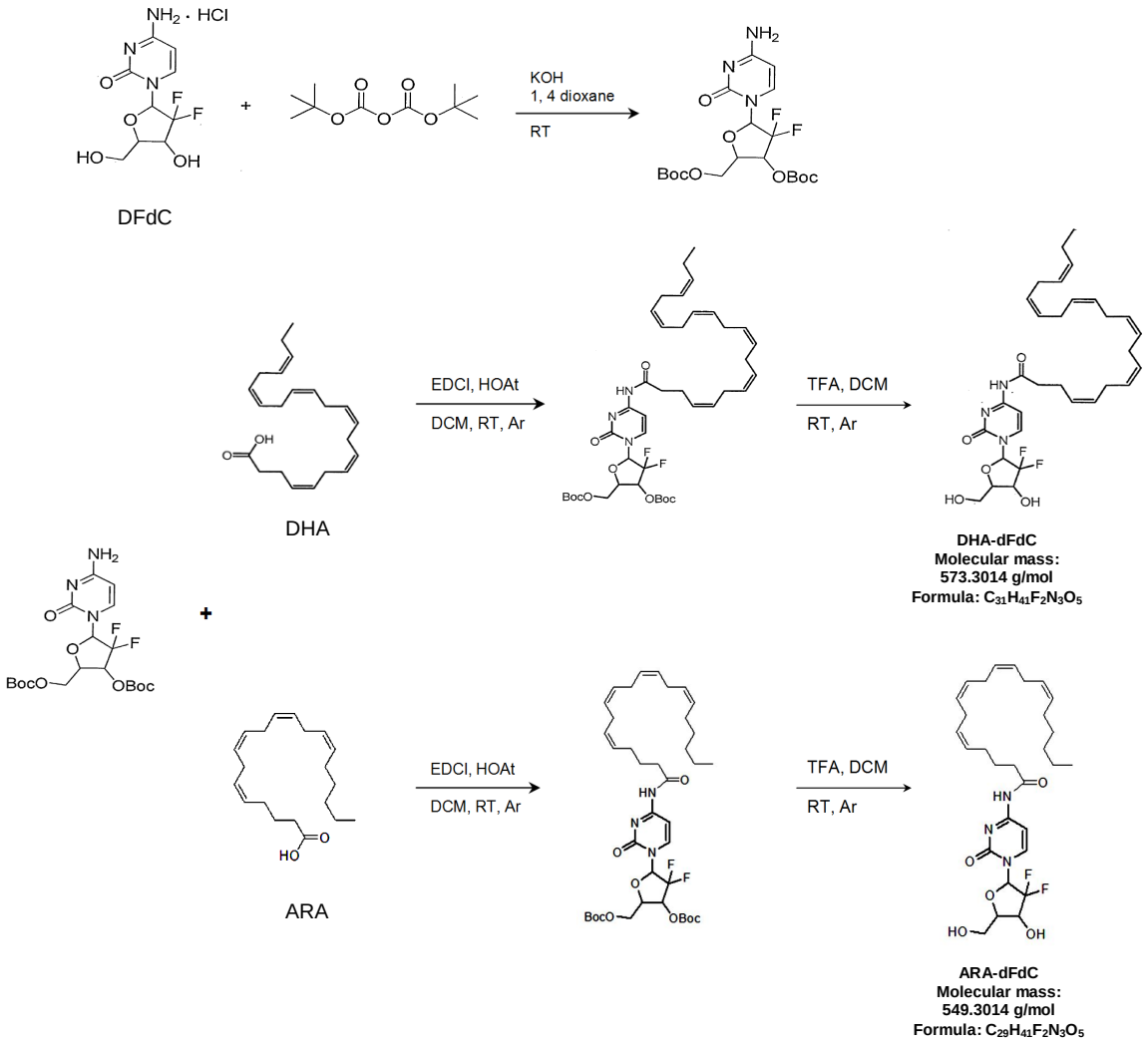

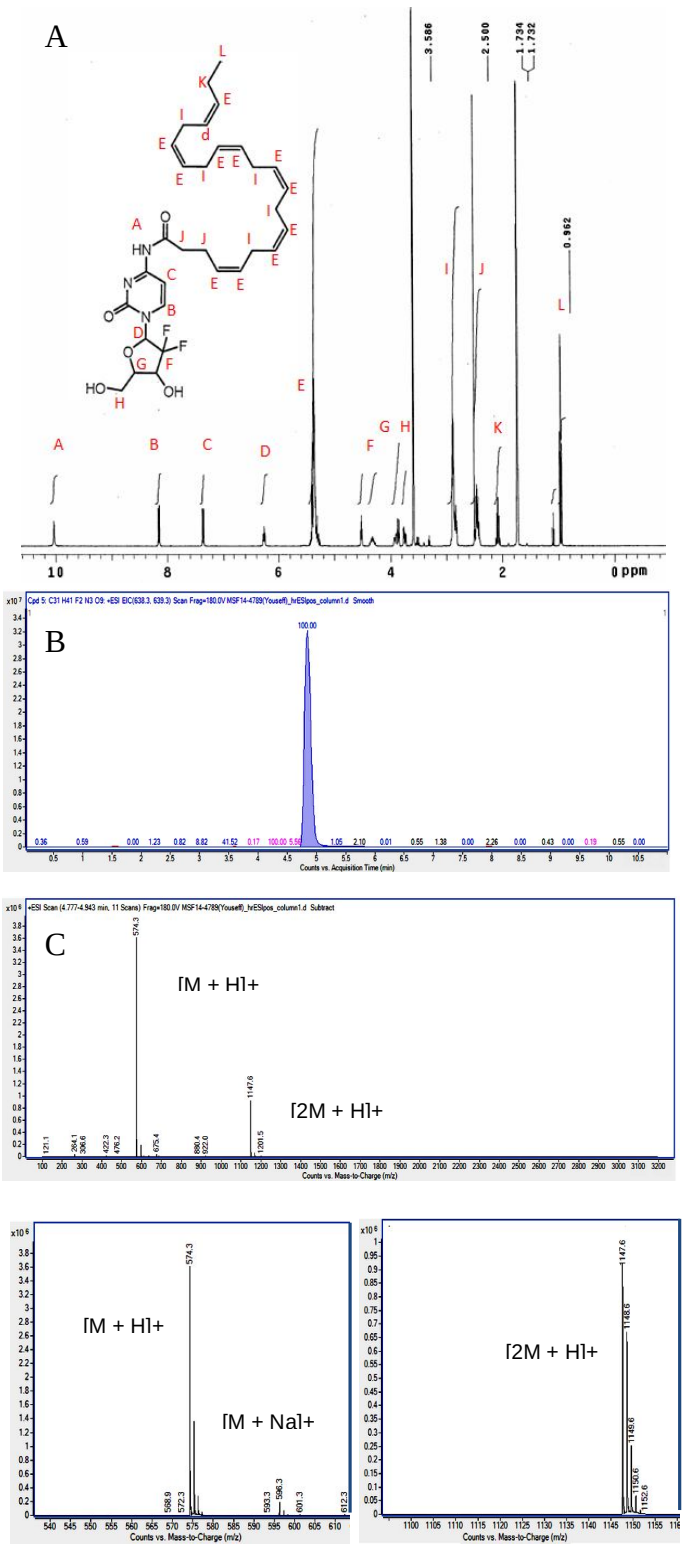

Figure: 3.1

Figure 3.1. Characterization and confirmation of the chemical formula and structure of DHA-dFdC using NMR and mass spectrometry. (A) H^1 NMR spectrum of DHA-dFdC (300 MHz, THF-d^4). (B) Mass spectra of DHA-dFdC, the compound was observed as $[M+H]^+$ m/z at 574.3, $[M+Na]^+$ m/z at 596.3, $[2M+H]^+$ m/z at 1147.6, and $[2M+Na]^+$ m/z at 1169.6. (C) LC/MS chromatogram of DHA-dFdC.

3.3.3 Chemical stability of DHA-dFdC

DHA-dFdC solubilized in a Tween 80/ethanol/water formulation was found to degrade considerably at room temperature (~22^{o}C) (Figure 3.2A). The degradation was significantly slower at 4^{o}C and was also significantly slower in the presence of vitamin E. Vitamin E at 0.01% (w/v) was more effective than at 0.04% (w/v). It was reported previously that a higher concentration of vitamin E may not necessarily have a higher anti-oxidative activity [327]. The effect of temperature on the chemical stability of DHA-dFdC is shown in Figure 3.2B and 3.2C and Table 3.1. The activation energy of the chemical reaction was calculated to be 12.86 kcal/mol.

3.3.4 XRD, UV/Vis and DSC

X-ray diffraction pattern showed that the major crystallinity peaks related to dFdC at the 2Θ values of 9.5, 15.4, 19.0, 21.0, 23.0, 27.5, 30.5, and 35.5 were retained in the physical mixture of dFdC and DHA, but disappeared in DHA-dFdC (Figure 3.3A). UV/Vis scanning revealed that the maximum absorption peak (λ_{max}) of DHA-dFdC in methanol was 248 nm, and there is another absorption peak at 300 nm (Figure 3.3B). The λ_{max} values of dFdC and DHA were 276 nm and 234 nm, respectively (Figure 3.3B). DSC analysis of DHA-dFdC showed a melting point of around 96^{o} C (Figure 3.3C).

Table 3.1: First order degradation rate constant of DHA-dFdC in an aqueous formulation at room temperature (~22^{o} C), 37^{o} C, and 60^{o} C. Data shown are mean ± S.D. (n = 3).

Temperature	**k *(h^{-1})***
Room temperature	0.018 ± 0.001
37° C	0.042 ± 0.005
60° C	0.106 ± 0.009

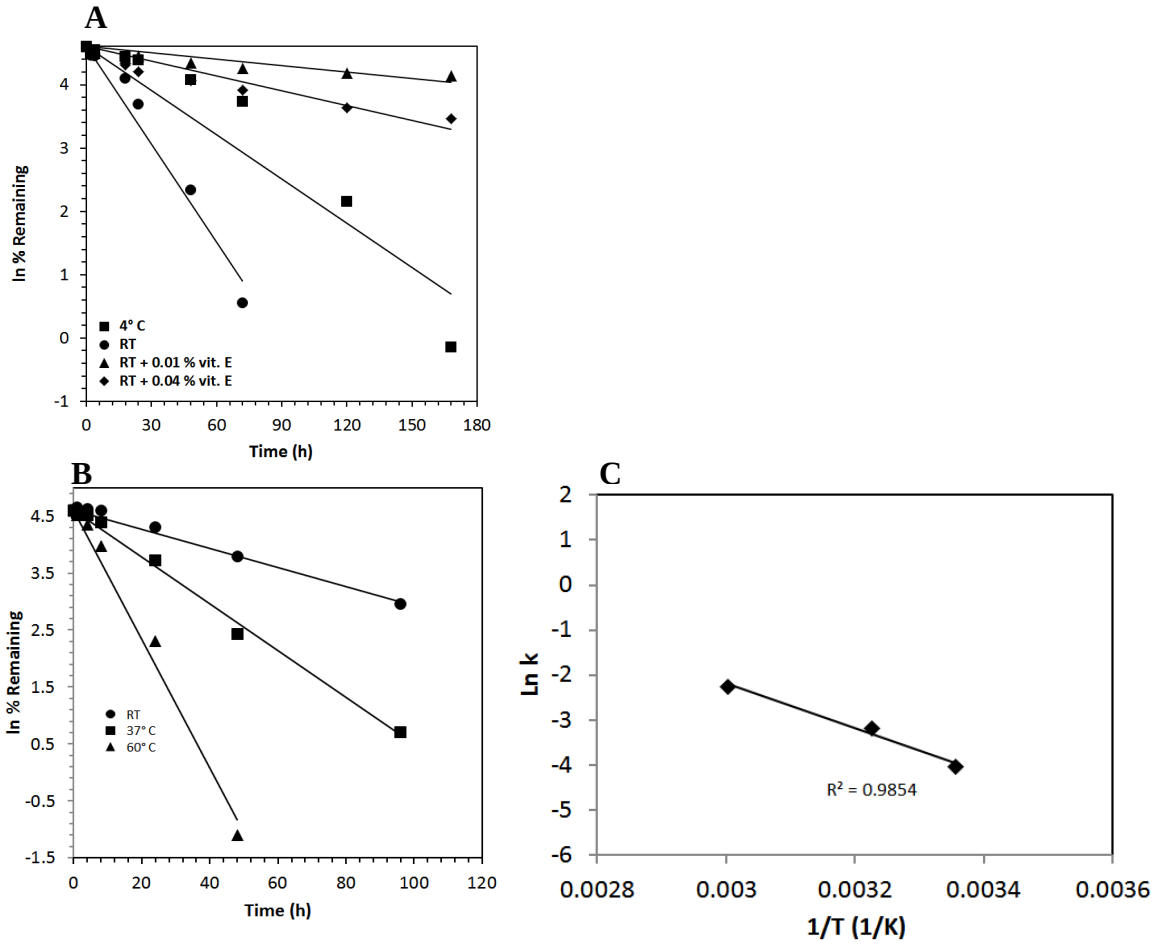
A
ln % Remaining
Time (h)
4° C
RT
RT + 0.01 % vit. E
RT + 0.04 % vit. E
B
ln % Remaining
Time (h)
RT
37° C
60° C
C
Ln k
1/T (1/K)
R² = 0.9854

Figure: 3.2

Figure 3.2. Chemical stability of DHA-dFdC in a Tween 80/ethanol/water formulation. (A) The concentration-time curves of DHA-dFdC at room temperature (~22^{o}C) in a solution that contained 0, 0.01 or 0.04 % (v/v) of vitamin E. As a control, the stability at 4°C was also shown. (B) The effect of temperature on the chemical stability of DHA-dFdC in a Tween 80/ethanol/water formulation. (C) Arrhenius plot showing the effect of temperature on the rate constant of the degradation of DHA-dFdC in a Tween 80/ethanol/water formulation. Data shown are mean from at least 3 repeats, and standard deviations were not shown for clarity.

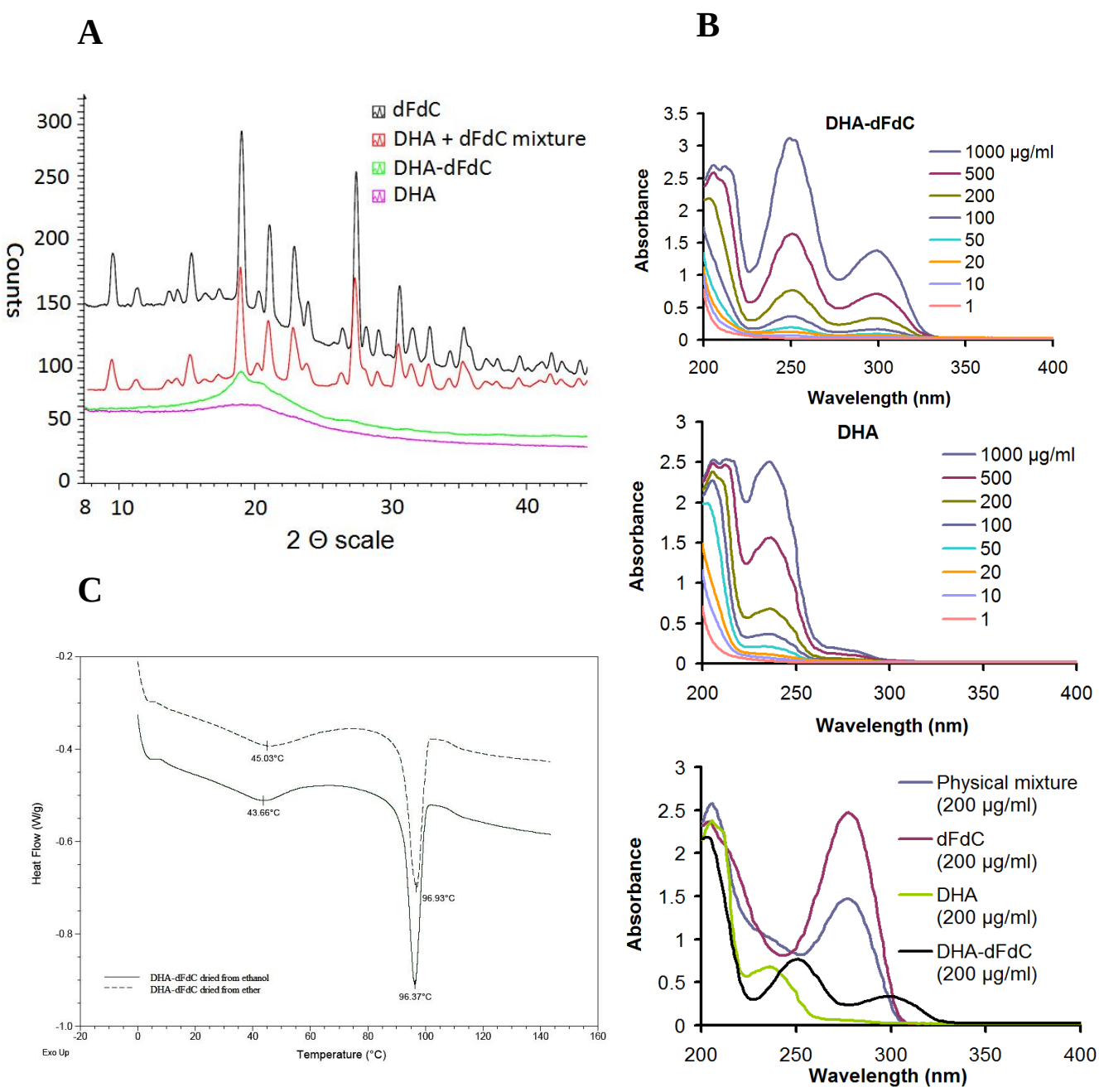
A
dFdC
DHA + dFdC mixture
DHA-dFdC
DHA
Counts
2 Θ scale
B
DHA-dFdC
1000 µg/ml
500
200
100
50
20
10
1
Absorbance
Wavelength (nm)
DHA
Physical mixture (200 µg/ml)
dFdC (200 µg/ml)
DHA (200 µg/ml)
DHA-dFdC (200 µg/ml)
C
Heat Flow (W/g)
Exo Up
Temperature (°C)
45.03°C
43.66°C
96.93°C
96.37°C
DHA-dFdC dried from ethanol
DHA-dFdC dried from ether

Figure: 3.3

Figure 3.3. Physicochemical characterization of DHA-dFdC. (A) XRD patterns of DHA-dFdC, dFdC, DHA, and the mixture of dFdC and DHA (1:1, m/m, DHA+dFdC). (B) UV/Vis spectra of DHA-dFdC and DHA at various concentrations, and a comparison of the UV/Vis spectra of DHA-dFdC, dFdC, DHA, and DHA+dFdC. (C) DSC analyses of DHA-dFdC precipitated from ethanol solution (solid line) or ether (dashed line).

3.3.5 The cytotoxicity of DHA-dFdC against tumor cells in culture

The cytotoxicity of DHA-dFdC was evaluated with the NCI-60 DTP Human Tumor Cell Lines, and the results are shown in Table 3.2. In addition, the ratios between the GI50 values of DHA-dFdC (μM) and those of dFdC against all tested cell lines were plotted for comparison (Figure 3.4). Values higher than 1 indicate higher DHA-dFdC antiproliferative activity compared to dFdC, in a particular cell line, and the opposite is correct for values less than 1 (Figure 3.4). The cytotoxicity of DHA-dFdC was also evaluated in various mouse and human pancreatic cancer cell lines (i.e., Panc-02, Bx-PC3, Panc-1) using an MTT assay, because the NCI-60 human tumor cell lines do not include pancreatic tumor cells. In pancreatic cancer cell lines tested, the anti-proliferative activity of gem-DHA was found to be concentration dependant (Figure 3.5A-E), which was also noticeable with its apoptotic activity against murine pancreatic cancer panc-02 cells (Figure 3.5F and G). Furthermore, DHA-dFdC exhibited a stronger anti-proliferative activity compared to dFdC or the physical mixture of dFdC and DHA (1:1, molar ratio), while the physical mixture of DHA and dFdC was not more cytotoxic than dFdC alone (Figure 3.5A, B, D-F). LDH assay also confirmed that DHA-dFdC was more cytotoxic than dFdC in Panc-02 tumor cells (Figure 3.54C).

In order to understand the effect of the omega-3 polyunsaturated fatty acid nature of the DHA (i.e., the docosahexaenoyl group) in the DHA-dFdC on its cytotoxicity against tumor cells, the cytotoxicity of ARA-dFdC, a conjugate of dFdC and arachidonic acid (ARA), an omega-6 polyunsaturated fatty acid, was also evaluated in BxPC-3 and MIA PaCa-2 cells. ARA-dFdC was not significantly more cytotoxic than dFdC (Figure

3.5H), indicating that the omega-3 fatty acid nature of the DHA in the DHA -dFdC is critical for the cytotoxicity of DHA-dFdC in tumor cells.

Table 3.2: Anti-proliferative and cytotoxic activities of DHA-dFdC against NCI-60 DTP Human Tumor Cell Lines. Values shown are all in in μM. GI_{50} is the concentration of DA-dFdC at which tumor cell growth was inhibited by 50%. TGI is the concentration at which tumor cell growth was completely inhibited. LC_{50} is the concentration at which 50% of the tumor cells were killed.

	Cell line	***GI50 (μM)***	***TGI (μM)***	***LC50 (μM)***
		DHA-dFdC	***DHA-dFdC***	***DHA-dFdC***
Leukemia	**CCRF-CEM**	0.0507	17.9	> 100
	HL-60 (TB)	0.029	14.8	> 100
	K-562	0.0674	46.9	> 100
	MOLT-4	0.0692	13.3	93.1
	RPMI-8226	0.0538	26.9	> 100
	SR	0.0141	28.8	> 100
Non-small cell lung cancer	**A549/ATCC**	0.0326	15.4	43.8
	EKVX	0.852	20.4	52.9
	HOP-62	0.0186	4.47	35.2
	HOP-92	0.771	34.5	> 100
	NCI-H226	0.0672	2.75	39.2
	NCI-H23	0.0157	12.7	56.6
	NCI-H322M	1.18	19	46
	NCI-H460	0.0153	11.8	43.3
	NCI-H522	0.028	14.2	54.1
Colon Cancer	**COLO 205**	0.143	14.1	50.7
	HCC-2998	10.6	26.7	67.5
	HCT-116	0.0311	15.3	44.4
	HCT-15	1.86	25.3	87.5
	HT29	0.0683	17.6	45.1
	KM12	1.05	20.2	51.9
	SW-620	0.0759	23.2	84.4
CNS Cancer	**SF-268**	0.0542	12.9	42.3
	SF-295	0.0791	10.9	37.5
	SF-539	0.0287	0.538	30.6
	SNB-19	0.0223	12.4	61.9

Table 3.2 (continued)

	SNB-75	0.401	25.1	> 100
	U251	0.0305	15.2	43.9
Melanoma	**LOX IMVI**	0.0414	1.07	77.9
	MALME-3M	10.1	22.8	51.6
	M14	0.0243	0.21	34.8
	MDA-MB-435	0.311	18.1	43.3
	SK-MEL-2	13.2	29.8	67.6
	SK-MEL-28	10.1	23.3	53.8
	SK-MEL-5	0.29	17.1	42.1
	UACC-257	0.518	22.9	56.1
	UACC-62	0.0494	12.5	43
Ovarian Cancer	**IGROV1**	3.45	22.5	55.3
	OVCAR-3	11.1	23.5	49.6
	OVCAR-4	14.5	28.8	57.2
	OVCAR-5	0.0821	22.5	63.8
	OVCAR-8	0.0345	11.4	43.2
	NCI-ADR-RES	0.0338	14.8	46.9
	SK-OV-3	0.11	14.2	> 100
Renal Cancer	**786-0**	< 0.01	14.2	> 100
	A498	0.0855	16.1	51.9
	ACHN	< 0.01	10.1	39.4
	CAKI-1	0.0253	11.7	34.3
	RXF 393	0.14	15.1	45.1
	SN12C	0.197	4.49	33.8
	TK-10	11.5	29.4	74.9
	UO-31	0.0835	12	37.9
Prostate Cancer	**PC-3**	10.7	27	67.8
	DU-145	0.0396	12.5	35.3
Breast Cancer	**MCF7**	< 0.01	13.4	42.3
	MDA-MB-231/ATCC	6.82	22.2	53.5
	HS 578T	17	45.5	> 100
	BT-549	0.0454	16.3	44.2
	T-47D	0.0996	17.6	71.9

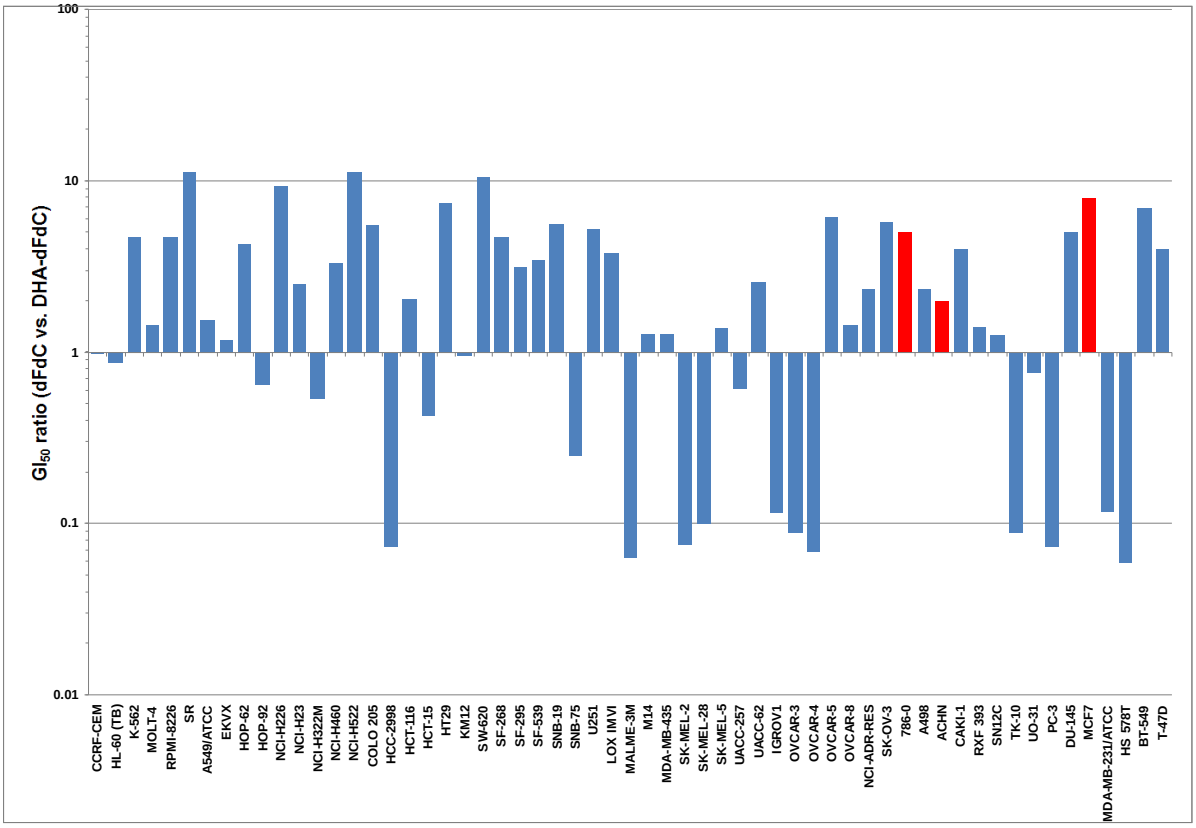
GI50 ratio (dFdC vs. DHA-dFdC)
100
10
1
0.1
0.01
CCRF-CEM
HL-60 (TB)
K-562
MOLT-4
RPMI-8226
SR
A549/ATCC
EKVX
HOP-62
HOP-92
NCI-H226
NCI-H23
NCI-H322M
NCI-H460
NCI-H522
COLO 205
HCC-2998
HCT-116
HCT-15
HT29
KM12
SW-620
SF-268
SF-295
SF-539
SNB-19
SNB-75
U251
LOX IMVI
MALME-3M
M14
MDA-MB-435
SK-MEL-2
SK-MEL-28
SK-MEL-5
UACC-257
UACC-62
IGROV1
OVCAR-3
OVCAR-4
OVCAR-5
OVCAR-8
NCI-ADR-RES
SK-OV-3
786-0
A498
ACHN
CAKI-1
RXF 393
SN12C
TK-10
UO-31
PC-3
DU-145
MCF7
MDA-MB-231/ATCC
HS 578T
BT-549
T-47D

Figure: 3.4

Figure 3.4: Comparison between the IG50-ratio values between DHA-dFdC and dFdC. Note that all the values higher than 1 and less than 10 represent superior anti-proliferative activity in favor of DHA-dFdC, and the opposite for the values higher than 0.1 and lower than 1. Red bars represent those cell lines in which DHA-dFdC, at its lower concentration, inflicted a % proliferation less than 50% of control (log IG50 values of less than - 8.0).

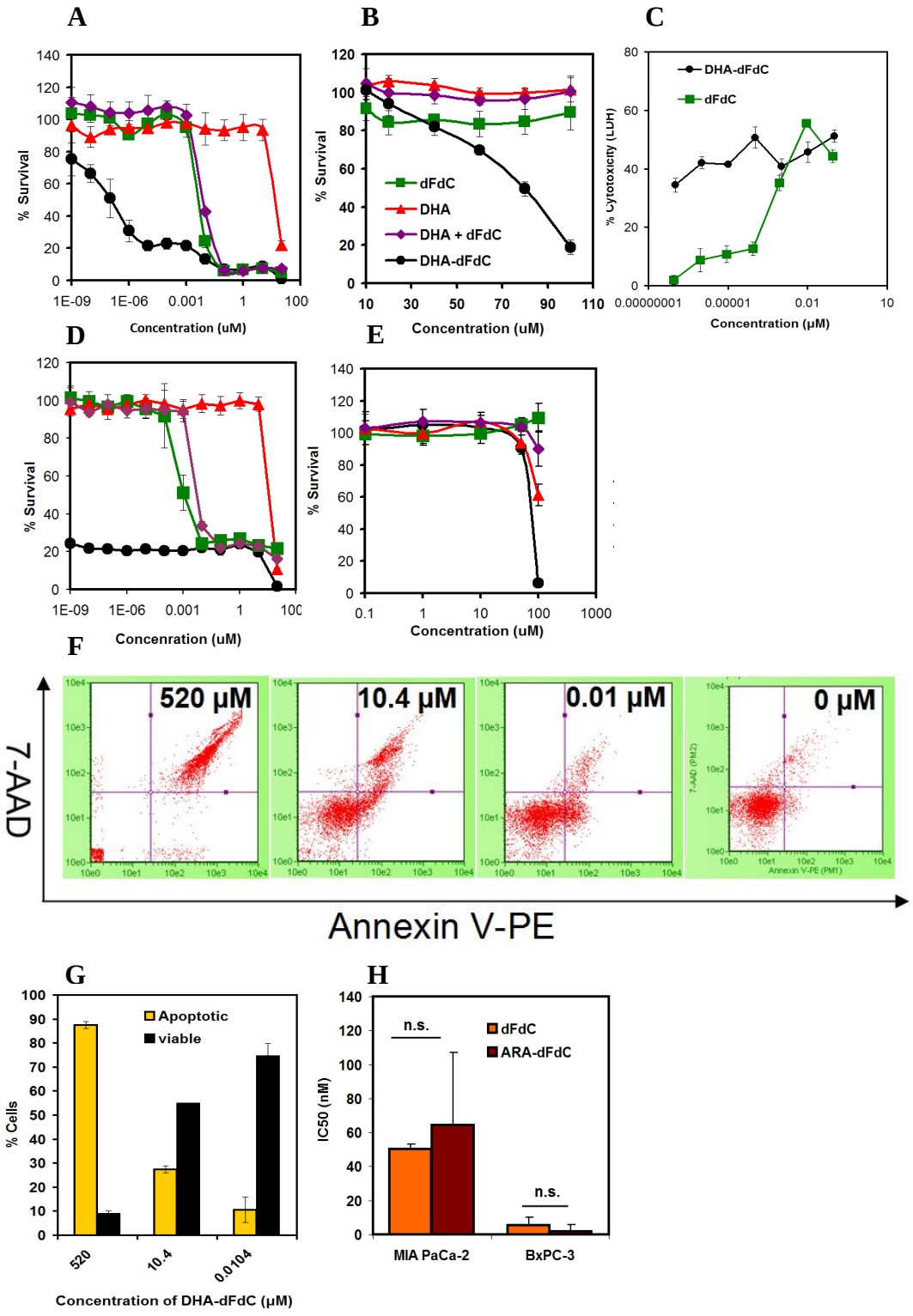
A
% Survival
Concentration (uM)
B
% Survival
dFdC
DHA
DHA + dFdC
DHA-dFdC
Concentration (uM)
C
DHA-dFdC
dFdC
% Cytotoxicity (LDH)
Concentration (µM)
D
% Survival
Concenration (uM)
E
% Survival
Concentration (uM)
F
520 µM
10.4 µM
0.01 µM
0 µM
7-AAD
Annexin V-PE
G
Apoptotic
viable
% Cells
Concentration of DHA-dFdC (µM)
H
n.s.
dFdC
ARA-dFdC
IC50 (nM)
MIA PaCa-2
BxPC-3

Figure: 3.5

Figure 3.5. Anti-cancer activity of DHA-dFdC and molar equivalent concentrations of other treatments against cancer cell lines. (A) Anti-proliferative activityagainst Panc-02 cells after 48 h, and (B) after 4 h. (C) cytotoxic activity (as represented by LDH release) of either DHA-dFdC or dFdC in Panc-02 cells after 48 h. Antiproliferative activity of DHA-dFdC and molar equivalent concentrations of other treatments against (D) BxPC-3 after 72 h, and (E) Panc-1-Luc after 24 h. (F) Pro-apoptotic activity of DHA-dFdC against Panc-02 cells determined using flow cytometry after Annexin V-PE and 7-AAD staining. Quarters are divided as follows: top left, cellular debris, bottom left: live cells, top right: late apoptotic cells, and bottom right: early apoptotic cells. (G) Pro-apoptotic activity of different concentrations of DHA-dFdC. (H) Comparison of the IC_{50} values of dFdC or ARA-dFdC in MIA PaCa-2 and in BxPC-3 cells (n.s. is non-significant). In all sub-figures, except (G), data shown are means ± standard derivations ($n \geq 3$).

3.3.6 Uptake of DHA-dFdC by tumor cells in culture

The percentage of DHA-dFdC that was taken up by Panc-02 cells after 4 h of incubation is shown in Figure 3.6. The % uptake of the DHA-dFdC was about 10-fold higher than that of dFdC.

3.3.7 Pharmacokinetics and biodistribution of DHA-dFdC

The plasma DHA-dFdC levels in mice at different time points after i.v. injection are shown in Figure 3.7A. The elimination of DHA-dFdC in plasma appears to follow a bi-exponential model. Selected pharmacokinetics parameters are shown in Figure 3.7B. An analysis of the concentrations of DHA-dFdC in several major organs in healthy mice, 60 min after i.v. injection at a dose of 75 mg/kg showed that the highest percent of the injected DHA-dFdC dose was found in mouse pancreas (Figure 3.7C). Therefore, the pharmacokinetics of DHA-dFdC in mouse pancreas after pre-determined time points, after i.v. injection was also determined and reported in Figure 3.8. For comparison, pancreatic levels of dFdC were also measure at pre-determined time points (Figure 3.8). It is clear that DHA-dFdC remains in the pancreas for longer periods compared to dFdC. For example, after 90 min, the % injected dose ofDHA-dFdC per gram of pancreatic tissues was more than 10 times than that of dFdC, in addition, DHA-dFdC is retained in the pancreas at a considerable amount in the pancreas after 5 h, while dFdC almost disappeared after 90 min.

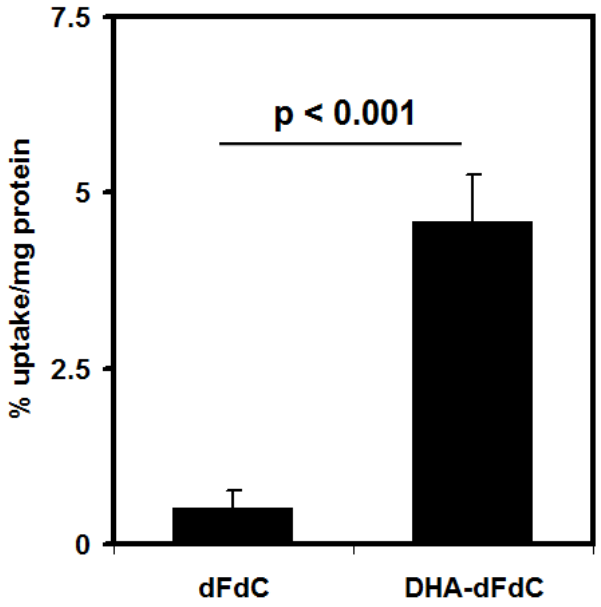

Figure: 3.6

Figure 3.6. Cellular uptake % of DHA-dFdC compared to that of dFdC. Panc-02 were seeded at 250,000 cells/well in a 12 well-plate for overnight followed by treatment with DHA-dFdC (10 μM in DMSO) or dFdC (10 μM in cell culture medium). After 4 h, media were removed, cells were lysed, and DHA-dFdC and dFdC were extracted using ethyl acetate or acetonitrile, respectively. % cellular uptake following treatment with either drug was calculated following analysis with HPLC. Protein content was measured in each cell lysate and used to normalize the value of % cellular uptake to the protein content. Data represent means ± standard deviations, n = 3-4.

A

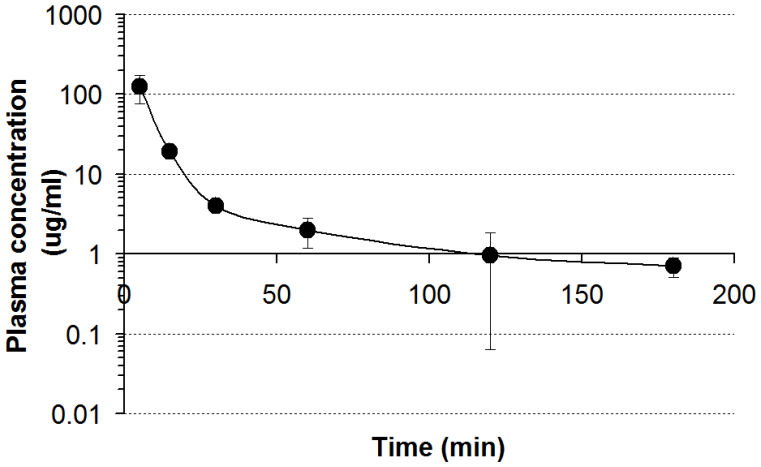

B

Parameter	Value
A (µg/ml)	334.5
B (µg/ml)	4.56
α (min. $^{-1}$)	0.205
β (min. $^{-1}$)	0.012
$t_{1/2\alpha}$ (min.)	3.38
$t_{1/2\beta}$ (min.)	57.75
AUC (µg.min/ml)	1998.3
K_{10} (min. $^{-1}$)	0.17
K_{12} (min. $^{-1}$)	0.033
K_{21} (min. $^{-1}$)	0.015
V_c (L/kg)	0.221
C_{max} (µg/ml)	339.05
Cl (ml/min. Kg)	37.62
V_{ss} (L/kg)	0.7
MRT (min.)	18.7

C

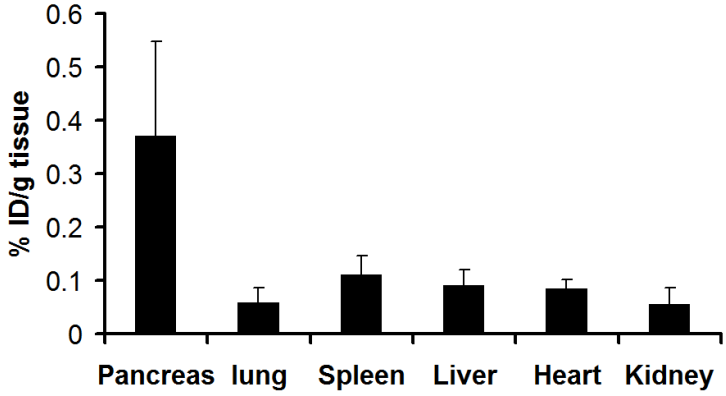

Figure: 3.7

Figure 3.7. Pharmacokinetics and biodistribution of DHA-dFdC. (A) Plasma DHA-dFdC concentrations at various time points following i.v. injection into C57BL/6 mice. (B) Selected pharmacokinetics parameters when data in A were fitted in two-compartment model using WinNonLin. (C) Biodistribution profile of DHA-dFdC in healthy BALB/c mice 60 min after i.v. injection (DHA-dFdC dose is 75 mg/kg). Data in A, and C are mean ± S.D. (n = 3).

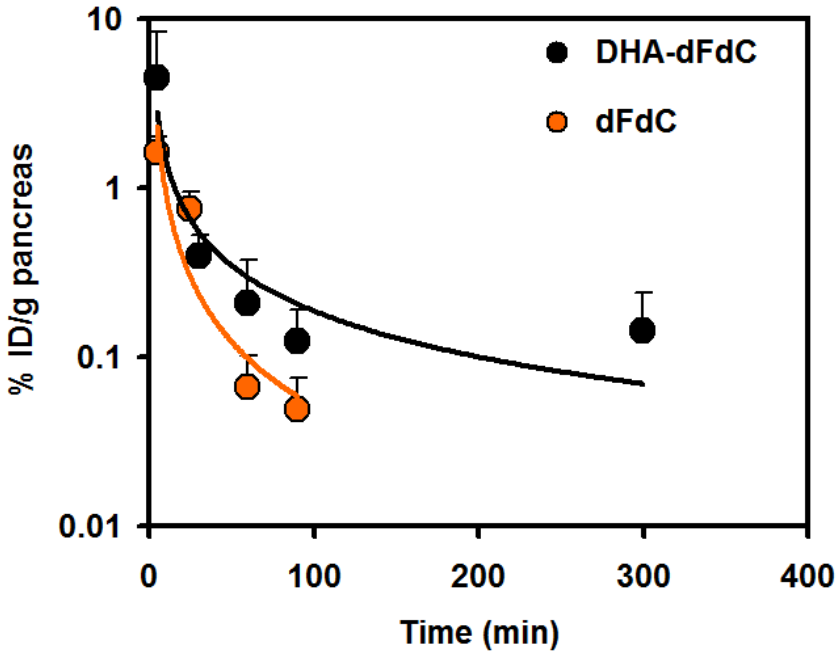
10
1
0.1
0.01
% ID/g pancreas
0
100
200
300
400
Time (min)
DHA-dFdC
dFdC

Figure: 3.8

Figure 3.8. Pancreatic levels of DHA-dFdC compared to those of dFdC following i.v. injection of BALB/c mice with either agents (75 mg/kg). After predetermined time intervals, mice were sacrificed, and their pancreases were collected, and either DHA-dFdC or dFdC were extracted and their amounts analyzed by HPLC. Values are means ± SD, n = 3).

3.3.8 Antitumor activity of DHA-dFdC in mouse models

Because the cytotoxicity of the DHA-dFdC was up to 10^5-fold higher than dFdC in pancreatic tumor cell lines and DHA-dFdC showed unexpected high distribution in mouse pancreas, the in vivo antitumor activity of DHA-dFdC was initially tested in Kras-Ink4A$^{+/-}$ transgenic mice that spontaneously develop pancreatic ductal adenocarcinoma (PDAC). Data in Figure 3.9 showed that treatment with DHA-dFdC significantly extended the survival of the transgenic mice. In another animal study involving the transgenic mice with pancreatic tumors, a noticeable retardation of tumor progression was noticed in DHA-dFdC group, when compared to untreated group (Figure 3.10 and Table 3.3). In the untreated group, 4 of 6 mice showed complete transformation of the pancreas into pancreatic ductal adenocarcinoma (PDAC), while the other 2 showed several foci of PDAC and extensive PanIN-2 and PanIN-3 lesions (Figure 3.10 and Table 3.3). DHA-dFdC-treated group (65 mg/kg, twice a week for 10 weeks) showed only 2 of 6 mice with complete PDAC transformation, and another one with almost half the pancreas with PDAC transformation. One pancreas appeared to be close to normal, with minimum PanIN-1 and -2 lesions. The other two pancreases showed variable expressions of PanIN-1, -2, and -3, with only very limited PDAC foci (Figure 3.10, Table 3.3).

The antitumor activity of DHA-dFdC was then evaluated and compared to that of the dFdC or the physical mixture of dFdC and DHA in mice with subcutaneously injected human Panc-1-Luc tumor cells. As shown in Figure 3.11A, at the dosing regimen used, DHA-dFdC significantly inhibited Panc-1-Luc tumor growth, as compared to the vehicle control, but the molar equivalent doses of dFdC alone, DHA alone, or the physical

mixture of dFdC and DHA did not significantly inhibit the tumor growth. Shown in Figure 3.11B are body weights of mice that were treated with DHA-dFdC. In mice with orthotopic Panc-1-Luc tumors, DHA-dFdC effectively inhibited the tumor growth, but dFdC at the dosing regimen used did not show significant activity (Figure 3.12A-C). Shown in Figure 3.12D is the body weights of mice that were treated with DHA-dFdC. H&E staining of the tumor tissues revealed that tumors in mice that were left untreated have dense cellular matrix with tightly-packed tumor cells and small intracellular spaces (Figure 3.13A). In addition, several areas of necrosis can also be seen in the centers of the tumors (lined in green). A similar pattern was observed in tumors in mice that were treated with dFdC, but with less necrosis. On the contrary, tumors in mice that were treated with DHA-dFdC showed less densely packed cancer cells, with a much larger cytoplasm to nucleus ratio and intracellular spaces. Several pyknotic cells with condensed chromatin can also be seen in tumors in mice that were treated with DHA-dFdC. Ki-67 staining showed that there is a significantly lower percent of Ki-67-positive cells in tumors in mice that were treated with DHA-dFdC than in mice that were treated with dFdC (Figure 3.13A and B). Anti-cleaved lamin A staining showed a significantly higher percent of positive staining in tumors in mice that were treated with DHA-dFdC than in mice that were untreated (Figure 3.13A and C), whereas the extent of cleaved lamin A positive staining in tumors in mice that were treated with dFdC was not different from that in mice that were not treated (Figure 3.13A and C). Finally, anti-CD-31 staining showed the micro-vessel density (MVD) in tumors in mice that were treated with DHA-dFdC was significantly lower than in mice that were not treated, but the MVD value in

tumors in mice that were treated with dFdC was not different from that in mice that were not treated (Figure 3.13A and D).

Finally, data in Figure 3.14A showed that DHA-dFdC was much more cytotoxic than dFdC, DHA, or a molar equivalent of a mixture of the two against TC-1 cells in culture (Figure 3.14 A). DHA-dFdC was more effective than the molar equivalent dose of dFdC in controlling the growth of subcutaneously implanted TC-1 mouse lung cancer tumors (Figure 3.14B), demonstrating that the in vivo antitumor activity of DHA-dFdC is not limited to pancreatic tumors. Shown in Figure 3.14C are the body weights of TC-1 tumor-bearing mice after they were treated with DHA-dFdC.

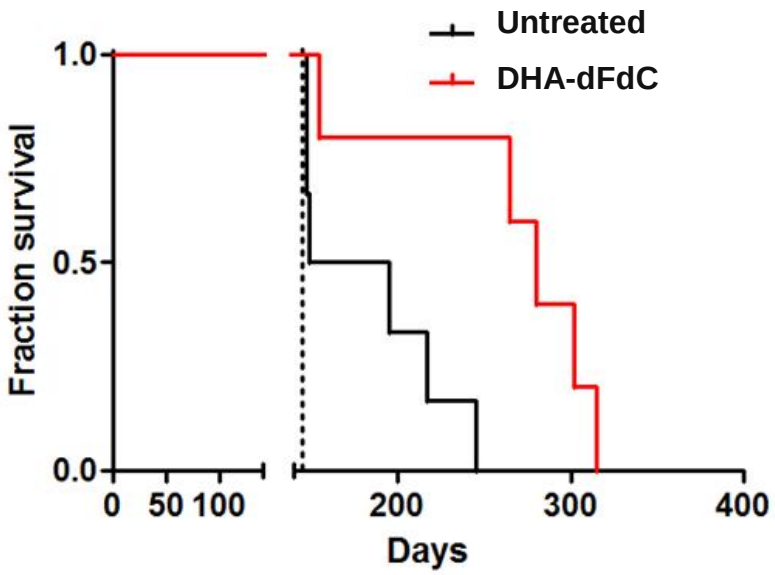
Untreated
DHA-dFdC
Fraction survival
1.0
0.5
0.0
0
50
100
200
300
400
Days

Figure: 3.9

Figure 3.9: Survival curves of female Kras Ink4A$^{+/-}$ mice treated with DHA-dFdC or left treated. Mice were moved to high fat diet at 16-17 weeks of age, DHA-dFdC treatment (50 mg/kg, in Tween 80/ethanol/5% mannitol aqueous solution, i.p. injection for twice a week) was started when mice were 20 weeks old.

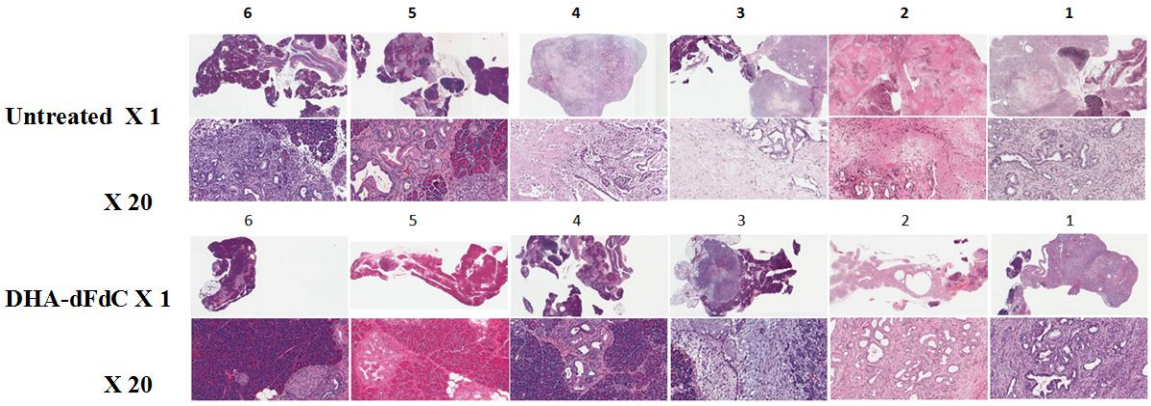

Figure: 3.10

Figure 3.10: Histological comparison between spontaneous pancreatic tumors extracted from transgenic mice that have been treated with DHA-dFdC or left untreated (n=6).

Table 3.3: Evaluation of spontaneous pancreatic tumors extracted from transgenic mice.

#	Normal pancreatic tissue	PanIN 1	PanIN 2	PanIN 3	Adenocarcinoma
Control 1	10 %	++	++++	++++	90 %
Control 2	None	++	++++	++++	100 %
Control 3	30 %	++	+++	+++	About 70 %
Control 4	None	+	+++	+++	100 %
Control 5	About 60 %	+++	++	++	Many foci
Control 6	More than 80 %	+++	+	+	small focus
DHA-dFdC 1	About 10 %	+	+++	+++	> 90 % (poorly differentiated)
DHA-dFdC 2	About 20 %	++	+++	+++	About 80 %
DHA-dFdC 3	About 35 %	+++	+++	++	Significant area (> 65 %), poorly differentiated
DHA-dFdC 4	About 80 %	+++	++	+	Small foci
DHA-dFdC 5	More than 90 %	+	+	+	None
DHA-dFdC 6	More than 90 %	+	+	+	None

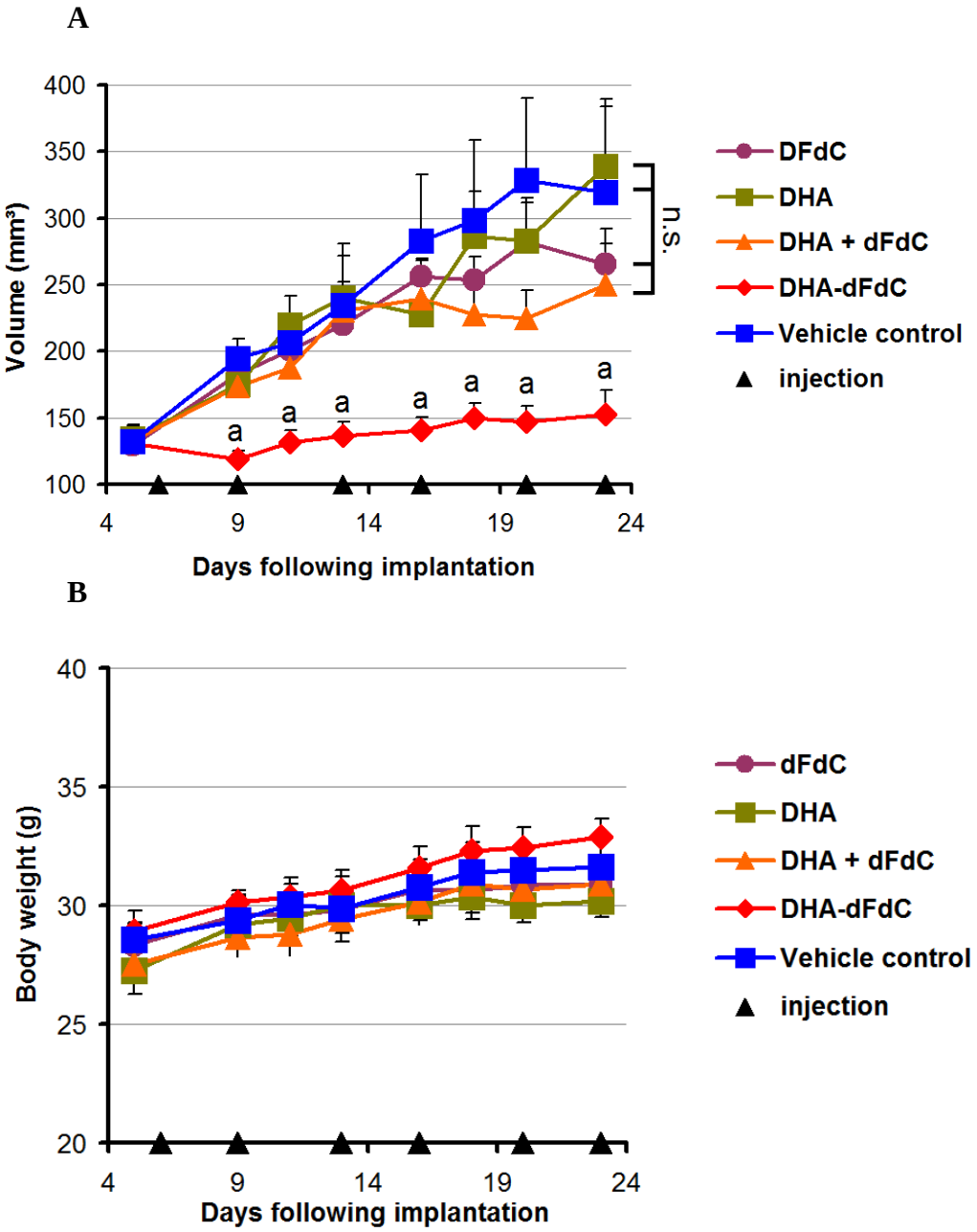
A
400
350
300
250
200
150
100
Volume (mm³)
n.s.
a
a
a
a
a
a
4
9
14
19
24
Days following implantation
DFdC
DHA
DHA + dFdC
DHA-dFdC
Vehicle control
injection
B
40
35
30
25
20
Body weight (g)
4
9
14
19
24
Days following implantation
dFdC
DHA
DHA + dFdC
DHA-dFdC
Vehicle control
injection

Figure: 3.11

Figure 3.11. Antitumor activity of DHA-dFdC against Panc-1-Luc human pancreatic tumors implanted subcutaneously in athymic nude male mice. Tumors were implanted (5 x 10^6 cells/mouse) in the right flank of male athymic nude mice. On day 5 following implantation, mice were then treated with DHA-dFdC (50 mg/kg) or molar equivalent doses of DHA, dFdC, or DHA + dFdC. Mice in the Vehicle control group were injected with a solution of Tween 80/ethanol in 5% of mannitol, which was also used to with DHA-dFdC, DHA, and DHA + dFdC mixture, while dFdC alone was dissolved in aqueous 50% mannitol solution. All treatments were given by i.p. injection as twice/week (A) Tumor growth curves. (B) Mouse body weights during treatments. Data are means ± standard errors (n = 5-6), ^{a} $p < 0.05$, DHA-dFdC vs. other groups, n.s. is non-significant.

3.4 Discussion

In the present study, we reported the synthesis of DHA-dFdC and presented ^{1}H NMR, MS, and LC/MS data to confirm its structure and purity (Scheme 3.1, Figure 3.1). DHA-dFdC showed potent broad spectrum antitumor activity as it inhibited the growth of all of the NCI-60 human tumor cell lines and several human and mouse pancreatic tumor cell lines (Table 3.2, Figure 3.5). Unexpectedly, biodistribution studies showed that DHA-dFdC had a relatively high accumulation and slow pancreatic clearance after injection into mice. Importantly, DHA-dFdC showed strong antitumor activity in mouse models with spontaneously developed pancreatic tumors and also in mice with subcutaneous or orthotopic Panc-1 human pancreatic tumor xenografts (Figures 3.9-3.13).

There have been numerous previously reported dFdC derivatives [306;308;311;313;315;328-334], including our own [193], but in many cases, the derivatives were not as cytotoxic as dFdC alone against tumor cells in culture [308;329;330]. Similarly, the chemical conjugates of DHA and other cancer chemotherapeutic agents such as paclitaxel, doxorubicin, and 10-hydroxycamptothecin were previously reported as well, but the conjugates were not more cytotoxic than the original agents in cell culture [290-292]. In fact, these conjugates were considered as prodrugs that need to be converted to active forms in order to be effective ([290;292]. Therefore, it was unexpected that DHA-dFdC showed a potent broad spectrum antitumor activity and was significantly more cytotoxic than dFdC in pancreatic cancer cells (e.g.,

in BxPC-3 cells, the IC_{50} value of DHA-dFdC was more than 100,000 fold smaller than that of the dFdC).

DHA-dFdC induced tumor cells (Panc-02) to undergo apoptosis (Figure 3.5F), and it is expected that the dFdC formed following hydrolysis of DHA-dFdC contributed to the apoptosis. However, the mechanism underlying the potent antitumor activity of DHA-dFdC appears to be different from that of dFdC alone, and may not even be primarily attributed to the dFdC's activity in inhibiting nucleic acid synthesis [335-337]. For example, although the conjugation of DHA to the 4-NH_2 group on the dFdC is expected to prevent deanimation, but the mere protection of the 4-NH_2 is not sufficient to increase the anti-cancer activity of dFdC , as the 4-(*N*)-stearoyl dFdC, a conjugate of dFdC with stearate, and ARA-dFdC, a conjugate of dFdC with ARA, an omega-6 PUFA, both in the 4-NH_2 position, were not more cytotoxic than dFdC against various dFdC-sensitive cancer cell lines (e.g., BxPC-3 and MIA PaCa-2) [179;219;338] (Figure 3.5 and unpublished data). Therefore, it is unlikely that the potent antitumor activity of the DHA-dFdC was simply due to the protection of the vulnerable amine group on the dFdC. Instead, it appears that the omega-3 PUFA nature of the docosahexaenoyl group in the DHA-dFdC (i.e., 22:6 (n-3)) is critical for its strong antitumor activity. ARA is a PUFA as well, but it is an omega-6 PUFA, and ARA-dFdC was not more cytotoxic than dFdC in the cell lines tested. It was reported previously that epoxy derivatives of DHA, formed by the action of cytochrome p450 epoxygenases, exhibited anti-proliferative, anti-angiogenic, and anti-metastatic activity [339]. It is expected that DHA-dFdC may also undergo oxidation at the 4-5, 7-8, 10-11, 13-14, 16-17, or 19-20 sites on its

docosahexaenoyl moiety to form the epoxy derivatives, and the oxidized metabolites of DHA-dFdC may have antitumor activity. The potent *in vitro* cytotoxicity of the DHA-dFdC may also be related to the more extensive cellular uptake of the DHA-dFdC by tumor cells in culture than the uptake of the dFdC alone (Figure 3.6), but may not be entirely attributed to the increased cellular uptake. For example, when Panc-02 cells were treated with DHA-dFdC or dFdC at high concentrations (e.g., 10-100 μM), cytotoxicity was detected after only 4 h of co-incubation with DHA-dFdC, but not with dFdC (Figure 3.5B). dFdC, which inhibits nucleic acid synthesis and thus cell proliferation, showed significant activity only after prolonged incubation (Figure 3.5A). Therefore, it is possible that DHA-dFdC, at least at high concentrations, may cause tumor cell death in a cell cycle-independent manner, and the cell death may not be due to the fatty acid nature of the DHA in the DHA-dFdC, because DHA alone at the same concentrations did not show cytotoxicity after 4 h of co-incubation (Figure 3.5B). Clearly, the mechanisms underlying the cytotoxicity of the DHA-dFdC and dFdC alone are not identical, but more experiments need to be carried out to understand how DHA-dFdC causes cytotoxicity to tumor cells.

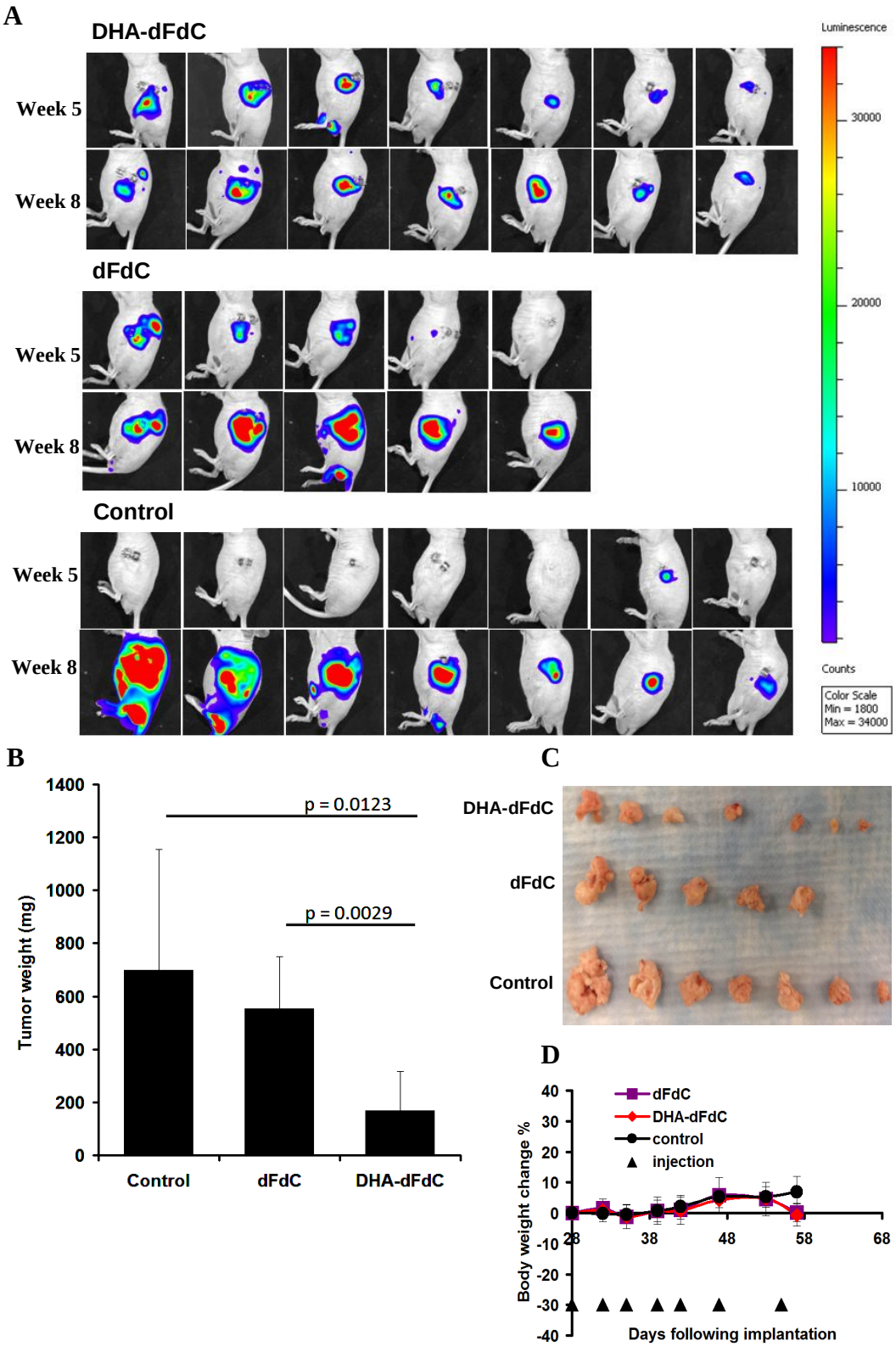
A
DHA-dFdC
Week 5
Week 8
dFdC
Week 5
Week 8
Control
Week 5
Week 8
Luminescence
30000
20000
10000
Counts
Color Scale
Min = 1800
Max = 34000
B
Tumor weight (mg)
1400
1200
1000
800
600
400
200
0
p = 0.0123
p = 0.0029
Control
dFdC
DHA-dFdC
C
DHA-dFdC
dFdC
Control
D
Body weight change %
40
30
20
10
0
-10
-20
-30
-40
dFdC
DHA-dFdC
control
injection
28
38
48
58
68
Days following implantation

Figure: 3.12

Figure 3.12. Antitumor activity of DHA-dFdC against Panc-1-Luc human pancreatic tumors implanted orthotopically in the pancreases of athymic nude male mice. Briefly, mice were anesthetized by isoflurane, and their pancreases were exposed following surgical incision. Panc-1-Luc cells (1×10^6 cells/mouse) were injected in the pancreas; the peritoneal membrane and skin were closed by sutures and clips, respectively. 4 weeks after tumor implantation, mice were randomized, and dosed with DHA-dFdC (50 mg/kg, in Tween 80/ethanol/aqueous mannitol solution vehicle) or dFdC (26.1 mg/kg, in aqueous mannitol solution). Treatments were given by i.p. injection as twice a week. (A) IVIS images of tumors in the 5^{th} week and 8^{th} week after the tumor implantation. (B) Tumor weights at the end of the study. (C) Photos of tumors at the end of the study. (D) Mouse body weight change during treatments. Data shown in B and D are means ± S.D. (n = 5-7).

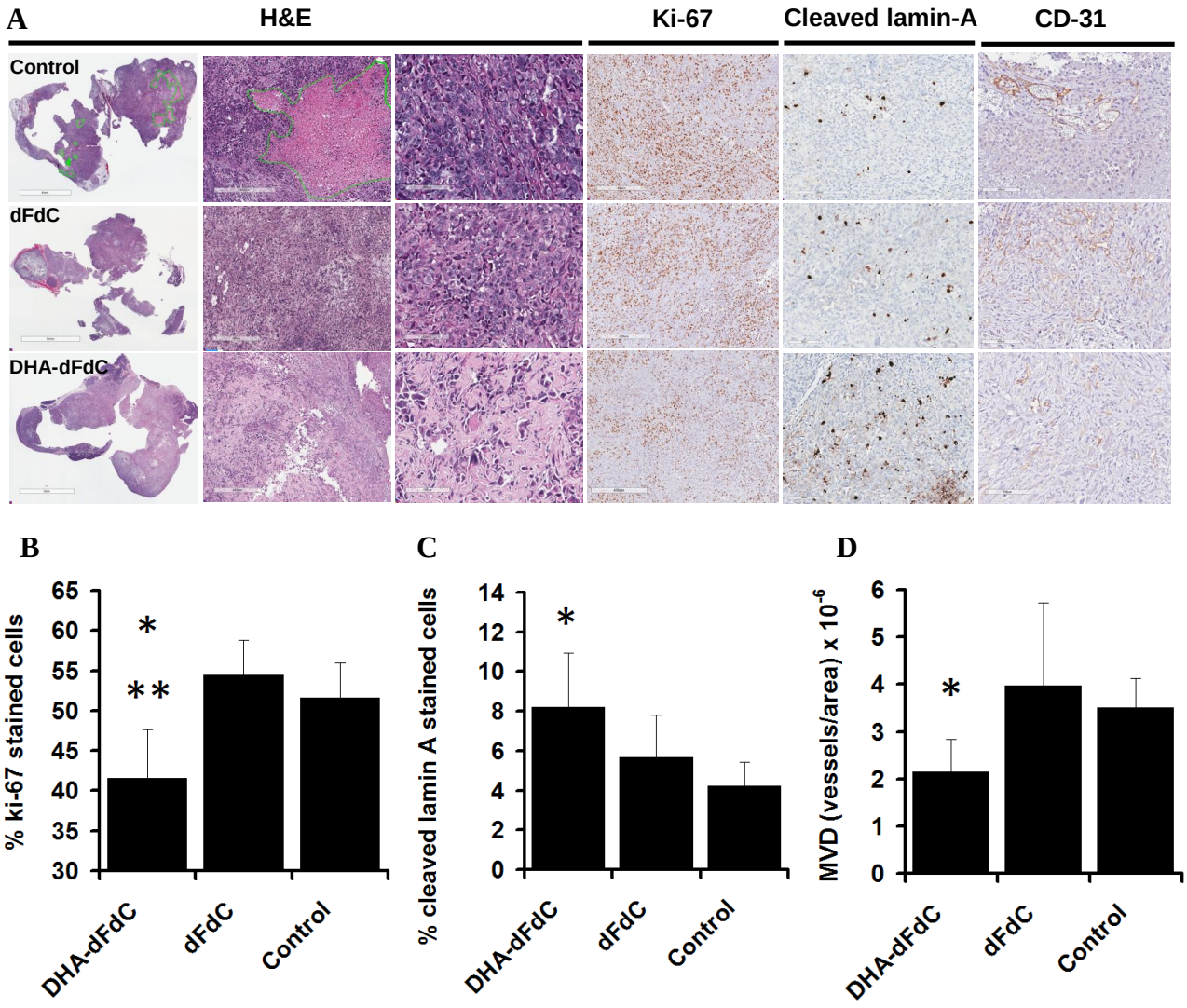
A
H&E
Ki-67
Cleaved lamin-A
CD-31
Control
dFdC
DHA-dFdC
B
% ki-67 stained cells
65
60
55
50
45
40
35
30
*
**
DHA-dFdC
dFdC
Control
C
% cleaved lamin A stained cells
14
12
10
8
6
4
2
0
*
DHA-dFdC
dFdC
Control
D
MVD (vessels/area) x 10-6
6
5
4
3
2
1
0
*
DHA-dFdC
dFdC
Control

Figure: 3.13

Figure 3.13. Histological and immunohistochemical evaluation of Panc-1-Luc orthotopically-implanted tumors. (A) Representative histological images of tumors from nude mice that were treated with DHA-dFdC or dFdC, after the tumor tissues were stained with H&E, anti-Ki-67, anti-cleaved lamin A, or anti-CD31 antibodies. (B) Percentage of Ki-67 positively-stained cells. (C) Percent of cleaved lamin A positively-stained cells. (D) The micro-vessel density (MVD) values in tumors determined after anti-CD-31 staining, * $p < 0.05$ against control, ** $p < 0.05$ against dFdC.

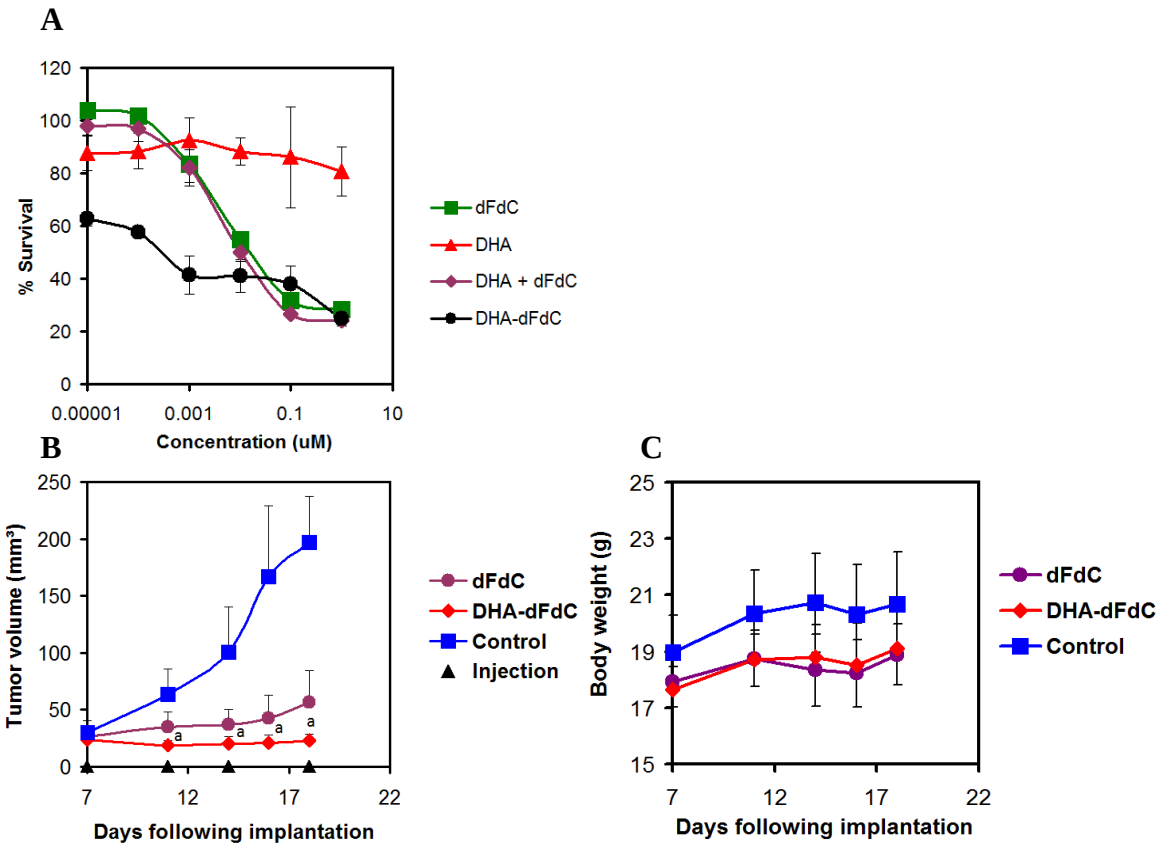
A
120
100
80
60
40
20
0
% Survival
0.00001
0.001
0.1
10
Concentration (uM)
dFdC
DHA
DHA + dFdC
DHA-dFdC
B
250
200
150
100
50
0
Tumor volume (mm³)
7
12
17
22
Days following implantation
a
a
a
a
dFdC
DHA-dFdC
Control
Injection
C
25
23
21
19
17
15
Body weight (g)
7
12
17
22
Days following implantation
dFdC
DHA-dFdC
Control

Figure: 3.14

Figure 3.14: Antitumor activity of DHA-dFdC against TC-1 cells in culture and in vivo in tumor model in C57BL/6 mice. (A) Anti-proliferative activity of DHA-dFdC and molar equivalent concentrations of other treatments against TC-1 murine lung cancer cells after 24 h. (B) TC-1 tumor growth curves following treatment with DHA-dFdC or dFdC. TC-1 tumor cells were subcutaneously implanted (500,000 cells/mouse) in the right flank of female mice, and treatment started in the 7^{th} day following tumor implantation. Mice received either DHA-dFdC in Tween 80/ethanol/mannitol aqueous solution vehicle (50 mg/kg), dFdC in sterile aqueous 5% mannitol solution (26.1 mg/kg), or were kept untreated. Treatments were given by i.p. injection as twice/week. (B) Mouse body weight during treatments. [a] $p < 0.05$, DHA-dFdC vs. other groups. n = 5-6, data are means ± SD).

Another unexpected finding from this present study is the high accumulation of DHA-dFdC in pancreas after i.v. injection into mice (Figures 3.7C and 3.8). The relatively high distribution of DHA-dFdC in pancreas was observed in both healthy mice (BALB/c) and tumor-bearing mice (C57BL/6 mice with TC-1 tumors and with orthotopic M-wnt mammary tumors, data not shown). The high accumulation of DHA-dFdC in the pancreas is likely related to the slow elimination of the DHA-dFdC from pancreatic tissues (Figure 3.8), but the reason behind the slow pancreatic elimination remains unknown. Fukui et al. previously reported that when a diet supplemented with fish oil was given to nude mice for 2 weeks (orally), exceptionally high levels of eicosapentanoic acid (omega-3 fatty acid, EPA) were detected in the pancreas of the mice, compared to control mice that received diet supplemented with corn oil [340]. Significantly higher pancreatic accumulation of DHA was also reported in the previously mentioned experiment, when compared to control mice, but the difference in DHA levels between fish oil-fed and corn-oil fed mice was much less pronounced than that reported with EPA (about 1.5 times compared to 5 times, respectively) [340]. Li et al. reported the synthesis of a DHA and dFdC conjugate, although no data were presented to demonstrate that the DHA was conjugated to the 4-NH2 group of dFdC [341]. Nonetheless, the authors showed that DHA seemed to help target dFdC to cells whose membrane is rich in phosphatidylethanolamine (PE) [341]. The unexpected high accumulation of DHA-dFdC in pancreas prompted the evaluation of its antitumor activity against pancreatic tumors in mouse models, and data in Figures 3.9-3.2.13) clearly showed that DHA-dFdC, at a dosing regimen that did not cause any observed side effects, effectively inhibit pancreatic

tumor growth in mice with spontaneously developed PDAC and with subcutaneous or orthotopic Panc-1 human pancreatic tumor xenografts. Panc-1 tumor cells are known to be resistant to dFdC, which explains why dFdC at the dosing regimen used did not significantly inhibit Panc-1 tumor growth (Figures 3.11, and 3.12). The potent cytotoxicity of DHA-dFdC against pancreatic tumor cells and their high accumulation in pancreas may partially explain its observed potent antitumor activity against orthotopic Panc-1 tumors and PDAC that were spontaneously developed in the Kras-ink4A$^{+/-}$ transgenic mice. Additionally, data from the NCI-60 human tumor cell line screening clearly showed that DHA-dFdC has potent broad spectrum activity against tumor cells. Thus, it is not unreasonable to expect it to show potent antitumor activity against other tumors such as renal cell carcinoma and leukemia. In fact, DHA-dFdC was significantly more effective than the molar equivalent dose of dFdC in inhibiting the growth of subcutaneously implanted mouse TC-1 lung cancer cells (Figure 3.14). Finally, the data in the present study clearly illustrated that covalently conjugating two pharmacologically active compounds together can generate a new compound with unexpected pharmacokinetics and efficacy profiles. Figure 3.4 reveals that the spectrum of antiproliferative activity of dFdC is completely different than that of dFdC, confirming the development of a new chemical entity.

3.5 Conclusion

In this report, a novel dFdC derivative (DHA-dFdC) was obtained and purified by conjugating DHA to the 4-(N) site of dFdC backbone. DHA-dFdC showed superior anti-proliferative and cytotoxic activity compared to dFdC or to a molar equivalent dose of dFdC + DHA in mixture. Improved antitumor activity was also found in nude mice with either subcutaneous or orthotopic Panc-1-Luc human pancreatic tumor xenografts, when compared to dFdC. Preliminary biodistribution study revealed that the drug favorably accumulates in the pancreas as the major organ of distribution following normalization to tissue weight. This trend may contribute to the enhanced antitumor activity of DHA-dFdC against pancreatic cancer.

Chapter 4

General Conclusion

In this dissertation, some of the most commonly encountered problems and drawbacks of currently available chemotherapeutic agents were addressed and were successfully overcome utilizing pharmaceutical technology approaches. In one example, in order to avoid the undesirable untoward effects related to either the excipient or the chemotherapeutic itself, a docetaxel- (DCX-) loaded solid lipid nanoparticle formulation (DCX-SLNs) was developed and evaluated as an alternative to the current docetaxel formulation that contains Tween 80 among other excipients. A long circulating, Tween 80-free nanoparticle formulation of DCX will not only avoid Tween 80-related side effects, but also is expected to accumulate more DCX in the tumor due to the enhanced permeation and retention (EPR) effect.

Instead of Tween 80, with which hypersensitivity reactions that can be severe are associated, mixtures of triglycerides and phospholipids were used to formulate DCX-SLNs. Various triglycerides with different carbon chain lengths were evaluated as the core material for the SLNs, while polyethylene glycol-modified (PEGylated) phospholipids were used to stabilize the nanoparticle formulations and to render their surfaces hydrophilic to achieve long circulation time. Trimyristin-based formulation was found to be more stable and able to release docetaxel at a relatively slower rate, and was chosen for further evaluation. Anti-proliferative activity of the DCX-SLNs was found to be higher than the conventional Tween 80-based DCX formulation, with IC_{50} values of

0.01, .0056, and 0.06 μM in MDA-MB-231, M-Wnt, and TC-1 cell lines, respectively, compared to 0.017, 0.011,and 0.113 μM with conventional DCX formulation. This higher anti-proliferative activity was found to be associated with significantly higher apoptotic activity as well. The overall better anti-cancer activity in cell culture obtained with DCX-SLNs may be related to the slow release of DCX from the formulation, with can prolong the exposure time of the cells to DCX. *In vivo* evaluation of DCX-SLNs in murine lung cancer tumor model in mice was carried out and it was found that DCX-SLNs have significantly more effective than the conventional DCX formulation to slow down tumor progress. This effect can be explained by the improved retention of DCX in tumors when DCX-SLNs were injected compared to the conventional DCX formulation. DCX-SLNs seemed to have a more favorable safety profile as relatively less drug was found in vital organs following injection of DCX-SLNs compared to conventional DCX formulation. In general, it can be concluded that a new PEGylated nanoparticle-based DCX formulation appears to be a better alternative to the currently available DCX formulation due to improved antitumor activity and apparent favorable safety profile.

On the other hand, gemcitabine HCl (dFdC) is one of the standard treatments for advanced pancreatic cancer, which is a fatal disease in most cases. Several drawbacks are associated with dFdC, including extensive metabolism, mainly via deamination, to yield inactive metabolites, in addition to the emergence of various resistance mechanisms within the cancer cells.

In this dissertation, the omega-3 unsaturated fatty acid docosahexaenoic acid (DHA) was covalently conjugated to the 4-N site of dFdC in order to achieve improved

effect via the protection of the vulnerable amine group of dFdC against extensive deamination and also to take advantage of the reported antitumor activity of DHA. The new conjugate (DHA-dFdC) was successfully synthesized and its structure was confirmed by means of NMR, mass spectrometry, and LC/MS. X-ray diffraction pattern revealed that major crystallization peaks of dFdC completely disappeared, while the melting point of the conjugate was found to be around 96º C as indicated by differential scanning calorimetry (DSC). Cellular uptake of DHA-dFdC was several folds higher than that of dFdC. Surprisingly, it was also found that the conjugate accumulates in the pancreas of mice following i.v. injection at higher levels compared with dFdC. When the conjugate was evaluated against dFdC-resistant human pancreatic tumors (Panc-1) implanted subcutaneously in nude mice, stronger antitumor activity was achieved, compared to dFdC alone, DHA alone, or a molar equivalent mixture of the two. Similar results were obtained when DHA-dFdC was injected (50 mg/kg, twice a week) in nude mice with orthotopic human pancreatic tumors compared to dFdC. Overall, chemical conjugation of a natural unsaturated fatty acid with a potential anticancer activity to the terminal amine group of dFdC yielded a conjugate with significantly improved antitumor activity compared to dFdC, in *in vitro* and *in vivo* models.

Appendix A

The effect of microneedles on the skin permeability and antitumor activity of topical 5-fluorouracil [3]

A.1 Introduction

Fluorouracil (5-FU) is an anti-metabolite that is used in the treatment of various types of cancers, including breast, head and neck, and colorectal cancer [342;343]. The fluorinated pyrimidine analog is available in topical formulations, which were approved by the United States Food and Drug Administration (FDA) to treat actinic keratosis (non-cancerous) and superficial basal cell carcinoma (BCC) [344;345]. Approved topical products include 5-FU solutions (e.g., Fluoroplex 1% 5-FU solution, Allergan, Inc., Irvine, CA, USA), creams (e.g., Efudex, Valeant Pharmaceuticals, Bridgewater, NJ, USA), and a 0.5% microsphere-based cream (Carac, Valeant Pharmaceuticals). Other reported clinical applications of topical 5-FU include the treatment of nail psoriasis [344;346], cholesteatoma [347], lentigo maligna [348], and some premalignant ophthalmic conditions [349]. Topical treatment with 5-FU, when applicable, is usually preferred to surgical removal of affected lesions for cosmetic reasons, especially for multiple lesions and/or facial lesions [350]. Unfortunately, the skin permeability of topically applied 5-FU is poor [351-353], likely due to its hydrophilic nature (LogP = -0.89) [354].

---

[3] This chapter is based on "*Youssef W. Naguib*[*]*, Amit Kumar*[*]*, and Zhengrong Cui,* ***Acta Pharmaceutica Sinica B****, 2014. 4 (1): 94-99"*

[*] *Contributed equally*

The use of the topical 5-FU in BCC is only limited to superficial BCC, and it is not recommended for invasive forms of BCC [345;355]. This is based on a study by Mohs *et al.*, who reported that topical application of 5-FU in invasive BCCs can mislead clinicians by showing superficial improvement, while the deeper parts of the cancerous lesions continue to grow unnoticed [355].

Several approaches to improve the skin permeation of topical 5-FU have been evaluated with different degrees of success. For example, Paolino *et al*. described the formulation of 5-FU-loaded bola-surfactant-based niosomes to improve the percutaneous permeation and antitumor activity of 5-FU [352]. The proposed niosomes exhibited an 8-fold increase in the percutaneous permeation of 5-FU through human skin, as compared to 5-FU in an aqueous solution. The 5-FU niosomes were significantly more cytotoxic against SKMEL-28 human melanoma cells in culture than 5-FU solution, which was attributed to the improved cellular uptake of 5-FU in the niosomes [352]. Other researchers reported the use of penetration enhancers such as Azone, isopropyl myristate, and lauryl alcohol [353], or the use of improved pharmaceutical formulation technologies (e.g., microemulsions [351] and nanogels [354]), to increase the percutaneous permeation of 5-FU. Physical methods to improve the permeability of 5-FU have also been evaluated. For example, Fang *et al*. studied the effect of a series of physical methods, namely iontophoresis, electroporation, and erbium:YAG (erbium:yttrium-aluminum-garnet) laser, and their combination, on the permeability of 5-FU [356]. Both iontophoresis and electroporation significantly enhanced the percutaneous permeability of 5-FU, but the controlled removal of the stratum corneum by

erbium:YAG laser was most effective [356], confirming that it is the stratum corneum that limits the skin permeability of 5-FU. Finally, Meidan *et al*. found that ultrasound unexpectedly lowered the permeability of 5-FU through whole rat skin; an effect that was attributed to the back-diffusion of 5-FU to the ultrasonic coupling gel filled in the donor compartment [357].

Microneedle technology has been successfully applied to improve the skin permeability of small molecules, macromolecules, vaccines, and even nanoparticles, by creating an array of micro-sized holes in the stratum corneum of skin [354;358;358-364]. In the present study, the feasibility of using microneedles to improve the skin permeability of 5-FU was tested *in vitro* using mouse skin mounted on Franz diffusion apparatus. In addition, the feasibility of using microneedles to improve the *in vivo* antitumor activity of 5-FU was tested by comparing the ability of an FDA-approved topical 5-FU cream in inhibiting the growth of subcutaneously implanted B16-F10 tumors in mice. The 5-FU cream was applied on the mouse skin area where the tumor cells were implanted, with or without pretreatment (of the skin area) with a microneedle roller. Topical 5-FU is not approved for melanoma treatment, but 5-FU was reported to be effective against melanoma cells in culture and in animal models [360;361]. The B16-F10 tumor cells are implanted subcutaneously in mice, which allows us to indirectly evaluate the *in vivo* permeation of 5-FU across mouse skin as well.

A.2 Materials and methods

A.2.1 Materials

The Dermaroller® microneedle roller was kindly provided by Cynergy, LLC (Carson City, NV, USA). There are 192 needles (500 μm in length, 50 μm in base diameter) on the roller. The topical 5-FU cream (5%) was from Taro Pharmaceuticals USA, Inc. (Hawthorne, NY, USA). Phosphate buffered saline (PBS, pH 7.4), cell culture medium, and antibiotics were from Invitrogen (Life Technologies, Carlsbad, CA, USA). MTT (3-(4,5-dimethylthiazol-2-yl)-2,5-diphenyltetrazolium bromide) and 5-FU were from Sigma-Aldrich (St. Louis, MO, USA).

A.2.2 *In vitro* cytotoxicity assay

B16-F10 murine melanoma cells were from American Type Culture Collection (Manassas, VA, USA) and maintained in Dulbecco's modified eagle medium (DMEM) with 10% (v/v) fetal bovine serum, 10 U/ml of penicillin, and 100 μg/ml of streptomycin. Cells (2000/well) were seeded in 96-well plates and incubated overnight at 37°C, 5% CO_2. Cells were then incubated in the presence of various concentrations of 5-FU in PBS solution (pH 7.4) for 24 h or 48 h. Cell viability was determined using an MTT assay following the manufacturer's instructions. The formed formazan crystals were dissolved in 100 μl of dimethyl sulfoxide, and the absorbance of the resultant solution was measured at 570 nm and 630 nm using a BioTek Synergy™ HT Multi-Mode Microplate Reader (Winooski, VT, USA).

A.2.3 *In vitro* permeation of 5-FU in solution through mouse skin

In vitro permeation assay using Franz diffusion cells was completed as previously described [360]. Full thickness dorsal skin from C57BL/6 mice was used in the permeation study. Hair was carefully trimmed using an electric clipper 24 h before the collection of the skin. The harvested skins were stored at -20^{o}C and used within one month. On the day when the permeability study was performed, the skin was also treated with the Veet® hair removal cream for 5 min and washed three times with water. The skin was then mounted onto the Franz diffusion cells (PermeGear, Inc., Hellertown, PA, USA), with the epidermis side facing upward. The receiver compartment contained 5 ml of PBS (pH 7.4, 10 mM) and was maintained at 37^{o}C (Haake SC 100 Water Circulator, ThermoScientific, Wellington, NH, USA). The diffusion area of the skin was 0.64 cm^{2}. The donor compartment was loaded with 400 µg of 5-FU in 400 µl PBS (pH 7.4, 10 mM) and covered with parafilm to prevent evaporation. To test the effect of treatment with microneedles on the permeation of 5-FU through the skin, the skin samples were also treated with a Dermaroller® microneedle roller as previously described before it was mounted onto the Franz diffusion cells [362]. Briefly, the skin sample was placed onto the flat surface of a balance, and the microneedle roller was rolled in 4 perpendicular lines over the skin surface, 5 times each for a total of 20 times, with an applying pressure of 600-800 g, which was constantly measured using the balance. At pre-determined time points (1, 2, 3, 6, and 18 h), samples (100 µl) were withdrawn from the receiver compartment and immediately replenished with fresh medium. The samples were

analyzed using HPLC. Chromatography was carried out with an Agilent Technologies 1260 Infinity HPLC workstation with an Agilent ZORBAX Eclipse Plus C18 column (5 µm, 4.6 x 150 mm) using a potassium phosphate buffer (40 mM, pH 7.0) as the mobile phase. The flow rate was 0.5 ml/min. The detector wavelength was 260 nm.

A.2.4 Animal study

Animal study was carried out following the US National Research Council guide for the care and use of laboratory animals. The animal protocol was approved by the Institutional Animal Care and Use Committee at The University of Texas at Austin. Female C57BL/6 mice (8-10 weeks) were from Charles River Laboratories (Wilmington, MA, USA). Hair in the lower dorsal skin of anesthetized mice was trimmed using an electric clipper. B16-F10 murine melanoma cells (100,000 cells per mouse) in 100 µl DMEM medium were injected subcutaneously in the hair-trimmed area on day 0. On day 9, mice were divided into 5 groups (5-6 mice per group) and treated as following: mice in the 5-FU cream group were treated with the 5-FU cream (100 mg of cream per mouse) on the area where the tumor cells were injected using a spatula, once daily for 8 consecutive days; mice in the MN + cream group were treated similarly, except that the application area was pretreated with the Dermaroller® microneedle roller (MN); mice in the I.V. 5-FU group were injected with 5-FU in sterile PBS intravenously via the tail vein (50 mg/kg body weight) on days 9 and 15. Control groups include tumor-bearing mice that were left untreated, or tumor-bearing mice that were treated with the microneedle roller in the skin area where the tumor cells were injected, but without further treatment with 5-

FU (i.e., MN group). To treat the mice with the microneedle roller, mice were placed onto the flat surface of a balance, and the microneedle roller was rolled over the skin area where the tumor cells were injected, 10 times parallel to the mouse length, with an applying pressure of around 400 g, which was measured using the balance. Tumor growth was monitored, and tumor size measured using a digital caliper. Tumor volume was calculated based on the following equation: tumor volume (mm^3) = (length x width x width)/2. On the last day of the study (day 17), mice were euthanized, and tumor tissues were collected and weighed.

A.2.5 Histology and immunohistochemistry

Tumor tissues were fixed with a buffered formalin (10%) solution for 48 h and then transferred to 70% ethanol until sections were prepared, following paraffin embedding. The sections were stained using hematoxylin-eosin (H&E) or anti-CD31 antibody (an angiogenesis marker, Abcam, Cambridge, MA, USA) in the Histology and Tissue Processing Facility in the Dell Pediatric Research Institute at the University of Texas at Austin. Slides were scanned, and images were taken using the ScanScope XT (Aperio Technologies, Vista, CA, USA).

A.2.6 Statistical analyses

Statistical analyses were completed by performing analysis of variance followed by Fisher's protected least significant difference procedure. A p-value of ≤ 0.05 (two-tail) was considered significant.

A.3 Results and discussion

Topical 5-FU products are available on the market to treat keratosis and superficial BCC. The poor skin permeation of 5-FU limits its application against various other cancerous and non-cancerous conditions. Microneedles have been successfully applied to improve the skin permeability of large and small molecules, and even nanoparticles, by creating micro-sized holes in the stratum corneum of skin [358-362]. The feasibility of using microneedles to improve the skin permeability of 5-FU was tested in the present study by pretreating skin with a microneedle roller that has solid microneedles (500 μm in length, 50 μm in base diameter) on it. The effect of pretreatment of mouse skin with microneedles on the diffusion of 5-FU in solution through full thickness mouse skin was initially evaluated *in vitro* using a Franz diffusion apparatus. As expected, the permeation of 5-FU through intact full thickness mouse skin was limited, with a flux of 8.93 ± 4.55 μg/cm^2/h (Figure A.1). Previously, Fang *et al*. reported a flux value of 1.5-2 μg/cm^2/h (at pH 5.0) for the diffusion of 5-FU across full thickness nude mouse skin [15]. However, the permeability of 5-FU through mouse skin that was pretreated with microneedles was significantly higher, with a flux of 39.75 ± 18.50 μg/cm^2/h, which is 4.5-fold larger than the flux of 5-FU through intact mouse skin ($p < 0.05$). Clearly, pretreatment of mouse skin with solid microneedles significantly increased the permeability of 5-FU through the skin.

To test whether pretreatment of mouse skin with microneedles can improve the antitumor activity of topical 5-FU by increasing its skin permeability, the ability of a topical 5-FU cream to inhibit the growth of mouse B16-F10 melanoma cells implanted

subcutaneously in the application area in mice was evaluated; the area where the 5-FU cream was applied was pretreated with the microneedle roller every time before the application of the 5-FU cream. Although 5-FU is not approved for melanoma, it was previously shown to be cytotoxic against human and murine melanoma cells [354;363;364]. Our own data also confirmed that 5-FU inhibited the growth of the B16-F10 mouse melanoma cells in culture (Figure A.2). B16-F10 mouse melanoma cells were subcutaneously implanted in the rear dorsal area of female C57BL/6 mice. When the tumor sizes reached 20-40 mm^3 (9 days following implantation), mice were treated with the 5-FU cream (5%) topically on the skin area where the tumor cells were implanted. As shown in Figure A.3A, B16-F10 tumors grew aggressively if left untreated. Topical treatment with 5-FU cream significantly inhibited the tumor growth (Figure A.3A). However, the 5-FU cream was significantly more effective in inhibiting the tumor growth when the skin area where the 5-FU cream was applied was pretreated with the microneedle roller (Figure A.3A). At the end of the study, mice were euthanized to collect tumor tissues (Figure A.3B). The average weight of tumors in mice that were topically treated with the 5-FU cream without pretreatment with microneedles was significantly lower than in mice that were left untreated, but was significantly larger than in mice that were treated with microneedles before the application of the 5-FU cream (Figure A.3C). In fact, the growth of tumors in mice that were treated with the topical 5-FU cream following pretreatment of the skin area with the microneedle roller was completely inhibited (Figs. 3A-C). The experiment was repeated with twice daily applications of 5-FU cream as well, and similar results were obtained (data not shown).

The antitumor activity of the topical 5-FU following pretreatment with microneedles was not simply due to the mechanical activity of applying the microneedle roller daily on the mouse skin area where the tumor cells were subcutaneously injected, because treatment with the microneedle roller alone without the 5-FU cream did not show any significant effect on the growth of the B16-F10 tumors (Figs. 3A-C). The weights of the mice were also monitored during the treatment period, and it was found that the weights of mice that were treated with the 5-FU cream following pretreatment with microneedles, once daily for 8 consecutive days, did not significantly change (Figure A.3D), suggesting that the practice of applying 5-FU cream on a skin area pretreated with microneedles is potentially safe.

Finally, the tumor tissues were collected from mice and examined microscopically. H&E staining revealed that except in mice that were treated with microneedles prior to the application of the 5-FU cream (i.e., the MN + 5-FU cream group), tumors in all other groups were large (Figure A.4A), with densely packed cells and scattered necrotic areas (Figure A.4B). On the contrary, tumors in mice that were treated with 5-FU cream after pretreatment with microneedles were smaller (Figure A.4A), and the tumor cells were loosely distributed with large intercellular spaces (Figure A.4B). Anti-CD31 staining (angiogenesis marker) also revealed that with the exception of tumors in mice in the MN + 5-FU cream group, tumors in mice from all other groups had well-developed vasculature (Figure A.4C).

Taken together, it is clear that the 5-FU cream was more effective when applied on a mouse skin area pretreated with microneedles than without microneedle

pretreatment in inhibiting the growth of the B16-F10 tumor cells subcutaneously implanted underneath the skin (Figure A.3), likely because pretreatment with microneedles enabled more 5-FU to permeate through the skin and reach the tumor cells in the subcutaneous space. Data in Figure A.1 clearly demonstrated that pretreatment of mouse skin with microneedles significantly increased the permeability of 5-FU through the skin. As mentioned earlier, topical 5-FU is approved by the FDA for the treatment of superficial BCC. BCC is developed from basal cells in basement membrane layer in the skin epidermis [365]. The data generated in the present study with the B16-F10 melanoma cells established in the subcutaneous space underneath the skin dermis layer may not accurately predict the effect of topical 5-FU applied on a skin area pretreated with microneedles on the growth of spontaneously developed BCC. However, in both cases, the 5-FU applied topically onto the skin needs to 'travel' across the stratum corneum layer before it can reach the live epidermis layer underneath the stratum corneum or the subcutaneous space. Data from previous studies showed that the stratum corneum layer is rate-limiting in the percutaneous absorption of 5-FU [356]. In addition, microneedles' ability to increase the skin permeability of molecules is mainly attributed to the micro-pores or holes created by them in the stratum corneum [360;361]. Therefore, the finding that pretreatment of a skin area with microneedles significantly enhanced the antitumor activity of topical 5-FU against the subcutaneously implanted mouse B16-F10 tumor cells may be exploited to improve the efficacy of topical 5-FU against human BCC in clinics, especially considering that microneedle rollers, including the one that was used in the present study (500 μm in needle length, 50 μm in based diameter), are already used

by humans for cosmetic purposes and dermatology therapy to stimulate collagen and elastin production [361;362;366]. Moreover, since the dermal permeability of 5-FU can be significantly increased by pretreatment with microneedles, it may become possible to evaluate this treatment strategy for transdermal systemic delivery of 5-FU to treat other cancers (e.g., breast, colorectal, pancreatic, and gastric cancers), against which intravenous 5-FU is currently approved.

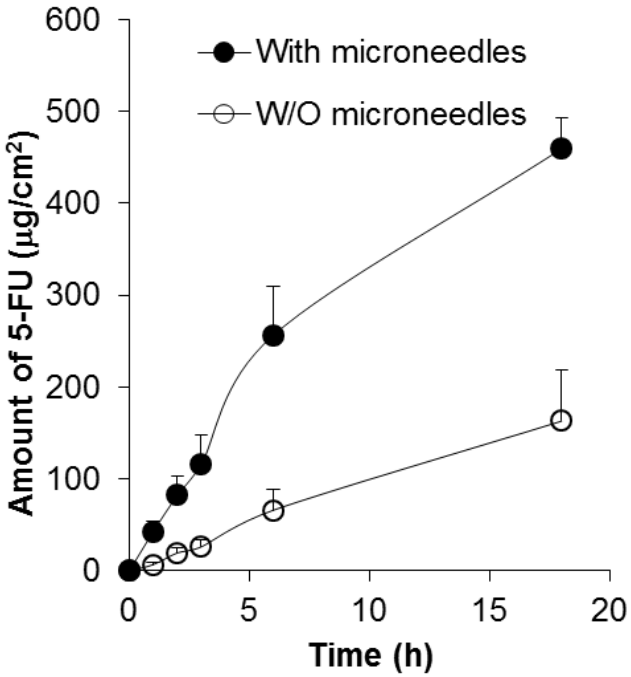
With microneedles
W/O microneedles
Amount of 5-FU (µg/cm²)
Time (h)
600
500
400
300
200
100
0
0
5
10
15
20

Figure: A.1

Figure A.1. The amounts of 5-FU in PBS solution diffused through full thickness mouse skin treated (●) or not treated (○) with microneedles as a function of time. Data shown are means ± S.E.M (n = 3). In all the time points tested, with the exception of 0 h, the values between the microneedle-treated and -untreated groups are significantly different ($p < 0.05$).

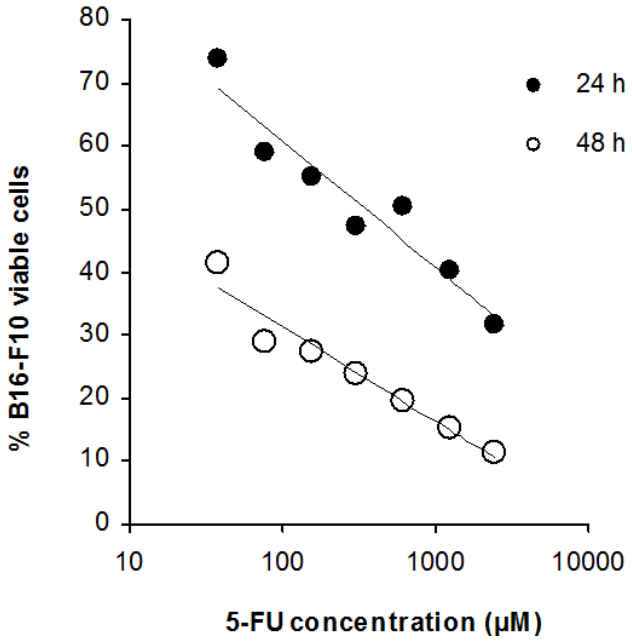
80
70
60
50
40
30
20
10
0
% B16-F10 viable cells
24 h
48 h
10
100
1000
10000
5-FU concentration (µM)

Figure: A.2

Figure A.2. *In vitro* cytotoxicity of 5-FU against B16-F10 mouse melanoma cells. Cells were incubated with various concentrations of 5-FU for 24 h (●) or 48 h (○), and cell viability was determined using an MTT assay. Data shown are means (n = 6). Standard deviations are not shown for clarity.

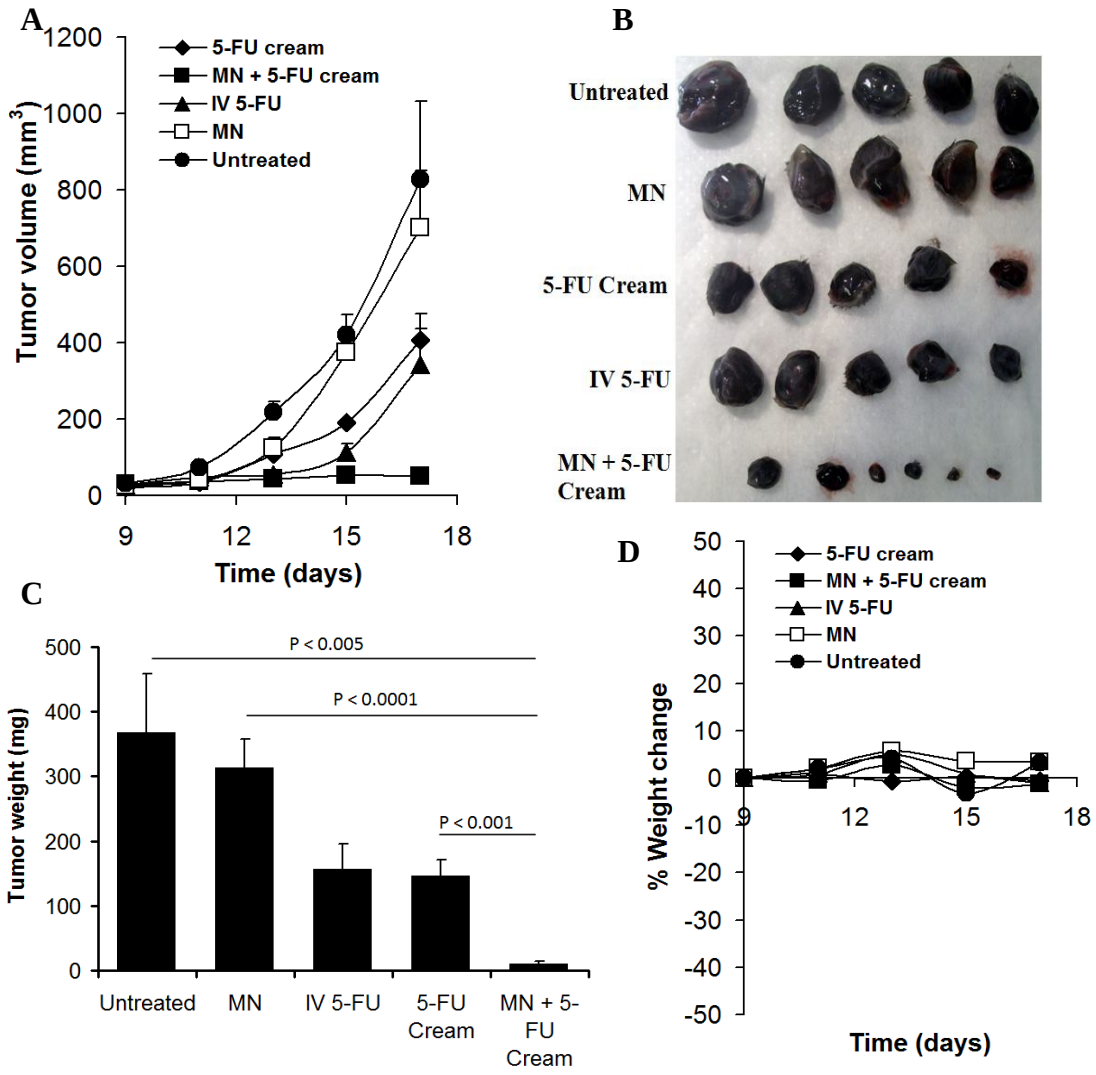
A
Tumor volume (mm3)
1200
1000
800
600
400
200
0
9
12
15
18
Time (days)
5-FU cream
MN + 5-FU cream
IV 5-FU
MN
Untreated
B
Untreated
MN
5-FU Cream
IV 5-FU
MN + 5-FU Cream
C
Tumor weight (mg)
500
400
300
200
100
0
P < 0.005
P < 0.0001
P < 0.001
Untreated
MN
IV 5-FU
5-FU Cream
MN + 5-FU Cream
D
% Weight change
50
40
30
20
10
0
-10
-20
-30
-40
-50
9
12
15
18
Time (days)
5-FU cream
MN + 5-FU cream
IV 5-FU
MN
Untreated

Figure: A.3

Figure A.3. **The antitumor activity of 5-FU cream applied on mice skins that were pre-treated with microneedles and below which B16-F10 melanoma tumors were implanted.** (**A**) The growth curves of B16-F10 tumors in C57BL/6 mice. (**B**) Digital photograph of tumors collected from mice at the end of the study. (**C**) The weights of tumors at the end of the study. (**D**) The changes in the body weight of B16-F10 tumor-bearing mice. C57BL/6 mice were subcutaneously injected with B16-F10 tumor cells on day 0. Starting on day 9, mice were randomly grouped (n = 5-6) and topically treated with 5-FU cream (5%), 100 mg daily for 8 consecutive days, on the skin area where the tumor cells were injected. The application area was pretreated (MN + 5-FU cream) or not (5-FU cream) with a microneedle roller before the application of the cream. As controls, mice were intravenously injected with 5-FU solution (I.V. 5-FU) on days 9 and 15. Other controls included tumor-bearing mice left untreated, or tumor-bearing mice treated with a microneedle roller in the skin area where the tumor cells were injected (i.e., MN). The asterisks (*) in A indicate that the values of the 5-FU cream group and the MN + 5-FU cream group are different on days 13, 15, and 17 ($p < 0.05$). Data shown in A and C are mean ± S.E.M (n = 5-6). Standard deviations are not shown in D for clarity (n = 5-6).

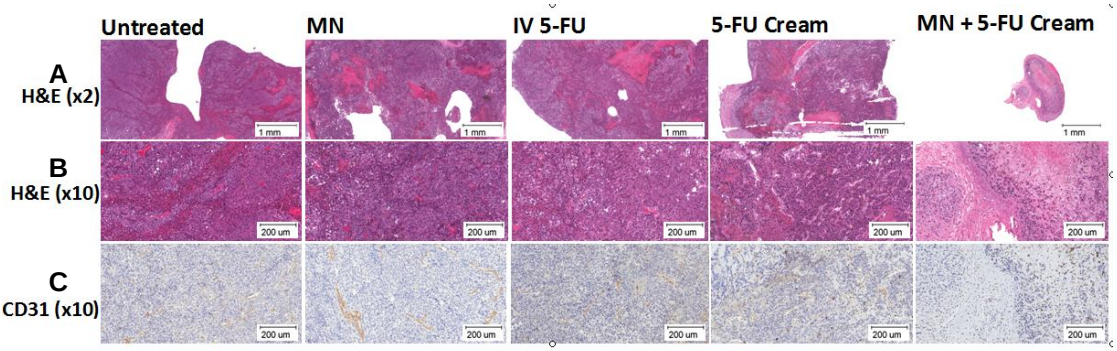
Untreated
MN
IV 5-FU
5-FU Cream
MN + 5-FU Cream
A
H&E (x2)
B
H&E (x10)
C
CD31 (x10)
1 mm
200 um

Figure: A.4

Figure A.4. **Histological and immunohistochemical evaluation of B16-F10 tumors following treatment of the tumor-bearing mice with either 5-FU cream with or without microneedle pretreatment, or with other controls.** Representative images of tumor tissues after H&E staining (**A**: x2, bar = 1mm, **B**: x10, bar = 200 μm) or anti-CD31 staining (**C**: x10, bar = 200 μm).

A.4 Conclusions

In this study, it was shown that the *in vitro* skin permeability and *in vivo* antitumor activity of topical 5-FU were significantly enhanced when the skin application area was pretreated with microneedles. Microneedle technology may be integrated into topical 5-FU therapy to improve the clinical outcomes.

Appendix B

Contribution of authors

Dr. Laura M. Lashinger (The University of Texas at Austin) substantially helped with some animal expriments mentioned in chapter 3, particularly Figure 3.12.

Ms. Audrey Rasmussen and Ms. Hannah Ruisi (The University of Texas at Austin) helped with some animal experiments mentioned in chapter 3. Ms. Ruisi and Dr. Tinashe Ruwona (The University of Texas at Austin) helped with genotyping of transgenic mice mentioned in chapter 3.

Dr. Xinran Li (The University of Texas at Austin) helped with TEM imaging in chapter 2.

Dr. Bertha Leticia Rodriguez (The University of Texas at Austin) contributed in Figures 3.5C, F, and G.

Dr. Dharmika P. Lansakara-P (the University of Texas at Austin) established the synthesis schemes of DHA-dFdC and ARA-dFdC (scheme 3.1), and also contributed with the cell culture experiments involving ARA-dFdC (Figure 3.5H).

Dr. Lan Peng (The University of Texas Southwestern Medical Center) helped with some of the information used in Table 3.3.

Dr. Amit Kumar (The University of Texas at Austin) helped with Figure A.2 and with Figure A.3.

Bibliography

1. Danhier F, Feron O, Preat V. To exploit the tumor microenvironment: Passive and active tumor targeting of nanocarriers for anti-cancer drug delivery. J Control Release 2010; 148(2):135-146.

2. Bangham AD, Standish MM, Watkins JC. Diffusion of univalent ions across the lamellae of swollen phospholipids. J Mol Biol 1965; 13(1):238-252.

3. Bangham AD, Horne RW. Negative staining of phospholipids and their structural modification by surface-active agents as observed in the electron microscope. Journal of Molecular Biology 1964; 8(5):660-IN10.

4. Haley B, Frenkel E. Nanoparticles for drug delivery in cancer treatment. Urol Oncol 2008; 26(1):57-64.

5. Rodriguez BL, Li X, Kiguchi K, DiGiovanni J, Unger EC, Cui Z. Control of solid tumor growth in mice using EGF receptor-targeted RNA replicase-based plasmid DNA. Nanomedicine (Lond) 2012; 7(4):475-491.

6. Alexis F, Pridgen EM, Langer R, Farokhzad OC. Nanoparticle technologies for cancer therapy. Handb Exp Pharmacol 2010;(197):55-86.

7. Torchilin VP. Recent advances with liposomes as pharmaceutical carriers. Nat Rev Drug Discov 2005; 4(2):145-160.

8. Arias JL. Liposomes in drug delivery: a patent review (2. Expert Opin Ther Pat 2013; 23(11):1399-1414.

9. Immordino ML, Dosio F, Cattel L. Stealth liposomes: review of the basic science, rationale, and clinical applications, existing and potential. Int J Nanomedicine 2006; 1(3):297-315.

10. Klibanov AL, Maruyama K, Torchilin VP, Huang L. Amphipathic polyethyleneglycols effectively prolong the circulation time of liposomes. FEBS Lett 1990; 268(1):235-237.

11. Banerjee R, Tyagi P, Li S, Huang L. Anisamide-targeted stealth liposomes: a potent carrier for targeting doxorubicin to human prostate cancer cells. Int J Cancer 2004; 112(4):693-700.

12. Li SD, Huang L. Targeted delivery of antisense oligodeoxynucleotide and small interference RNA into lung cancer cells. Mol Pharm 2006; 3(5):579-588.

13. Rodriguez BL, Blando JM, Lansakara P, Kiguchi Y, DiGiovanni J, Cui Z. Antitumor activity of tumor-targeted RNA replicase-based plasmid that expresses interleukin-2 in a murine melanoma model. Mol Pharm 2013; 10(6):2404-2415.

14. Raju A, Muthu MS, Feng SS. Trastuzumab-conjugated vitamin E TPGS liposomes for sustained and targeted delivery of docetaxel. Expert Opin Drug Deliv 2013; 10(6):747-760.

15. Gao J, Sun J, Li H, Liu W, Zhang Y, Li B et al. Lyophilized HER2-specific PEGylated immunoliposomes for active siRNA gene silencing. Biomaterials 2010; 31(9):2655-2664.

16. Wu XS, Wang N. Synthesis, characterization, biodegradation, and drug delivery application of biodegradable lactic/glycolic acid polymers. Part II: biodegradation. J Biomater Sci Polym Ed 2001; 12(1):21-34.

17. Wu XS. Synthesis, characterization, biodegradation, and drug delivery application of biodegradable lactic/glycolic acid polymers: Part III. Drug delivery application. Artif Cells Blood Substit Immobil Biotechnol 2004; 32(4):575-591.

18. Nair LS, Laurencin CT. Biodegradable polymers as biomaterials. Progress in Polymer Science 2007; 32(8ΓÇô9):762-798.

19. Gopferich A. Mechanisms of polymer degradation and erosion. Biomaterials 1996; 17(2):103-114.

20. Chandra R, Rustgi R. Biodegradable polymers. Progress in Polymer Science 1998; 23(7):1273-1335.

21. von BF, Schedl L, Gopferich A. Why degradable polymers undergo surface erosion or bulk erosion. Biomaterials 2002; 23(21):4221-4231.

22. Gref R, Minamitake Y, Peracchia MT, Trubetskoy V, Torchilin V, Langer R. Biodegradable long-circulating polymeric nanospheres. Science 1994; 263(5153):1600-1603.

23. Pradhan R, Poudel BK, Ramasamy T, Choi HG, Yong CS, Kim JO. Docetaxel-loaded polylactic acid-co-glycolic acid nanoparticles: formulation, physicochemical characterization and cytotoxicity studies. J Nanosci Nanotechnol 2013; 13(8):5948-5956.

24. Jagani HV, Josyula VR, Palanimuthu VR, Hariharapura RC, Gang SS. Improvement of therapeutic efficacy of PLGA nanoformulation of siRNA targeting anti-apoptotic Bcl-2 through chitosan coating. Eur J Pharm Sci 2013; 48(4-5):611-618.

25. Pinto RC, Neufeld RJ, Ribeiro AJ, Veiga F. Nanoencapsulation I. Methods for preparation of drug-loaded polymeric nanoparticles. Nanomedicine 2006; 2(1):8-21.

26. Beck-Broichsitter M, Rytting E, Lebhardt T, Wang X, Kissel T. Preparation of nanoparticles by solvent displacement for drug delivery: a shift in the "ouzo region" upon drug loading. Eur J Pharm Sci 2010; 41(2):244-253.

27. Jensen DM, Cun D, Maltesen MJ, Frokjaer S, Nielsen HM, Foged C. Spray drying of siRNA-containing PLGA nanoparticles intended for inhalation. J Control Release 2010; 142(1):138-145.

28. Byrappa K, Ohara S, Adschiri T. Nanoparticles synthesis using supercritical fluid technology - towards biomedical applications. Adv Drug Deliv Rev 2008; 60(3):299-327.

29. Perry JL, Herlihy KP, Napier ME, Desimone JM. PRINT: a novel platform toward shape and size specific nanoparticle theranostics. Acc Chem Res 2011; 44(10):990-998.

30. Kam KR, Desai TA. Nano- and microfabrication for overcoming drug delivery challenges. J Mater Chem B Mater Biol Med 2013; 1(14):1878-1884.

31. Yoo JW, Doshi N, Mitragotri S. Adaptive micro and nanoparticles: temporal control over carrier properties to facilitate drug delivery. Adv Drug Deliv Rev 2011; 63(14-15):1247-1256.

32. Saxena V, Hussain MD. Poloxamer 407/TPGS mixed micelles for delivery of gambogic acid to breast and multidrug-resistant cancer. Int J Nanomedicine 2012; 7:713-721.

33. Kim SC, Kim DW, Shim YH, Bang JS, Oh HS, Wan KS et al. In vivo evaluation of polymeric micellar paclitaxel formulation: toxicity and efficacy. J Control Release 2001; 72(1-3):191-202.

34. Ostacolo L, Marra M, Ungaro F, Zappavigna S, Maglio G, Quaglia F et al. In vitro anticancer activity of docetaxel-loaded micelles based on poly(ethylene oxide)-poly(epsilon-caprolactone) block copolymers: Do nanocarrier properties have a role? J Control Release 2010; 148(2):255-263.

35. Ebrahim Attia AB, Ong ZY, Hedrick JL, Lee PP, Ee PLR, Hammond PT et al. Mixed micelles self-assembled from block copolymers for drug delivery. Current Opinion in Colloid & Interface Science 2011; 16(3):182-194.

36. Chen L, Sha X, Jiang X, Chen Y, Ren Q, Fang X. Pluronic P105/F127 mixed micelles for the delivery of docetaxel against Taxol-resistant non-small cell lung cancer: optimization and in vitro, in vivo evaluation. Int J Nanomedicine 2013; 8:73-84.

37. Mehnert W, Mader K. Solid lipid nanoparticles: production, characterization and applications. Adv Drug Deliv Rev 2001; 47(2-3):165-196.

38. Xu Z, Chen L, Gu W, Gao Y, Lin L, Zhang Z et al. The performance of docetaxel-loaded solid lipid nanoparticles targeted to hepatocellular carcinoma. Biomaterials 2009; 30(2):226-232.

39. Sloat BR, Sandoval MA, Li D, Chung WG, Lansakara P, Proteau PJ et al. In vitro and in vivo anti-tumor activities of a gemcitabine derivative carried by nanoparticles. Int J Pharm 2011; 409(1-2):278-288.

40. Mosallaei N, Jaafari MR, Hanafi-Bojd MY, Golmohammadzadeh S, Malaekeh-Nikouei B. Docetaxel-loaded solid lipid nanoparticles: preparation, characterization, in vitro, and in vivo evaluations. J Pharm Sci 2013; 102(6):1994-2004.

41. Parveen R, Ahmad FJ, Iqbal Z, Samim M, Ahmad S. Solid lipid nanoparticles of anticancer drug andrographolide: formulation, in vitro and in vivo studies. Drug Dev Ind Pharm 2013.

42. Muller RH, Mader K, Gohla S. Solid lipid nanoparticles (SLN) for controlled drug delivery - a review of the state of the art. Eur J Pharm Biopharm 2000; 50(1):161-177.

43. Wong HL, Bendayan R, Rauth AM, Li Y, Wu XY. Chemotherapy with anticancer drugs encapsulated in solid lipid nanoparticles. Adv Drug Deliv Rev 2007; 59(6):491-504.

44. Feng L, Mumper RJ. A critical review of lipid-based nanoparticles for taxane delivery. Cancer Lett 2013; 334(2):157-175.

45. Sanchis J, Canal F, Lucas R, Vicent MJ. Polymer-drug conjugates for novel molecular targets. Nanomedicine (Lond) 2010; 5(6):915-935.

46. Pasut G, Veronese FM. PEG conjugates in clinical development or use as anticancer agents: an overview. Adv Drug Deliv Rev 2009; 61(13):1177-1188.

47. Duncan R. Development of HPMA copolymer-anticancer conjugates: clinical experience and lessons learnt. Adv Drug Deliv Rev 2009; 61(13):1131-1148.

48. Li C, Wallace S. Polymer-drug conjugates: recent development in clinical oncology. Adv Drug Deliv Rev 2008; 60(8):886-898.

49. Ringsdorf H. Structure and properties of pharmacologically active polymers. J polym sci , C Polym symp 1975; 51(1):135-153.

50. Vasey PA, Kaye SB, Morrison R, Twelves C, Wilson P, Duncan R et al. Phase I clinical and pharmacokinetic study of PK1 [N-(2-hydroxypropyl)methacrylamide copolymer doxorubicin]: first member of a new class of chemotherapeutic agents-drug-polymer conjugates. Cancer Research Campaign Phase I/II Committee. Clin Cancer Res 1999; 5(1):83-94.

51. Lammers T, Subr V, Ulbrich K, Peschke P, Huber PE, Hennink WE et al. Simultaneous delivery of doxorubicin and gemcitabine to tumors in vivo using prototypic polymeric drug carriers. Biomaterials 2009; 30(20):3466-3475.

52. Tong R, Yala L, Fan TM, Cheng J. The formulation of aptamer-coated paclitaxel-polylactide nanoconjugates and their targeting to cancer cells. Biomaterials 2010; 31(11):3043-3053.

53. Jeyapalan S, Boxerman J, Donahue J, Goldman M, Kinsella T, Dipetrillo T et al. Paclitaxel Poliglumex, Temozolomide, and Radiation for Newly Diagnosed High-grade Glioma: A Brown University Oncology Group Study. Am J Clin Oncol 2013.

54. Stirland DL, Nichols JW, Miura S, Bae YH. Mind the gap: A survey of how cancer drug carriers are susceptible to the gap between research and practice. J Control Release 2013.

55. O'Brien ME, Socinski MA, Popovich AY, Bondarenko IN, Tomova A, Bilynsky BT et al. Randomized phase III trial comparing single-agent paclitaxel Poliglumex (CT-2103, PPX) with single-agent gemcitabine or vinorelbine for the treatment of PS 2 patients with chemotherapy-naive advanced non-small cell lung cancer. J Thorac Oncol 2008; 3(7):728-734.

56. Paz-Ares L, Ross H, O'Brien M, Riviere A, Gatzemeier U, Von PJ et al. Phase III trial comparing paclitaxel poliglumex vs docetaxel in the second-line treatment of non-small-cell lung cancer. Br J Cancer 2008; 98(10):1608-1613.

57. Sievers EL, Senter PD. Antibody-drug conjugates in cancer therapy. Annu Rev Med 2013; 64:15-29.

58. Ricart AD, Tolcher AW. Technology insight: cytotoxic drug immunoconjugates for cancer therapy. Nat Clin Pract Oncol 2007; 4(4):245-255.

59. Wu AM, Senter PD. Arming antibodies: prospects and challenges for immunoconjugates. Nat Biotechnol 2005; 23(9):1137-1146.

60. Junutula JR, Raab H, Clark S, Bhakta S, Leipold DD, Weir S et al. Site-specific conjugation of a cytotoxic drug to an antibody improves the therapeutic index. Nat Biotechnol 2008; 26(8):925-932.

61. Mosure KW, Henderson AJ, Klunk LJ, Knipe JO. Disposition of conjugate-bound and free doxorubicin in tumor-bearing mice following administration of a BR96-doxorubicin immunoconjugate (BMS 182248). Cancer Chemother Pharmacol 1997; 40(3):251-258.

62. Gerber HP, Koehn FE, Abraham RT. The antibody-drug conjugate: an enabling modality for natural product-based cancer therapeutics. Nat Prod Rep 2013; 30(5):625-639.

63. Zhao RY, Wilhelm SD, Audette C, Jones G, Leece BA, Lazar AC et al. Synthesis and evaluation of hydrophilic linkers for antibody-maytansinoid conjugates. J Med Chem 2011; 54(10):3606-3623.

64. Kovtun YV, Audette CA, Mayo MF, Jones GE, Doherty H, Maloney EK et al. Antibody-maytansinoid conjugates designed to bypass multidrug resistance. Cancer Res 2010; 70(6):2528-2537.

65. Carter PJ, Senter PD. Antibody-drug conjugates for cancer therapy. Cancer J 2008; 14(3):154-169.

66. Chan SY, Gordon AN, Coleman RE, Hall JB, Berger MS, Sherman ML et al. A phase 2 study of the cytotoxic immunoconjugate CMB-401 (hCTM01-calicheamicin) in patients with platinum-sensitive recurrent epithelial ovarian carcinoma. Cancer Immunol Immunother 2003; 52(4):243-248.

67. Lambert JM. Drug-conjugated monoclonal antibodies for the treatment of cancer. Curr Opin Pharmacol 2005; 5(5):543-549.

68. Kharfan-Dabaja MA, Hamadani M, Reljic T, Pyngolil R, Komrokji RS, Lancet JE et al. Gemtuzumab ozogamicin for treatment of newly diagnosed acute myeloid leukaemia: a systematic review and meta-analysis. Br J Haematol 2013; 163(3):315-325.

69. Newland AM, Li JX, Wasco LE, Aziz MT, Lowe DK. Brentuximab vedotin: a CD30-directed antibody-cytotoxic drug conjugate. Pharmacotherapy 2013; 33(1):93-104.

70. Wong BS, Yoong SL, Jagusiak A, Panczyk T, Ho HK, Ang WH et al. Carbon nanotubes for delivery of small molecule drugs. Adv Drug Deliv Rev 2013.

71. Liang XJ, Meng H, Wang Y, He H, Meng J, Lu J et al. Metallofullerene nanoparticles circumvent tumor resistance to cisplatin by reactivating endocytosis. Proc Natl Acad Sci U S A 2010; 107(16):7449-7454.

72. Dreaden EC, Austin LA, Mackey MA, El-Sayed MA. Size matters: gold nanoparticles in targeted cancer drug delivery. Ther Deliv 2012; 3(4):457-478.

73. Shen J, Song G, An M, Li X, Wu N, Ruan K et al. The use of hollow mesoporous silica nanospheres to encapsulate bortezomib and improve efficacy for non-small cell lung cancer therapy. Biomaterials 2013.

74. Li X, Li H, Yi W, Chen J, Liang B. Acid-triggered core cross-linked nanomicelles for targeted drug delivery and magnetic resonance imaging in liver cancer cells. Int J Nanomedicine 2013; 8:3019-3031.

75. Diaz A, Saxena V, Gonzalez J, David A, Casanas B, Carpenter C et al. Zirconium phosphate nano-platelets: a novel platform for drug delivery in cancer therapy. Chem Commun (Camb) 2012; 48(12):1754-1756.

76. Fang M, Yuan JP, Peng CW, Pang DW, Li Y. Quantum dots-based in situ molecular imaging of dynamic changes of collagen IV during cancer invasion. Biomaterials 2013; 34(34):8708-8717.

77. Gautier J, lard-Vannier E, Munnier E, Souce M, Chourpa I. Recent advances in theranostic nanocarriers of doxorubicin based on iron oxide and gold nanoparticles. J Control Release 2013; 169(1-2):48-61.

78. Chen Y, Chen H, Shi J. In vivo bio-safety evaluations and diagnostic/therapeutic applications of chemically designed mesoporous silica nanoparticles. Adv Mater 2013; 25(23):3144-3176.

79. Probst CE, Zrazhevskiy P, Bagalkot V, Gao X. Quantum dots as a platform for nanoparticle drug delivery vehicle design. Adv Drug Deliv Rev 2013; 65(5):703-718.

80. Yang F, Jin C, Subedi S, Lee CL, Wang Q, Jiang Y et al. Emerging inorganic nanomaterials for pancreatic cancer diagnosis and treatment. Cancer Treat Rev 2012; 38(6):566-579.

81. Mukerjee A, Ranjan AP, Vishwanatha JK. Combinatorial nanoparticles for cancer diagnosis and therapy. Curr Med Chem 2012; 19(22):3714-3721.

82. Matsumura Y, Maeda H. A new concept for macromolecular therapeutics in cancer chemotherapy: mechanism of tumoritropic accumulation of proteins and the antitumor agent smancs. Cancer Res 1986; 46(12 Pt 1):6387-6392.

83. Torchilin V. Tumor delivery of macromolecular drugs based on the EPR effect. Adv Drug Deliv Rev 2011; 63(3):131-135.

84. Maeda H. Tumor-selective delivery of macromolecular drugs via the EPR effect: background and future prospects. Bioconjug Chem 2010; 21(5):797-802.

85. Wu J, Akaike T, Maeda H. Modulation of enhanced vascular permeability in tumors by a bradykinin antagonist, a cyclooxygenase inhibitor, and a nitric oxide scavenger. Cancer Res 1998; 58(1):159-165.

86. Brannon-Peppas L, Blanchette JO. Nanoparticle and targeted systems for cancer therapy. Adv Drug Deliv Rev 2004; 56(11):1649-1659.

87. Iyer AK, Khaled G, Fang J, Maeda H. Exploiting the enhanced permeability and retention effect for tumor targeting. Drug Discov Today 2006; 11(17-18):812-818.

88. Alexis F, Rhee JW, Richie JP, Radovic-Moreno AF, Langer R, Farokhzad OC. New frontiers in nanotechnology for cancer treatment. Urol Oncol 2008; 26(1):74-85.

89. Maeda H, Bharate GY, Daruwalla J. Polymeric drugs for efficient tumor-targeted drug delivery based on EPR-effect. Eur J Pharm Biopharm 2009; 71(3):409-419.

90. Hobson B, Denekamp J. Endothelial proliferation in tumours and normal tissues: continuous labelling studies. Br J Cancer 1984; 49(4):405-413.

91. Fang J, Nakamura H, Maeda H. The EPR effect: Unique features of tumor blood vessels for drug delivery, factors involved, and limitations and augmentation of the effect. Adv Drug Deliv Rev 2011; 63(3):136-151.

92. Maeda H, Sawa T, Konno T. Mechanism of tumor-targeted delivery of macromolecular drugs, including the EPR effect in solid tumor and clinical overview of the prototype polymeric drug SMANCS. J Control Release 2001; 74(1-3):47-61.

93. Maeda H. SMANCS and polymer-conjugated macromolecular drugs: advantages in cancer chemotherapy. Advanced Drug Delivery Reviews 1991; 6(2):181-202.

94. Prabhakar U, Maeda H, Jain RK, Sevick-Muraca EM, Zamboni W, Farokhzad OC et al. Challenges and key considerations of the enhanced permeability and retention effect for nanomedicine drug delivery in oncology. Cancer Res 2013; 73(8):2412-2417.

95. Bae YH, Park K. Targeted drug delivery to tumors: myths, reality and possibility. J Control Release 2011; 153(3):198-205.

96. Bae YH. Drug targeting and tumor heterogeneity. J Control Release 2009; 133(1):2-3.

97. Denison TA, Bae YH. Tumor heterogeneity and its implication for drug delivery. J Control Release 2012; 164(2):187-191.

98. Nichols JW, Bae YH. Odyssey of a cancer nanoparticle: from injection site to site of action. Nano Today 2012; 7(6):606-618.

99. Noguchi A, Takahashi T, Yamaguchi T, Kitamura K, Noguchi A, Tsurumi H et al. Enhanced tumor localization of monoclonal antibody by treatment with kininase II inhibitor and angiotensin II. Jpn J Cancer Res 1992; 83(3):240-243.

100. Seki T, Fang J, Maeda H. Enhanced delivery of macromolecular antitumor drugs to tumors by nitroglycerin application. Cancer Sci 2009; 100(12):2426-2430.

101. Jain RK. Normalization of tumor vasculature: an emerging concept in antiangiogenic therapy. Science 2005; 307(5706):58-62.

102. Yuan F, Chen Y, Dellian M, Safabakhsh N, Ferrara N, Jain RK. Time-dependent vascular regression and permeability changes in established human tumor xenografts induced by an anti-vascular endothelial growth factor/vascular permeability factor antibody. Proc Natl Acad Sci U S A 1996; 93(25):14765-14770.

103. Goel S, Duda DG, Xu L, Munn LL, Boucher Y, Fukumura D et al. Normalization of the vasculature for treatment of cancer and other diseases. Physiol Rev 2011; 91(3):1071-1121.

104. Jain RK, Stylianopoulos T. Delivering nanomedicine to solid tumors. Nat Rev Clin Oncol 2010; 7(11):653-664.

105. Carmeliet P, Jain RK. Principles and mechanisms of vessel normalization for cancer and other angiogenic diseases. Nat Rev Drug Discov 2011; 10(6):417-427.

106. Goel S, Wong AH, Jain RK. Vascular normalization as a therapeutic strategy for malignant and nonmalignant disease. Cold Spring Harb Perspect Med 2012; 2(3):a006486.

107. Chauhan VP, Stylianopoulos T, Martin JD, Popovic Z, Chen O, Kamoun WS et al. Normalization of tumour blood vessels improves the delivery of nanomedicines in a size-dependent manner. Nat Nanotechnol 2012; 7(6):383-388.

108. Huang C, Zhang Y, Yuan H, Gao H, Zhang S. Role of nanoparticle geometry in endocytosis: laying down to stand up. Nano Lett 2013; 13(9):4546-4550.

109. Byrne JD, Betancourt T, Brannon-Peppas L. Active targeting schemes for nanoparticle systems in cancer therapeutics. Adv Drug Deliv Rev 2008; 60(15):1615-1626.

110. Dagar A, Kuzmis A, Rubinstein I, Sekosan M, Onyuksel H. VIP-targeted Cytotoxic Nanomedicine for Breast Cancer. Drug Deliv Transl Res 2012; 2(6):454-462.

111. Cirstoiu-Hapca A, Buchegger F, Bossy L, Kosinski M, Gurny R, Delie F. Nanomedicines for active targeting: physico-chemical characterization of

paclitaxel-loaded anti-HER2 immunonanoparticles and in vitro functional studies on target cells. Eur J Pharm Sci 2009; 38(3):230-237.

112. Nobs L, Buchegger F, Gurny R, Allemann E. Biodegradable nanoparticles for direct or two-step tumor immunotargeting. Bioconjug Chem 2006; 17(1):139-145.

113. Cirstoiu-Hapca A, Bossy-Nobs L, Buchegger F, Gurny R, Delie F. Differential tumor cell targeting of anti-HER2 (Herceptin) and anti-CD20 (Mabthera) coupled nanoparticles. Int J Pharm 2007; 331(2):190-196.

114. Sandoval MA, Sloat BR, Lansakara P, Kumar A, Rodriguez BL, Kiguchi K et al. EGFR-targeted stearoyl gemcitabine nanoparticles show enhanced anti-tumor activity. J Control Release 2012; 157(2):287-296.

115. Yhee JY, Lee SJ, Lee S, Song S, Min HS, Kang SW et al. Tumor-targeting Transferrin Nanoparticles for Systemic Polymerized siRNA Delivery in Tumor-bearing Mice. Bioconjug Chem 2013.

116. Stephenson SM, Low PS, Lee RJ. Folate receptor-mediated targeting of liposomal drugs to cancer cells. Methods Enzymol 2004; 387:33-50.

117. Lu Y, Low PS. Folate-mediated delivery of macromolecular anticancer therapeutic agents. Adv Drug Deliv Rev 2002; 54(5):675-693.

118. Saxena V, Naguib Y, Hussain MD. Folate receptor targeted 17-allylamino-17-demethoxygeldanamycin (17-AAG) loaded polymeric nanoparticles for breast cancer. Colloids Surf B Biointerfaces 2012; 94:274-280.

119. Hrkach J, Von HD, Mukkaram AM, Andrianova E, Auer J, Campbell T et al. Preclinical development and clinical translation of a PSMA-targeted docetaxel nanoparticle with a differentiated pharmacological profile. Sci Transl Med 2012; 4(128):128ra39.

120. Elsabahy M, Wooley KL. Design of polymeric nanoparticles for biomedical delivery applications. Chem Soc Rev 2012; 41(7):2545-2561.

121. Huynh NT, Roger E, Lautram N, Benoit JP, Passirani C. The rise and rise of stealth nanocarriers for cancer therapy: passive versus active targeting. Nanomedicine (Lond) 2010; 5(9):1415-1433.

122. Bertrand N, Leroux JC. The journey of a drug-carrier in the body: an anatomo-physiological perspective. J Control Release 2012; 161(2):152-163.

123. Owens DE, III, Peppas NA. Opsonization, biodistribution, and pharmacokinetics of polymeric nanoparticles. Int J Pharm 2006; 307(1):93-102.

124. Ernsting MJ, Murakami M, Roy A, Li SD. Factors controlling the pharmacokinetics, biodistribution and intratumoral penetration of nanoparticles. J Control Release 2013.

125. Betancourt T, Byrne JD, Sunaryo N, Crowder SW, Kadapakkam M, Patel S et al. PEGylation strategies for active targeting of PLA/PLGA nanoparticles. J Biomed Mater Res A 2009; 91(1):263-276.

126. Perry JL, Reuter KG, Kai MP, Herlihy KP, Jones SW, Luft JC et al. PEGylated PRINT nanoparticles: the impact of PEG density on protein binding, macrophage association, biodistribution, and pharmacokinetics. Nano Lett 2012; 12(10):5304-5310.

127. bu Lila AS, Kiwada H, Ishida T. The accelerated blood clearance (ABC) phenomenon: Clinical challenge and approaches to manage. J Control Release 2013; 172(1):38-47.

128. Alaaeldin E, bu Lila AS, Moriyoshi N, Sarhan HA, Ishida T, Khaled KA et al. The co-delivery of oxaliplatin abrogates the immunogenic response to PEGylated siRNA-lipoplex. Pharm Res 2013; 30(9):2344-2354.

129. Yoo JW, Irvine DJ, Discher DE, Mitragotri S. Bio-inspired, bioengineered and biomimetic drug delivery carriers. Nat Rev Drug Discov 2011; 10(7):521-535.

130. Cai S, Vijayan K, Cheng D, Lima EM, Discher DE. Micelles of different morphologies--advantages of worm-like filomicelles of PEO-PCL in paclitaxel delivery. Pharm Res 2007; 24(11):2099-2109.

131. Geng Y, Dalhaimer P, Cai S, Tsai R, Tewari M, Minko T et al. Shape effects of filaments versus spherical particles in flow and drug delivery. Nat Nanotechnol 2007; 2(4):249-255.

132. Parodi A, Quattrocchi N, van d, V, Chiappini C, Evangelopoulos M, Martinez JO et al. Synthetic nanoparticles functionalized with biomimetic leukocyte membranes possess cell-like functions. Nat Nanotechnol 2013; 8(1):61-68.

133. Jiang X, Xin H, Ren Q, Gu J, Zhu L, Du F et al. Nanoparticles of 2-deoxy-d-glucose functionalized poly(ethylene glycol)-co-poly(trimethylene carbonate) for dual-targeted drug delivery in glioma treatment. Biomaterials 2013.

134. Miura Y, Takenaka T, Toh K, Wu S, Nishihara H, Kano MR et al. Cyclic RGD-Linked Polymeric Micelles for Targeted Delivery of Platinum Anticancer Drugs to Glioblastoma through the Blood-Brain Tumor Barrier. ACS Nano 2013; 7(10):8583-8592.

135. Gao H, Yang Z, Zhang S, Cao S, Pang Z, Yang X et al. Glioma-homing peptide with a cell-penetrating effect for targeting delivery with enhanced glioma localization, penetration and suppression of glioma growth. J Control Release 2013.

136. Rasheed ZA, Matsui W, Maitra A. Pathology of pancreatic stroma in PDAC. 2012.

137. Liss AS, Thayer SP. Therapeutic targeting of pancreatic stroma. 2012.

138. Kirtane AR, Kalscheuer SM, Panyam J. Exploiting nanotechnology to overcome tumor drug resistance: Challenges and opportunities. Adv Drug Deliv Rev 2013.

139. Heinemann V, Reni M, Ychou M, Richel DJ, Macarulla T, Ducreux M. Tumour-stroma interactions in pancreatic ductal adenocarcinoma: Rationale and current evidence for new therapeutic strategies. Cancer Treat Rev 2013.

140. Cox TR, Erler JT. Remodeling and homeostasis of the extracellular matrix: implications for fibrotic diseases and cancer. Dis Model Mech 2011; 4(2):165-178.

141. Lu P, Weaver VM, Werb Z. The extracellular matrix: a dynamic niche in cancer progression. J Cell Biol 2012; 196(4):395-406.

142. Levental KR, Yu H, Kass L, Lakins JN, Egeblad M, Erler JT et al. Matrix crosslinking forces tumor progression by enhancing integrin signaling. Cell 2009; 139(5):891-906.

143. Kessenbrock K, Plaks V, Werb Z. Matrix metalloproteinases: regulators of the tumor microenvironment. Cell 2010; 141(1):52-67.

144. Erler JT, Weaver VM. Three-dimensional context regulation of metastasis. Clin Exp Metastasis 2009; 26(1):35-49.

145. Tredan O, Galmarini CM, Patel K, Tannock IF. Drug resistance and the solid tumor microenvironment. J Natl Cancer Inst 2007; 99(19):1441-1454.

146. Minchinton AI, Tannock IF. Drug penetration in solid tumours. Nat Rev Cancer 2006; 6(8):583-592.

147. Sermeus A, Rebucci M, Fransolet M, Flamant L, Desmet D, Delaive E et al. Differential effect of hypoxia on etoposide-induced DNA damage response and p53 regulation in different cell types. J Cell Physiol 2013; 228(12):2365-2376.

148. Erler JT, Bennewith KL, Nicolau M, Dornhofer N, Kong C, Le QT et al. Lysyl oxidase is essential for hypoxia-induced metastasis. Nature 2006; 440(7088):1222-1226.

149. Brown JM, Wilson WR. Exploiting tumour hypoxia in cancer treatment. Nat Rev Cancer 2004; 4(6):437-447.

150. Comerford KM, Wallace TJ, Karhausen J, Louis NA, Montalto MC, Colgan SP. Hypoxia-inducible factor-1-dependent regulation of the multidrug resistance (MDR1) gene. Cancer Res 2002; 62(12):3387-3394.

151. Gerweck LE, Vijayappa S, Kozin S. Tumor pH controls the in vivo efficacy of weak acid and base chemotherapeutics. Mol Cancer Ther 2006; 5(5):1275-1279.

152. Jain RK. Transport of molecules in the tumor interstitium: a review. Cancer Res 1987; 47(12):3039-3051.

153. Heldin CH, Rubin K, Pietras K, Ostman A. High interstitial fluid pressure - an obstacle in cancer therapy. Nat Rev Cancer 2004; 4(10):806-813.

154. Saggar JK, Yu M, Tan Q, Tannock IF. The tumor microenvironment and strategies to improve drug distribution. Front Oncol 2013; 3:154.

155. Biswas SK, Allavena P, Mantovani A. Tumor-associated macrophages: functional diversity, clinical significance, and open questions. Semin Immunopathol 2013; 35(5):585-600.

156. Balkwill F, Mantovani A. Inflammation and cancer: back to Virchow? Lancet 2001; 357(9255):539-545.

157. Siveen KS, Kuttan G. Role of macrophages in tumour progression. Immunol Lett 2009; 123(2):97-102.

158. Bingle L, Brown NJ, Lewis CE. The role of tumour-associated macrophages in tumour progression: implications for new anticancer therapies. J Pathol 2002; 196(3):254-265.

159. Pollard JW. Tumour-educated macrophages promote tumour progression and metastasis. Nat Rev Cancer 2004; 4(1):71-78.

160. Coffelt SB, Hughes R, Lewis CE. Tumor-associated macrophages: effectors of angiogenesis and tumor progression. Biochim Biophys Acta 2009; 1796(1):11-18.

161. Owen JL, Mohamadzadeh M. Macrophages and chemokines as mediators of angiogenesis. Front Physiol 2013; 4:159.

162. Marsh T, Pietras K, McAllister SS. Fibroblasts as architects of cancer pathogenesis. Biochim Biophys Acta 2013; 1832(7):1070-1078.

163. Kalluri R, Zeisberg M. Fibroblasts in cancer. Nat Rev Cancer 2006; 6(5):392-401.

164. Cirri P, Chiarugi P. Cancer associated fibroblasts: the dark side of the coin. Am J Cancer Res 2011; 1(4):482-497.

165. Goruppi S, Dotto GP. Mesenchymal stroma: primary determinant and therapeutic target for epithelial cancer. Trends Cell Biol 2013.

166. Madar S, Goldstein I, Rotter V. 'Cancer associated fibroblasts'--more than meets the eye. Trends Mol Med 2013; 19(8):447-453.

167. Dvorak HF. Tumors: wounds that do not heal. Similarities between tumor stroma generation and wound healing. N Engl J Med 1986; 315(26):1650-1659.

168. Polanska UM, Orimo A. Carcinoma-associated fibroblasts: non-neoplastic tumour-promoting mesenchymal cells. J Cell Physiol 2013; 228(8):1651-1657.

169. Murakami M, Ernsting MJ, Undzys E, Holwell N, Foltz WD, Li SD. Docetaxel conjugate nanoparticles that target alpha-smooth muscle actin-expressing stromal cells suppress breast cancer metastasis. Cancer Res 2013; 73(15):4862-4871.

170. Whatcott CJ, Han H, Posner RG, Hostetter G, Von Hoff DD. Targeting the tumor microenvironment in cancer: why hyaluronidase deserves a second look. Cancer Discov 2011; 1(4):291-296.

171. Thompson CB, Shepard HM, O'Connor PM, Kadhim S, Jiang P, Osgood RJ et al. Enzymatic depletion of tumor hyaluronan induces antitumor responses in preclinical animal models. Mol Cancer Ther 2010; 9(11):3052-3064.

172. Baumgartner G, Gomar-Hoss C, Sakr L, Ulsperger E, Wogritsch C. The impact of extracellular matrix on the chemoresistance of solid tumors--experimental and clinical results of hyaluronidase as additive to cytostatic chemotherapy. Cancer Lett 1998; 131(1):85-99.

173. Pillwein K, Fuiko R, Slavc I, Czech T, Hawliczek G, Bernhardt G et al. Hyaluronidase additional to standard chemotherapy improves outcome for children with malignant brain tumors. Cancer Lett 1998; 131(1):101-108.

174. Yocum RC, Kennard D, Heiner LS. Assessment and implication of the allergic sensitivity to a single dose of recombinant human hyaluronidase injection: a double-blind, placebo-controlled clinical trial. J Infus Nurs 2007; 30(5):293-299.

175. Provenzano PP, Cuevas C, Chang AE, Goel VK, Von Hoff DD, Hingorani SR. Enzymatic targeting of the stroma ablates physical barriers to treatment of pancreatic ductal adenocarcinoma. Cancer Cell 2012; 21(3):418-429.

176. Provenzano PP, Hingorani SR. Hyaluronan, fluid pressure, and stromal resistance in pancreas cancer. Br J Cancer 2013; 108(1):1-8.

177. Yang C, Liu Y, He Y, Du Y, Wang W, Shi X et al. The use of HA oligosaccharide-loaded nanoparticles to breach the endogenous hyaluronan glycocalyx for breast cancer therapy. Biomaterials 2013; 34(28):6829-6838.

178. Burris HA, III, Moore MJ, Andersen J, Green MR, Rothenberg ML, Modiano MR et al. Improvements in survival and clinical benefit with gemcitabine as first-line therapy for patients with advanced pancreas cancer: a randomized trial. J Clin Oncol 1997; 15(6):2403-2413.

179. Chung WG, Sandoval MA, Sloat BR, Lansakara P, Cui Z. Stearoyl gemcitabine nanoparticles overcome resistance related to the over-expression of ribonucleotide reductase subunit M1. J Control Release 2012; 157(1):132-140.

180. Olson P, Hanahan D. Cancer. Breaching the cancer fortress. Science 2009; 324(5933):1400-1401.

181. Olive KP, Jacobetz MA, Davidson CJ, Gopinathan A, McIntyre D, Honess D et al. Inhibition of Hedgehog signaling enhances delivery of chemotherapy in a mouse model of pancreatic cancer. Science 2009; 324(5933):1457-1461.

182. Sandhiya S, Melvin G, Kumar SS, Dkhar SA. The dawn of hedgehog inhibitors: Vismodegib. J Pharmacol Pharmacother 2013; 4(1):4-7.

183. Xu Y, Chenna V, Hu C, Sun HX, Khan M, Bai H et al. Polymeric nanoparticle-encapsulated hedgehog pathway inhibitor HPI-1 (NanoHHI) inhibits systemic metastases in an orthotopic model of human hepatocellular carcinoma. Clin Cancer Res 2012; 18(5):1291-1302.

184. Chenna V, Hu C, Pramanik D, Aftab BT, Karikari C, Campbell NR et al. A polymeric nanoparticle encapsulated small-molecule inhibitor of Hedgehog signaling (NanoHHI) bypasses secondary mutational resistance to Smoothened antagonists. Mol Cancer Ther 2012; 11(1):165-173.

185. Heinemann V, Haas M, Boeck S. Systemic treatment of advanced pancreatic cancer. Cancer Treat Rev 2012; 38(7):843-853.

186. Yardley DA. nab-Paclitaxel mechanisms of action and delivery. J Control Release 2013; 170(3):365-372.

187. Desai N, Trieu V, Damascelli B, Soon-Shiong P. SPARC Expression Correlates with Tumor Response to Albumin-Bound Paclitaxel in Head and Neck Cancer Patients. Transl Oncol 2009; 2(2):59-64.

188. Neuzillet C, Tijeras-Raballand A, Cros J, Faivre S, Hammel P, Raymond E. Stromal expression of SPARC in pancreatic adenocarcinoma. Cancer Metastasis Rev 2013.

189. Von Hoff DD, Ramanathan RK, Borad MJ, Laheru DA, Smith LS, Wood TE et al. Gemcitabine plus nab-paclitaxel is an active regimen in patients with advanced pancreatic cancer: a phase I/II trial. J Clin Oncol 2011; 29(34):4548-4554.

190. Von Hoff DD, Ervin T, Arena FP, Chiorean EG, Infante J, Moore M et al. Increased Survival in Pancreatic Cancer with nab-Paclitaxel plus Gemcitabine. N Engl J Med 2013.

191. Alvarez R, Musteanu M, Garcia-Garcia E, Lopez-Casas PP, Megias D, Guerra C et al. Stromal disrupting effects of nab-paclitaxel in pancreatic cancer. Br J Cancer 2013; 109(4):926-933.

192. Frese KK, Neesse A, Cook N, Bapiro TE, Lolkema MP, Jodrell DI et al. nab-Paclitaxel potentiates gemcitabine activity by reducing cytidine deaminase levels in a mouse model of pancreatic cancer. Cancer Discov 2012; 2(3):260-269.

193. Lansakara P, Rodriguez BL, Cui Z. Synthesis and in vitro evaluation of novel lipophilic monophosphorylated gemcitabine derivatives and their nanoparticles. Int J Pharm 2012; 429(1-2):123-134.

194. Ernsting MJ, Murakami M, Undzys E, Aman A, Press B, Li SD. A docetaxel-carboxymethylcellulose nanoparticle outperforms the approved taxane nanoformulation, Abraxane, in mouse tumor models with significant control of metastases. J Control Release 2012; 162(3):575-581.

195. Ernsting MJ, Foltz WD, Undzys E, Tagami T, Li SD. Tumor-targeted drug delivery using MR-contrasted docetaxel - carboxymethylcellulose nanoparticles. Biomaterials 2012; 33(15):3931-3941.

196. Ernsting MJ, Tang WL, MacCallum NW, Li SD. Preclinical pharmacokinetic, biodistribution, and anti-cancer efficacy studies of a docetaxel-carboxymethylcellulose nanoparticle in mouse models. Biomaterials 2012; 33(5):1445-1454.

197. Ernsting MJ, Tang WL, MacCallum N, Li SD. Synthetic modification of carboxymethylcellulose and use thereof to prepare a nanoparticle forming conjugate of docetaxel for enhanced cytotoxicity against cancer cells. Bioconjug Chem 2011; 22(12):2474-2486.

198. Lee ES, Gao Z, Bae YH. Recent progress in tumor pH targeting nanotechnology. J Control Release 2008; 132(3):164-170.

199. Torchilin V. Multifunctional and stimuli-sensitive pharmaceutical nanocarriers. Eur J Pharm Biopharm 2009; 71(3):431-444.

200. Zhu L, Torchilin VP. Stimulus-responsive nanopreparations for tumor targeting. Integr Biol (Camb) 2013; 5(1):96-107.

201. Ganta S, Devalapally H, Shahiwala A, Amiji M. A review of stimuli-responsive nanocarriers for drug and gene delivery. J Control Release 2008; 126(3):187-204.

202. Jensen SS, Andresen TL, Davidsen J, Hoyrup P, Shnyder SD, Bibby MC et al. Secretory phospholipase A2 as a tumor-specific trigger for targeted delivery of a novel class of liposomal prodrug anticancer etherlipids. Mol Cancer Ther 2004; 3(11):1451-1458.

203. Andresen TL, Davidsen J, Begtrup M, Mouritsen OG, Jorgensen K. Enzymatic release of antitumor ether lipids by specific phospholipase A2 activation of liposome-forming prodrugs. J Med Chem 2004; 47(7):1694-1703.

204. Lee ES, Na K, Bae YH. Polymeric micelle for tumor pH and folate-mediated targeting. J Control Release 2003; 91(1-2):103-113.

205. Patel NR, Pattni BS, Abouzeid AH, Torchilin VP. Nanopreparations to overcome multidrug resistance in cancer. Adv Drug Deliv Rev 2013.

206. Poon Z, Chang D, Zhao X, Hammond PT. Layer-by-layer nanoparticles with a pH-sheddable layer for in vivo targeting of tumor hypoxia. ACS Nano 2011; 5(6):4284-4292.

207. Sawant RM, Hurley JP, Salmaso S, Kale A, Tolcheva E, Levchenko TS et al. "SMART" drug delivery systems: double-targeted pH-responsive pharmaceutical nanocarriers. Bioconjug Chem 2006; 17(4):943-949.

208. Zhu S, Lansakara P, Li X, Cui Z. Lysosomal delivery of a lipophilic gemcitabine prodrug using novel acid-sensitive micelles improved its antitumor activity. Bioconjug Chem 2012; 23(5):966-980.

209. Zhu S, Wonganan P, Lansakara P, O'Mary HL, Li Y, Cui Z. The effect of the acid-sensitivity of 4-(N)-stearoyl gemcitabine-loaded micelles on drug resistance caused by RRM1 overexpression. Biomaterials 2013; 34(9):2327-2339.

210. Yanasarn N, Sloat BR, Cui Z. Nanoparticles engineered from lecithin-in-water emulsions as a potential delivery system for docetaxel. Int J Pharm 2009; 379(1):174-180.

211. Zhu S, Niu M, O'Mary H, Cui Z. Targeting of Tumor-Associated Macrophages Made Possible by PEG-Sheddable, Mannose-Modified Nanoparticles. Mol Pharm 2013.

212. Zhu L, Wang T, Perche F, Taigind A, Torchilin VP. Enhanced anticancer activity of nanopreparation containing an MMP2-sensitive PEG-drug conjugate and cell-penetrating moiety. Proc Natl Acad Sci U S A 2013; 110(42):17047-17052.

213. Xu S, Olenyuk BZ, Okamoto CT, Hamm-Alvarez SF. Targeting receptor-mediated endocytotic pathways with nanoparticles: rationale and advances. Adv Drug Deliv Rev 2013; 65(1):121-138.

214. Sahay G, Alakhova DY, Kabanov AV. Endocytosis of nanomedicines. J Control Release 2010; 145(3):182-195.

215. Varkouhi AK, Scholte M, Storm G, Haisma HJ. Endosomal escape pathways for delivery of biologicals. J Control Release 2011; 151(3):220-228.

216. Akinc A, Thomas M, Klibanov AM, Langer R. Exploring polyethylenimine-mediated DNA transfection and the proton sponge hypothesis. J Gene Med 2005; 7(5):657-663.

217. Vercauteren D, Rejman J, Martens TF, Demeester J, De Smedt SC, Braeckmans K. On the cellular processing of non-viral nanomedicines for nucleic acid delivery: mechanisms and methods. J Control Release 2012; 161(2):566-581.

218. Duncan R, Richardson SC. Endocytosis and intracellular trafficking as gateways for nanomedicine delivery: opportunities and challenges. Mol Pharm 2012; 9(9):2380-2402.

219. Wonganan P, Lansakara P, Zhu S, Holzer M, Sandoval MA, Warthaka M et al. Just getting into cells is not enough: mechanisms underlying 4-(N)-stearoyl gemcitabine solid lipid nanoparticle's ability to overcome gemcitabine resistance caused by RRM1 overexpression. J Control Release 2013; 169(1-2):17-27.

220. Sun YL, Patel A, Kumar P, Chen ZS. Role of ABC transporters in cancer chemotherapy. Chin J Cancer 2012; 31(2):51-57.

221. Jabr-Milane LS, van Vlerken LE, Yadav S, Amiji MM. Multi-functional nanocarriers to overcome tumor drug resistance. Cancer Treat Rev 2008; 34(7):592-602.

222. Xue X, Liang XJ. Overcoming drug efflux-based multidrug resistance in cancer with nanotechnology. Chin J Cancer 2012; 31(2):100-109.

223. Zhang P, Ling G, Sun J, Zhang T, Yuan Y, Sun Y et al. Multifunctional nanoassemblies for vincristine sulfate delivery to overcome multidrug resistance by escaping P-glycoprotein mediated efflux. Biomaterials 2011; 32(23):5524-5533.

224. Zahedi P, De SR, Huynh L, Piquette-Miller M, Allen C. Combination drug delivery strategy for the treatment of multidrug resistant ovarian cancer. Mol Pharm 2011; 8(1):260-269.

225. Patil Y, Sadhukha T, Ma L, Panyam J. Nanoparticle-mediated simultaneous and targeted delivery of paclitaxel and tariquidar overcomes tumor drug resistance. J Control Release 2009; 136(1):21-29.

226. Navarro G, Sawant RR, Biswas S, Essex S, Tros d, I, Torchilin VP. P-glycoprotein silencing with siRNA delivered by DOPE-modified PEI overcomes doxorubicin resistance in breast cancer cells. Nanomedicine (Lond) 2012; 7(1):65-78.

227. Li YT, Chua MJ, Kunnath AP, Chowdhury EH. Reversing multidrug resistance in breast cancer cells by silencing ABC transporter genes with nanoparticle-facilitated delivery of target siRNAs. Int J Nanomedicine 2012; 7:2473-2481.

228. Wang Y, Guo M, Lu Y, Ding LY, Ron WT, Liu YQ et al. Alpha-tocopheryl polyethylene glycol succinate-emulsified poly(lactic-co-glycolic acid) nanoparticles for reversal of multidrug resistance in vitro. Nanotechnology 2012; 23(49):495103.

229. Wang J, Sun J, Chen Q, Gao Y, Li L, Li H et al. Star-shape copolymer of lysine-linked di-tocopherol polyethylene glycol 2000 succinate for doxorubicin delivery with reversal of multidrug resistance. Biomaterials 2012; 33(28):6877-6888.

230. Patil YB, Swaminathan SK, Sadhukha T, Ma L, Panyam J. The use of nanoparticle-mediated targeted gene silencing and drug delivery to overcome tumor drug resistance. Biomaterials 2010; 31(2):358-365.

231. Wu H, Shi Y, Huang C, Zhang Y, Wu J, Shen H et al. Multifunctional nanocarrier based on clay nanotubes for efficient intracellular siRNA delivery and gene silencing. J Biomater Appl 2013.

232. Ganesh S, Iyer AK, Weiler J, Morrissey DV, Amiji MM. Combination of siRNA-directed Gene Silencing With Cisplatin Reverses Drug Resistance in Human Non-small Cell Lung Cancer. Mol Ther Nucleic Acids 2013; 2:e110.

233. Yang F, Huang W, Li Y, Liu S, Jin M, Wang Y et al. Anti-tumor effects in mice induced by survivin-targeted siRNA delivered through polysaccharide nanoparticles. Biomaterials 2013; 34(22):5689-5699.

234. Markman JL, Rekechenetskiy A, Holler E, Ljubimova JY. Nanomedicine therapeutic approaches to overcome cancer drug resistance. Adv Drug Deliv Rev 2013.

235. Kunjachan S, Rychlik B, Storm G, Kiessling F, Lammers T. Multidrug resistance: Physiological principles and nanomedical solutions. Adv Drug Deliv Rev 2013.

236. Zhao P, Astruc D. Docetaxel nanotechnology in anticancer therapy. ChemMedChem 2012; 7(6):952-972.

237. Cortes JE, Pazdur R. Docetaxel. J Clin Oncol 1995; 13(10):2643-2655.

238. Herbst RS, Khuri FR. Mode of action of docetaxel - a basis for combination with novel anticancer agents. Cancer Treat Rev 2003; 29(5):407-415.

239. Engels FK, Mathot RA, Verweij J. Alternative drug formulations of docetaxel: a review. Anticancer Drugs 2007; 18(2):95-103.

240. Tan Q, Liu X, Fu X, Li Q, Dou J, Zhai G. Current development in nanoformulations of docetaxel. Expert Opin Drug Deliv 2012; 9(8):975-990.

241. Seo YG, Kim DW, Yeo WH, Ramasamy T, Oh YK, Park YJ et al. Docetaxel-loaded thermosensitive and bioadhesive nanomicelles as a rectal drug delivery system for enhanced chemotherapeutic effect. Pharm Res 2013; 30(7):1860-1870.

242. ten Tije AJ, Verweij J, Loos WJ, Sparreboom A. Pharmacological effects of formulation vehicles : implications for cancer chemotherapy. Clin Pharmacokinet 2003; 42(7):665-685.

243. Hennenfent KL, Govindan R. Novel formulations of taxanes: a review. Old wine in a new bottle? Ann Oncol 2006; 17(5):735-749.

244. Nie S, Xing Y, Kim GJ, Simons JW. Nanotechnology applications in cancer. Annu Rev Biomed Eng 2007; 9:257-288.

245. Koo H, Huh MS, Sun IC, Yuk SH, Choi K, Kim K et al. In vivo targeted delivery of nanoparticles for theranosis. Acc Chem Res 2011; 44(10):1018-1028.

246. Petros RA, DeSimone JM. Strategies in the design of nanoparticles for therapeutic applications. Nat Rev Drug Discov 2010; 9(8):615-627.

247. Jokerst JV, Lobovkina T, Zare RN, Gambhir SS. Nanoparticle PEGylation for imaging and therapy. Nanomedicine (Lond) 2011; 6(4):715-728.

248. Venkateswarlu V, Manjunath K. Preparation, characterization and in vitro release kinetics of clozapine solid lipid nanoparticles. J Control Release 2004; 95(3):627-638.

249. Yang SC, Lu LF, Cai Y, Zhu JB, Liang BW, Yang CZ. Body distribution in mice of intravenously injected camptothecin solid lipid nanoparticles and targeting effect on brain. J Control Release 1999; 59(3):299-307.

250. Schwarz C, Mehnert W, Lucks JS, M++ller RH. Solid lipid nanoparticles (SLN) for controlled drug delivery. I. Production, characterization and sterilization. Journal of Controlled Release 1994; 30(1):83-96.

251. Gao Y, Yang R, Zhang Z, Chen L, Sun Z, Li Y. Solid lipid nanoparticles reduce systemic toxicity of docetaxel: performance and mechanism in animal. Nanotoxicology 2011; 5(4):636-649.

252. Xu W, Lim SJ, Lee MK. Cellular uptake and antitumour activity of paclitaxel incorporated into trilaurin-based solid lipid nanoparticles in ovarian cancer. J Microencapsul 2013.

253. Lee MK, Lim SJ, Kim CK. Preparation, characterization and in vitro cytotoxicity of paclitaxel-loaded sterically stabilized solid lipid nanoparticles. Biomaterials 2007; 28(12):2137-2146.

254. Heurtault B, Saulnier P, Pech B, Proust JE, Benoit JP. A novel phase inversion-based process for the preparation of lipid nanocarriers. Pharm Res 2002; 19(6):875-880.

255. Peltier S, Oger JM, Lagarce F, Couet W, Benoit JP. Enhanced oral paclitaxel bioavailability after administration of paclitaxel-loaded lipid nanocapsules. Pharm Res 2006; 23(6):1243-1250.

256. Lacoeuille F, Hindre F, Moal F, Roux J, Passirani C, Couturier O et al. In vivo evaluation of lipid nanocapsules as a promising colloidal carrier for paclitaxel. Int J Pharm 2007; 344(1-2):143-149.

257. Li R, Eun JS, Lee MK. Pharmacokinetics and biodistribution of paclitaxel loaded in pegylated solid lipid nanoparticles after intravenous administration. Arch Pharm Res 2011; 34(2):331-337.

258. Videira MA, Arranja AG, Gouveia LF. Experimental design towards an optimal lipid nanosystem: a new opportunity for paclitaxel-based therapeutics. Eur J Pharm Sci 2013; 49(2):302-310.

259. Huynh L, Grant J, Leroux JC, Delmas P, Allen C. Predicting the solubility of the anti-cancer agent docetaxel in small molecule excipients using computational methods. Pharm Res 2008; 25(1):147-157.

260. Chan JM, Zhang L, Yuet KP, Liao G, Rhee JW, Langer R et al. PLGA-lecithin-PEG core-shell nanoparticles for controlled drug delivery. Biomaterials 2009; 30(8):1627-1634.

261. Tao W, Zeng X, Liu T, Wang Z, Xiong Q, Ouyang C et al. Docetaxel-loaded nanoparticles based on star-shaped mannitol-core PLGA-TPGS diblock copolymer for breast cancer therapy. Acta Biomater 2013.

262. Kim DW, Kim SY, Kim HK, Kim SW, Shin SW, Kim JS et al. Multicenter phase II trial of Genexol-PM, a novel Cremophor-free, polymeric micelle formulation of paclitaxel, with cisplatin in patients with advanced non-small-cell lung cancer. Ann Oncol 2007; 18(12):2009-2014.

263. Lee KS, Chung HC, Im SA, Park YH, Kim CS, Kim SB et al. Multicenter phase II trial of Genexol-PM, a Cremophor-free, polymeric micelle formulation of paclitaxel, in patients with metastatic breast cancer. Breast Cancer Res Treat 2008; 108(2):241-250.

264. Shi J, Xiao Z, Kamaly N, Farokhzad OC. Self-assembled targeted nanoparticles: evolution of technologies and bench to bedside translation. Acc Chem Res 2011; 44(10):1123-1134.

265. Mikhail AS, Allen C. Poly(ethylene glycol)-b-poly(epsilon-caprolactone) micelles containing chemically conjugated and physically entrapped docetaxel: synthesis, characterization, and the influence of the drug on micelle morphology. Biomacromolecules 2010; 11(5):1273-1280.

266. Farokhzad OC, Langer R. Impact of nanotechnology on drug delivery. ACS Nano 2009; 3(1):16-20.

267. Kraus LA, Samuel SK, Schmid SM, Dykes DJ, Waud WR, Bissery MC. The mechanism of action of docetaxel (Taxotere) in xenograft models is not limited to bcl-2 phosphorylation. Invest New Drugs 2003; 21(3):259-268.

268. Fang J, Sawa T, Maeda H. Factors and mechanism of "EPR" effect and the enhanced antitumor effects of macromolecular drugs including SMANCS. Adv Exp Med Biol 2003; 519:29-49.

269. Wang L, Li M, Zhang N. Folate-targeted docetaxel-lipid-based-nanosuspensions for active-targeted cancer therapy. Int J Nanomedicine 2012; 7:3281-3294.

270. Liu D, Liu F, Liu Z, Wang L, Zhang N. Tumor specific delivery and therapy by double-targeted nanostructured lipid carriers with anti-VEGFR-2 antibody. Mol Pharm 2011; 8(6):2291-2301.

271. Liu D, Liu Z, Wang L, Zhang C, Zhang N. Nanostructured lipid carriers as novel carrier for parenteral delivery of docetaxel. Colloids Surf B Biointerfaces 2011; 85(2):262-269.

272. Mi Y, Zhao J, Feng SS. Targeted co-delivery of docetaxel, cisplatin and herceptin by vitamin E TPGS-cisplatin prodrug nanoparticles for multimodality treatment of cancer. J Control Release 2013; 169(3):185-192.

273. Westesen K, Bunjes H. Do nanoparticles prepared from lipids solid at room temperature always possess a solid lipid matrix? International Journal of Pharmaceutics 1995; 115(1):129-131.

274. Yerlikaya F, Ozgen A, Vural I, Guven O, Karaagaoglu E, Khan MA et al. Development and Evaluation of Paclitaxel Nanoparticles Using a Quality-by-Design Approach. J Pharm Sci 2013.

275. Bunjes H, Westesen K, Koch MHJ. Crystallization tendency and polymorphic transitions in triglyceride nanoparticles. International Journal of Pharmaceutics 1996; 129:159-173.

276. Wasutrasawat P, Al-Obaidi H, Gaisford S, Lawrence MJ, Warisnoicharoen W. Drug solubilisation in lipid nanoparticles containing high melting point triglycerides. Eur J Pharm Biopharm 2013.

277. Li X, Wang D, Zhang J, Pan W. Preparation and pharmacokinetics of docetaxel based on nanostructured lipid carriers. J Pharm Pharmacol 2009; 61(11):1485-1492.

278. Wang S, Koo SI. Plasma clearance and hepatic utilization of stearic, myristic and linoleic acids introduced via chylomicrons in rats. Lipids 1993; 28(8):697-703.

279. Murphy RA, Mourtzakis M, Chu QS, Baracos VE, Reiman T, Mazurak VC. Supplementation with fish oil increases first-line chemotherapy efficacy in

patients with advanced nonsmall cell lung cancer. Cancer 2011; 117(16):3774-3780.

280. Arshad A, Chung WY, Steward W, Metcalfe MS, Dennison AR. Reduction in circulating pro-angiogenic and pro-inflammatory factors is related to improved outcomes in patients with advanced pancreatic cancer treated with gemcitabine and intravenous omega-3 fish oil. HPB (Oxford) 2013; 15(6):428-432.

281. Wynter MP, Russell ST, Tisdale MJ. Effect of n-3 fatty acids on the antitumour effects of cytotoxic drugs. In Vivo 2004; 18(5):543-547.

282. Kato T, Kolenic N, Pardini RS. Docosahexaenoic acid (DHA), a primary tumor suppressive omega-3 fatty acid, inhibits growth of colorectal cancer independent of p53 mutational status. Nutr Cancer 2007; 58(2):178-187.

283. Strouch MJ, Ding Y, Salabat MR, Melstrom LG, Adrian K, Quinn C et al. A high omega-3 fatty acid diet mitigates murine pancreatic precancer development. J Surg Res 2011; 165(1):75-81.

284. Merendino N, Loppi B, D'Aquino M, Molinari R, Pessina G, Romano C et al. Docosahexaenoic acid induces apoptosis in the human PaCa-44 pancreatic cancer cell line by active reduced glutathione extrusion and lipid peroxidation. Nutr Cancer 2005; 52(2):225-233.

285. Merendino N, Molinari R, Loppi B, Pessina G, D' AM, Tomassi G et al. Induction of apoptosis in human pancreatic cancer cells by docosahexaenoic acid. Ann N Y Acad Sci 2003; 1010:361-364.

286. D'Eliseo D, Manzi L, Merendino N, Velotti F. Docosahexaenoic acid inhibits invasion of human RT112 urinary bladder and PT45 pancreatic carcinoma cells via down-modulation of granzyme B expression. J Nutr Biochem 2012; 23(5):452-457.

287. Chen HW, Chao CY, Lin LL, Lu CY, Liu KL, Lii CK et al. Inhibition of matrix metalloproteinase-9 expression by docosahexaenoic acid mediated by heme oxygenase 1 in 12-O-tetradecanoylphorbol-13-acetate-induced MCF-7 human breast cancer cells. Arch Toxicol 2013; 87(5):857-869.

288. Rahman MM, Veigas JM, Williams PJ, Fernandes G. DHA is a more potent inhibitor of breast cancer metastasis to bone and related osteolysis than EPA. Breast Cancer Res Treat 2013; 141(3):341-352.

289. Spencer L, Mann C, Metcalfe M, Webb M, Pollard C, Spencer D et al. The effect of omega-3 FAs on tumour angiogenesis and their therapeutic potential. Eur J Cancer 2009; 45(12):2077-2086.

290. Wang Y, Li L, Jiang W, Yang Z, Zhang Z. Synthesis and preliminary antitumor activity evaluation of a DHA and doxorubicin conjugate. Bioorg Med Chem Lett 2006; 16(11):2974-2977.

291. Wang Y, Li L, Jiang W, Larrick JW. Synthesis and evaluation of a DHA and 10-hydroxycamptothecin conjugate. Bioorg Med Chem 2005; 13(19):5592-5599.

292. Bradley MO, Webb NL, Anthony FH, Devanesan P, Witman PA, Hemamalini S et al. Tumor targeting by covalent conjugation of a natural fatty acid to paclitaxel. Clin Cancer Res 2001; 7(10):3229-3238.

293. Bedikian AY, DeConti RC, Conry R, Agarwala S, Papadopoulos N, Kim KB et al. Phase 3 study of docosahexaenoic acid-paclitaxel versus dacarbazine in patients with metastatic malignant melanoma. Ann Oncol 2011; 22(4):787-793.

294. Homsi J, Bedikian AY, Papadopoulos NE, Kim KB, Hwu WJ, Mahoney SL et al. Phase 2 open-label study of weekly docosahexaenoic acid-paclitaxel in patients with metastatic uveal melanoma. Melanoma Res 2010; 20(6):507-510.

295. Sparreboom A, Wolff AC, Verweij J, Zabelina Y, van Zomeren DM, McIntire GL et al. Disposition of docosahexaenoic acid-paclitaxel, a novel taxane, in blood: in vitro and clinical pharmacokinetic studies. Clin Cancer Res 2003; 9(1):151-159.

296. Bradley MO, Swindell CS, Anthony FH, Witman PA, Devanesan P, Webb NL et al. Tumor targeting by conjugation of DHA to paclitaxel. J Control Release 2001; 74(1-3):233-236.

297. Hui YF, Reitz J. Gemcitabine: a cytidine analogue active against solid tumors. Am J Health Syst Pharm 1997; 54(2):162-170.

298. Pierantoni C, Pagliacci A, Scartozzi M, Berardi R, Bianconi M, Cascinu S. Pancreatic cancer: progress in cancer therapy. Crit Rev Oncol Hematol 2008; 67(1):27-38.

299. Kontopodis E, Kentepozidis N, Christophyllakis C, Boukovinas I, Kalykaki A, Kalbakis K et al. Docetaxel, gemcitabine and bevacizumab as salvage chemotherapy for HER-2-negative metastatic breast cancer. Cancer Chemother Pharmacol 2015; 75(1):153-160.

300. Nadal R, Bellmunt J. New treatments for bladder cancer: when will we make progress? Curr Treat Options Oncol 2014; 15(1):99-114.

301. Immordino ML, Brusa P, Rocco F, Arpicco S, Ceruti M, Cattel L. Preparation, characterization, cytotoxicity and pharmacokinetics of liposomes containing lipophilic gemcitabine prodrugs. J Control Release 2004; 100(3):331-346.

302. De Angel RE, Blando JM, Hogan MG, Sandoval MA, Lansakara P, Dunlap SM et al. Stearoyl gemcitabine nanoparticles overcome obesity-induced cancer cell resistance to gemcitabine in a mouse postmenopausal breast cancer model. Cancer Biol Ther 2013; 14(4):357-364.

303. ELi Lilly. GEMZAR (gemcitabine for injection), for intravenous use. 2014.

304. Moysan E, Bastiat G, Benoit JP. Gemcitabine versus Modified Gemcitabine: a review of several promising chemical modifications. Mol Pharm 2013; 10(2):430-444.

305. Abbruzzese JL, Grunewald R, Weeks EA, Gravel D, Adams T, Nowak B et al. A phase I clinical, plasma, and cellular pharmacology study of gemcitabine. J Clin Oncol 1991; 9(3):491-498.

306. Couvreur P, Stella B, Reddy LH, Hillaireau H, Dubernet C, Desmaele D et al. Squalenoyl nanomedicines as potential therapeutics. Nano Lett 2006; 6(11):2544-2548.

307. Tao XM, Wang JC, Wang JB, Feng Q, Gao SY, Zhang LR et al. Enhanced anticancer activity of gemcitabine coupling with conjugated linoleic acid against human breast cancer in vitro and in vivo. Eur J Pharm Biopharm 2012; 82(2):401-409.

308. Chitkara D, Mittal A, Behrman SW, Kumar N, Mahato RI. Self-assembling, amphiphilic polymer-gemcitabine conjugate shows enhanced antitumor efficacy against human pancreatic adenocarcinoma. Bioconjug Chem 2013; 24(7):1161-1173.

309. Maksimenko A, Alami M, Zouhiri F, Brion JD, Pruvost A, Mougin J et al. Therapeutic modalities of squalenoyl nanocomposites in colon cancer: an ongoing search for improved efficacy. ACS Nano 2014; 8(3):2018-2032.

310. Arias JL, Reddy LH, Othman M, Gillet B, Desmaele D, Zouhiri F et al. Squalene based nanocomposites: a new platform for the design of multifunctional pharmaceutical theragnostics. ACS Nano 2011; 5(2):1513-1521.

311. Reddy LH, Renoir JM, Marsaud V, Lepetre-Mouelhi S, Desmaele D, Couvreur P. Anticancer efficacy of squalenoyl gemcitabine nanomedicine on 60 human tumor cell panel and on experimental tumor. Mol Pharm 2009; 6(5):1526-1535.

312. Reddy LH, Ferreira H, Dubernet C, Mouelhi SL, Desmaele D, Rousseau B et al. Squalenoyl nanomedicine of gemcitabine is more potent after oral administration in leukemia-bearing rats: study of mechanisms. Anticancer Drugs 2008; 19(10):999-1006.

313. Reddy LH, Marque PE, Dubernet C, Mouelhi SL, Desmaele D, Couvreur P. Preclinical toxicology (subacute and acute) and efficacy of a new squalenoyl gemcitabine anticancer nanomedicine. J Pharmacol Exp Ther 2008; 325(2):484-490.

314. Reddy LH, Dubernet C, Mouelhi SL, Marque PE, Desmaele D, Couvreur P. A new nanomedicine of gemcitabine displays enhanced anticancer activity in sensitive and resistant leukemia types. J Control Release 2007; 124(1-2):20-27.

315. Rejiba S, Reddy LH, Bigand C, Parmentier C, Couvreur P, Hajri A. Squalenoyl gemcitabine nanomedicine overcomes the low efficacy of gemcitabine therapy in pancreatic cancer. Nanomedicine 2011; 7(6):841-849.

316. Wolfgang CL, Herman JM, Laheru DA, Klein AP, Erdek MA, Fishman EK et al. Recent progress in pancreatic cancer. CA Cancer J Clin 2013; 63(5):318-348.

317. Ryan DP, Hong TS, Bardeesy N. Pancreatic adenocarcinoma. N Engl J Med 2014; 371(11):1039-1049.

318. Muniz VP, Barnes JM, Paliwal S, Zhang X, Tang X, Chen S et al. The ARF tumor suppressor inhibits tumor cell colonization independent of p53 in a novel mouse model of pancreatic ductal adenocarcinoma metastasis. Mol Cancer Res 2011; 9(7):867-877.

319. Guo ZZ, Gallo JM. Selective Protection of 2',2'-Difluorodeoxycytidine (Gemcitabine). J Org Chem 1999; 64(22):8319-8322.

320. Beall HD, Getz JJ, Sloan KB. The estimation of relative water solubility for prodrugs that are unstable in water. International Journal of Pharmaceutics 1993; 93:37-47.

321. Hsu CH, Jay M, Bummer PM, Lehmler HJ. Chemical stability of esters of nicotinic acid intended for pulmonary administration by liquid ventilation. Pharm Res 2003; 20(6):918-925.

322. Naguib YW, Rodriguez BL, Li X, Hursting SD, Williams RO, III, Cui Z. Solid lipid nanoparticle formulations of docetaxel prepared with high melting point triglycerides: in vitro and in vivo evaluation. Mol Pharm 2014; 11(4):1239-1249.

323. Lanz C, Fruh M, Thormann W, Cerny T, Lauterburg BH. Rapid determination of gemcitabine in plasma and serum using reversed-phase HPLC. J Sep Sci 2007; 30(12):1811-1820.

324. Lashinger LM, Harrison LM, Rasmussen AJ, Logsdon CD, Fischer SM, McArthur MJ et al. Dietary energy balance modulation of Kras- and Ink4a/Arf+/--driven pancreatic cancer: the role of insulin-like growth factor-I. Cancer Prev Res (Phila) 2013; 6(10):1046-1055.

325. Raut CP, Nawrocki S, Lashinger LM, Davis DW, Khanbolooki S, Xiong H et al. Celecoxib inhibits angiogenesis by inducing endothelial cell apoptosis in human pancreatic tumor xenografts. Cancer Biol Ther 2004; 3(12):1217-1224.

326. Bruns CJ, Harbison MT, Kuniyasu H, Eue I, Fidler IJ. In vivo selection and characterization of metastatic variants from human pancreatic adenocarcinoma by using orthotopic implantation in nude mice. Neoplasia 1999; 1(1):50-62.

327. Owen SC. In: Rowe RC, Sheskey PJ, Owen SC Eds, Handbook of Pharmaceutical Excipients. London, Pharmaceutical Press, 2006; 32-35.

328. Vandana M, Sahoo SK. Long circulation and cytotoxicity of PEGylated gemcitabine and its potential for the treatment of pancreatic cancer. Biomaterials 2010; 31(35):9340-9356.

329. Pasut G, Canal F, Dalla VL, Arpicco S, Veronese FM, Schiavon O. Antitumoral activity of PEG-gemcitabine prodrugs targeted by folic acid. J Control Release 2008; 127(3):239-248.

330. Guo P, Ma J, Li S, Guo Z, Adams AL, Gallo JM. Targeted delivery of a peripheral benzodiazepine receptor ligand-gemcitabine conjugate to brain tumors in a xenograft model. Cancer Chemother Pharmacol 2001; 48(2):169-176.

331. Maiti S, Park N, Han JH, Jeon HM, Lee JH, Bhuniya S et al. Gemcitabine-coumarin-biotin conjugates: a target specific theranostic anticancer prodrug. J Am Chem Soc 2013; 135(11):4567-4572.

332. Ali SM, Khan AR, Ahmad MU, Chen P, Sheikh S, Ahmad I. Synthesis and biological evaluation of gemcitabine-lipid conjugate (NEO6002). Bioorg Med Chem Lett 2005; 15(10):2571-2574.

333. Alexander RL, Greene BT, Torti SV, Kucera GL. A novel phospholipid gemcitabine conjugate is able to bypass three drug-resistance mechanisms. Cancer Chemother Pharmacol 2005; 56(1):15-21.

334. Khare V, Kour S, Alam N, Dubey RD, Saneja A, Koul M et al. Synthesis, characterization and mechanistic-insight into the anti-proliferative potential of PLGA-gemcitabine conjugate. Int J Pharm 2014; 470(1-2):51-62.

335. Bergman AM, Pinedo HM, Peters GJ. Determinants of resistance to 2',2'-difluorodeoxycytidine (gemcitabine). Drug Resist Updat 2002; 5(1):19-33.

336. de Sousa CL, Monteiro G. Gemcitabine: metabolism and molecular mechanisms of action, sensitivity and chemoresistance in pancreatic cancer. Eur J Pharmacol 2014; 741:8-16.

337. Andersson R, Aho U, Nilsson BI, Peters GJ, Pastor-Anglada M, Rasch W et al. Gemcitabine chemoresistance in pancreatic cancer: molecular mechanisms and potential solutions. Scand J Gastroenterol 2009; 44(7):782-786.

338. Wang Y, Fan W, Dai X, Katragadda U, Mckinley D, Teng Q et al. Enhanced tumor delivery of gemcitabine via PEG-DSPE/TPGS mixed micelles. Mol Pharm 2014; 11(4):1140-1150.

339. Zhang G, Panigrahy D, Mahakian LM, Yang J, Liu JY, Stephen Lee KS et al. Epoxy metabolites of docosahexaenoic acid (DHA) inhibit angiogenesis, tumor growth, and metastasis. Proc Natl Acad Sci U S A 2013; 110(16):6530-6535.

340. Fukui M, Kang KS, Okada K, Zhu BT. EPA, an omega-3 fatty acid, induces apoptosis in human pancreatic cancer cells: role of ROS accumulation, caspase-8 activation, and autophagy induction. J Cell Biochem 2013; 114(1):192-203.

341. Li S, Qin J, Tian C, Cao J, Fida G, Wang Z et al. The targeting mechanism of DHA ligand and its conjugate with Gemcitabine for the enhanced tumor therapy. Oncotarget 2014; 5(11):3622-3635.

342. Chu E. Clinical Colorectal Cancer: Ode to 5-Fluorouracil. Clinical Colorectal Cancer 2007; 6(9):609.

343. Longley DB, Harkin DP, Johnston PG. 5-fluorouracil: mechanisms of action and clinical strategies. Nat Rev Cancer 2003; 3(5):330-338.

344. Moore AY. Clinical applications for topical 5-fluorouracil in the treatment of dermatological disorders. J Dermatolog Treat 2009; 20(6):328-335.

345. Ceilley RI. Mechanisms of action of topical 5-fluorouracil: review and implications for the treatment of dermatological disorders. J Dermatolog Treat 2012; 23(2):83-89.

346. de Vries AC, Bogaards NA, Hooft L, Velema M, Pasch M, Lebwohl M et al. Interventions for nail psoriasis. Cochrane Database Syst Rev 2013; 1:CD007633.

347. Takahashi H, Funabiki K, Hasebe S, Fukuda-Yamamoto T, Kaieda S, Iwanaga T et al. Clinical efficacy of 5-fluorouracil (5-FU) topical cream for treatment of cholesteatoma. Auris Nasus Larynx 2005; 32(4):353-357.

348. Litwin MS, Krementz ET, Mansell PW, Reed RJ. Topical chemotherapy of lentigo maligna with 5-fluorouracil. Cancer 1975; 35(3):721-733.

349. de Keizer RJ, de Wolff-Rouendaal D, van Delft JL. Topical application of 5-fluorouracil in premalignant lesions of cornea, conjunctiva and eyelid. Doc Ophthalmol 1986; 64(1):31-42.

350. Gross K, Kircik L, Kricorian G. 5% 5-Fluorouracil cream for the treatment of small superficial Basal cell carcinoma: efficacy, tolerability, cosmetic outcome, and patient satisfaction. Dermatol Surg 2007; 33(4):433-439.

351. Gupta RR, Jain SK, Varshney M. AOT water-in-oil microemulsions as a penetration enhancer in transdermal drug delivery of 5-fluorouracil. Colloids Surf B Biointerfaces 2005; 41(1):25-32.

352. Paolino D, Cosco D, Muzzalupo R, Trapasso E, Picci N, Fresta M. Innovative bola-surfactant niosomes as topical delivery systems of 5-fluorouracil for the treatment of skin cancer. Int J Pharm 2008; 353(1-2):233-242.

353. Singh BN, Singh RB, Singh J. Effects of ionization and penetration enhancers on the transdermal delivery of 5-fluorouracil through excised human stratum corneum. Int J Pharm 2005; 298(1):98-107.

354. Sabitha M, Sanoj RN, Nair A, Lakshmanan VK, Nair SV, Jayakumar R. Development and evaluation of 5-fluorouracil loaded chitin nanogels for treatment of skin cancer. Carbohydr Polym 2013; 91(1):48-57.

355. Mohs FE, Jones DL, Bloom RF. Tendency of fluorouracil to conceal deep foci of invasive basal cell carcinoma. Arch Dermatol 1978; 114(7):1021-1022.

356. Fang JY, Hung CF, Fang YP, Chan TF. Transdermal iontophoresis of 5-fluorouracil combined with electroporation and laser treatment. Int J Pharm 2004; 270(1-2):241-249.

357. Meidan VM, Walmsley AD, Docker MF, Irwin WJ. Ultrasound-enhanced diffusion into coupling gel during phonophoresis of 5-fluorouracil. Int J Pharm 1999; 185(2):205-213.

358. Park JH, Choi SO, Seo S, Choy YB, Prausnitz MR. A microneedle roller for transdermal drug delivery. Eur J Pharm Biopharm 2010; 76(2):282-289.

359. Prausnitz MR. Microneedles for transdermal drug delivery. Adv Drug Deliv Rev 2004; 56(5):581-587.

360. Kumar A, Wonganan P, Sandoval MA, Li X, Zhu S, Cui Z. Microneedle-mediated transcutaneous immunization with plasmid DNA coated on cationic PLGA nanoparticles. J Control Release 2012; 163(2):230-239.

361. Kumar A, Li X, Sandoval MA, Rodriguez BL, Sloat BR, Cui Z. Permeation of antigen protein-conjugated nanoparticles and live bacteria through microneedle-treated mouse skin. Int J Nanomedicine 2011; 6:1253-1264.

362. Kim YC, Park JH, Prausnitz MR. Microneedles for drug and vaccine delivery. Adv Drug Deliv Rev 2012; 64(14):1547-1568.

363. Liu W, Li X, Wong YS, Zheng W, Zhang Y, Cao W et al. Selenium nanoparticles as a carrier of 5-fluorouracil to achieve anticancer synergism. ACS Nano 2012; 6(8):6578-6591.

364. Qu X, Felder MA, Perez HZ, Sondel PM, Rakhmilevich AL. Antitumor effects of anti-CD40/CpG immunotherapy combined with gemcitabine or 5-fluorouracil chemotherapy in the B16 melanoma model. Int Immunopharmacol 2013; 17(4):1141-1147.

365. Bath-Hextall FJ, Perkins W, Bong J, Williams HC. Interventions for basal cell carcinoma of the skin. Cochrane Database Syst Rev 2007;(1):CD003412.

366. Bariya SH, Gohel MC, Mehta TA, Sharma OP. Microneedles: an emerging transdermal drug delivery system. J Pharm Pharmacol 2012; 64(1):11-29.

Vita

Youssef Wahib Naguib Ibrahim was born and raised in Minia, Egypt in 1981. He received bachelor's degree of Pharmacy in 2003 and master's degree in pharmaceutics in 2009, both from Minia University. He joined the graduate school at the University of Texas at Austin in fall 2011. During this time, he worked as a graduate research assistant, as well as a teaching assistant at the college of Pharmacy at the University of Texas at Austin. Youssef Wahib Naguib Ibrahim is a registered pharmacist in Egypt.

E-mail address: naguib@utexas.edu

This dissertation was typed by Youssef Wahib Naguib Ibrahim